

The VLTI/MIDI[★] view on the inner mass loss of evolved stars from the Herschel MESS sample

C. Paladini^{1,2}, D. Klotz², S. Sacuto^{2,3}, E. Lagadec⁴, M. Wittkowski⁵, A. Richichi⁶, J. Hron², A. Jorissen¹, M. A. T. Groenewegen⁷, F. Kerschbaum², T. Verhoelst⁸, G. Rau², H. Olofsson⁹, R. Zhao-Geisler¹⁰, and A. Matter⁴

¹ Institut d'Astronomie et d'Astrophysique, Université libre de Bruxelles, CP 226, Boulevard du Triomphe, 1050 Brussels, Belgium; e-mail: claudia.paladini@ulb.ac.be

² University of Vienna, Department of Astrophysics, Türkenschanzstrasse 17, 1180 Wien, Austria

³ University of Uppsala, Department of Physics and Astronomy, Division of Astronomy and Space Physics, Box 516, 75120, Uppsala, Sweden

⁴ Laboratoire Lagrange, Université Côte d'Azur, Observatoire de la Côte d'Azur, CNRS, Blvd de l'Observatoire, CS 34229, 06304 Nice cedex 4, France

⁵ ESO, Karl-Schwarzschild-Str. 2, 85748 Garching bei München, Germany

⁶ National Astronomical Research Institute of Thailand, 191 Siriphanich Bldg., Huay Kaew Rd., Suthep, Muang, 50200 Chiang Mai, Thailand

⁷ Koninklijke Sterrenwacht van België, Ringlaan 3, 1180 Brussel, Belgium

⁸ Belgian Institute for Space Aeronomy (BIRA-IASB), Ringlaan-3-Avenue Circulaire, B-1180 Brussels, Belgium

⁹ Onsala Space Observatory, Dept. of Earth and Space Sciences, Chalmers University of Technology, 43992 Onsala, Sweden

¹⁰ National Taiwan Normal University, Department of Earth Sciences, 88 Sec. 4, Ting-Chou Rd, Wenshan District, Taipei, 11677, Taiwan, ROC

Received; accepted

ABSTRACT

Context. The mass-loss process from evolved stars is a key ingredient for our understanding of many fields of astrophysics, including stellar evolution and the chemical enrichment of the interstellar medium (ISM) via stellar yields. Nevertheless, many questions are still unsolved, one of which is the geometry of the mass-loss process.

Aims. Taking advantage of the results from the Herschel Mass loss of Evolved StarS (MESS) programme, we initiated a coordinated effort to characterise the geometry of mass loss from evolved red giants at various spatial scales.

Methods. For this purpose we used the MID-infrared interferometric Instrument (MIDI) to resolve the inner envelope of 14 asymptotic giant branch stars (AGBs) in the MESS sample. In this contribution we present an overview of the interferometric data collected within the frame of our Large Programme, and we also add archive data for completeness. We studied the geometry of the inner atmosphere by comparing the observations with predictions from different geometric models.

Results. Asymmetries are detected for the following five stars: R Leo, RT Vir, π^1 Gruis, \omicron Ori, and R Crb. All the objects are O-rich or S-type, suggesting that asymmetries in the N band are more common among stars with such chemistry. We speculate that this fact is related to the characteristics of the dust grains. Except for one star, no interferometric variability is detected, i.e. the changes in size of the shells of non-mira stars correspond to changes of the visibility of less than 10%. The observed spectral variability confirms previous findings from the literature. The detection of dust in our sample follows the location of the AGBs in the IRAS colour-colour diagram: more dust is detected around oxygen-rich stars in region II and in the carbon stars in region VII. The SiC dust feature does not appear in the visibility spectrum of the U Ant and S Sct, which are two carbon stars with detached shells. This finding has implications for the theory of SiC dust formation.

Key words. Stars: late-type – Stars: AGB and post-AGB – Stars: mass loss – Circumstellar matter – Technique: high angular resolution – Technique: interferometric

1. Introduction

Most of the material processed during the lifetime of low- to intermediate-mass stars is returned to the interstellar medium (ISM) during the asymptotic giant branch (AGB) stage. This material is crucial for the chemical evolution of galaxies (perhaps

even at high redshift; Valiante et al. 2009), and it contributes to building new generations of stars and planets.

The general picture that explains the mass-loss process assumes that stellar pulsation triggers shock waves in the atmosphere. These shocks lift the gas above the stellar surface, creating dense cool layers where dust may form. Depending on the chemistry of the star, theory predicts that the radiation pressure on dust or the scattering on micron-size dust grains drive the stellar material away (Höfner & Dorfi 1997; Woitke 2006; Höfner 2008). An important aspect of the mass-loss process that is poorly understood is its geometry, i.e. the deviation of the

[★] Based on observations collected at the European Organisation for Astronomical Research in the Southern Hemisphere under ESO programmes 073.D-0711, 076.D-0620, 077.D-0294, 078.D-0122, 080.D-0801, 081.D-0021, 083.D-0234, 086.D-0737, 086.D-899, 187.D-0924, 089.D-0562, 090.D-410, 091.C-0468, 091.D-0344

density distribution from spherical symmetry on different spatial scales. The assumption about the geometry of the circumstellar environment affects calculations of mass-loss rates and other fundamental parameters (Ohnaka et al. 2008b). In recent years, several observing campaigns were carried out with the purpose of investigating the geometry of the envelope of AGB stars (references below). Observations suggest that the wind mechanism may depend on the initial mass of the objects and on the evolution along the AGB (Habing & Olofsson 2003). Despite first evidence in favour of overall spherical symmetry, some observations (Knapp et al. 1997, e.g. V Hya) show very complicated geometry at various spatial scales, and no consensus on its origin has been reached so far (Habing & Olofsson 2003). Understanding how the mass-loss shapes the envelope of AGB stars is crucial also for the progeny. Although a binary companion is currently the most accepted explanation, other mechanisms such as rotation velocity and magnetic fields might still play a role (De Marco 2009). Investigating the morphology of the atmosphere of AGB stars at different spatial scales and evolutionary stages (early-AGB and thermal-pulse AGB) helps to clarify the picture in the follow-up stages.

By scanning the envelope of an AGB star from the inside to the outside one can distinguish the following:

Inner circumstellar envelope (CSE). At milliarcsecond scales (1-2.5 stellar radii), close to the photosphere of the stars, asymmetries are frequently detected with lunar occultations (Richichi et al. 1995; Meyer et al. 1995) and optical interferometry (Ragland et al. 2006; Le Bouquin et al. 2009; Pluzhnik et al. 2009; Chiavassa et al. 2010; Wittkowski et al. 2011; Cruzalèbes et al. 2013a; van Belle et al. 2013; Mayer et al. 2014; van Belle et al. 2013; Cruzalèbes et al. 2015). The asymmetric structures are often ascribed to convective patterns, but other interpretations are also invoked (mainly the effect of stellar rotation and binarity). It is observed that asymmetries in the brightness distribution are more frequent for Miras (Cruzalèbes et al. 2015, i.e. towards the end of the AGB life) and irregular variables (Ragland et al. 2006); asymmetries are more frequent in C-rich stars than in the O-rich stars.

Intermediate CSE. Between 2 and 10 stellar radii, asymmetries, and clumpiness are also observed for several objects (Weigelt et al. 1998; Tuthill et al. 2000; Weigelt et al. 2002; Leão et al. 2006; Tatebe et al. 2006; Chandler et al. 2007; Paladini et al. 2012; Sacuto et al. 2013). In a very few cases the asymmetries have a clear pattern resembling a spiral or a disc. These cases are usually related to the presence of a hidden binary companion (Mauron & Huggins 2006; Deroo et al. 2007; Ohnaka et al. 2008a; Maercker et al. 2012; Mayer et al. 2013; Decin et al. 2014; Kervella et al. 2014; Ramstedt et al. 2014; Lykou et al. 2015; Kervella et al. 2015). On the other hand, many other authors detect time variability but no clear signatures of asymmetries (Danchi et al. 1994; Ohnaka et al. 2005; Wittkowski et al. 2007; Karovicova et al. 2011; Sacuto et al. 2011; Zhao-Geisler et al. 2011, 2012; Karovicova et al. 2013). To confuse the picture even more, SiO maser observations show evidence for clumpy isotropic mass loss in the atmosphere of O-rich AGB stars, while H₂O and OH masers (at $R > 10 R_*$) probing the intermediate-outer part of AGB stars are less conclusive regarding the geometry.

Outer CSE. Submillimeter observations of CO line profiles obtained towards M stars may deviate significantly from those expected from a spherical envelope (Knapp et al. 1998; Winters et al. 2003; Klotz et al. 2012a). Imaging in the CO radio emission lines of carbon stars revealed spherically symmetric thin detached shells (Olofsson et al. 2000), probably originating dur-

ing the thermal pulses known to occur during the AGB phase. Images provided by the Herschel/PACS instrument within the frame of the Herschel Mass loss of Evolved StarS guaranteed time key programme (MESS; Groenewegen et al. 2011) showed that the morphology of the outer atmosphere ($R > 1000 R_*$) of AGBs differs depending on various factors (for example interaction between wind and the interstellar medium, or wind-wind interaction; Cox et al. 2012).

Altogether it is clear that one has to probe all spatial scales to understand the physics of these complex outflows. While previous studies with the aim of detecting asymmetries suffered from a lack of (u, v) coverage (cfr. optical/infrared interferometry) and/or instruments with sufficient sensitivities, the advent of new facilities with improved resolution and sensitivity like Herschel, ALMA, and VLTI offers the unique chance to understand the mass-loss and dust-formation processes, and generally speaking, the life cycle of dust and gas in the Universe.

In September 2010, we proposed a Large Programme (LP) to the European Southern Observatory (ESO) to complement the Herschel observations with observations using the mid-infrared instruments MIDI on the Very Large Telescope Interferometer (VLTI) and VISIR on the Very Large Telescope (VLT). The aims of the study are i) to establish whether asymmetries of the outer CSE originate in the dust-forming region or whether they are only due to interaction with the ISM; ii) to evaluate at which height, the mass-loss process becomes manifestly non-spherical; and iii) to understand how the geometry of the atmosphere changes at the different evolutionary stages (M-S-C stars, and from almost dust-free to very dusty objects) within the AGB sequence.

In this paper, we present the programme and data of the interferometric (MIDI) campaign interpreted with geometric models. All the ESO archive data available for the targets are incorporated in the analysis to give a complete overview. This first work will be followed by a series of papers including a detailed interpretation of the MIDI data in terms of model atmospheres. The VISIR observing campaign was severely affected by bad weather conditions; a new observing proposal was recently accepted.

The selection of the targets is described in Sect. 2.1, while the strategy for observations is given in Sect. 2.2. The data reduction is reported in Sect. 2.3. We also used archive data that are introduced in Sect. 2.4. The programme used for the interpretation of the interferometric data is described in Sect. 3. Results are presented in Sect. 4. The discussion, conclusions, and outlooks are given in Sects. 5 and 6, respectively. The detailed description of every single target can be found in Appendix A, and the journal of the observations is provided in Appendix B.

2. Target selection and data

2.1. Target selection

A sub-sample of the AGB stars observed within the Herschel key programme MESS (Groenewegen et al. 2011; Cox et al. 2012) was selected on the basis of the following criteria: declination accessible from the southern hemisphere where the ESO telescopes are located, brightness within the limits of the instruments, and a range of chemistries and variability types. The IRAS two-colour diagram (van der Veen & Habing 1988) was used as a reference with the purpose of sampling AGBs with different shell properties (Fig. 1). Every region includes targets with well-defined infrared characteristics: variability, and IRAS Low Resolution Spectrometer (LRS) classification.

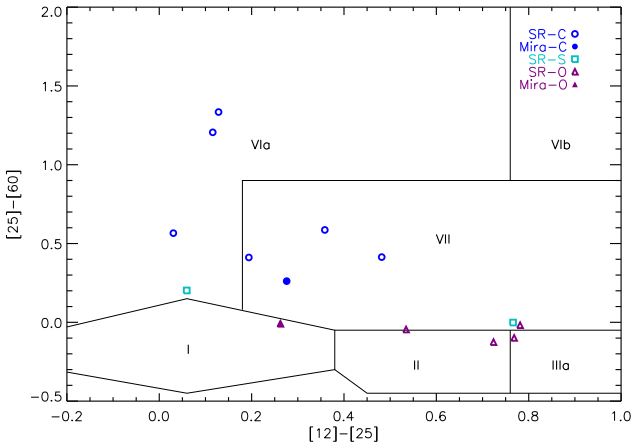


Fig. 1. Targets of our sample shown in the IRAS two-colour diagram of van der Veen & Habing (1988).

The mildly variable O-rich AGB stars without extended circumstellar shells are expected to populate region I. In region II the objects are surrounded by young O-rich shells, while in region IIIa the shells are more evolved and mass-loss rates are higher. Most of the C-rich objects with relatively cold dust are located in region VIa (so-called detached-shell objects), while the objects located in region VIb have hot oxygen-rich dust close to the star and cold dust at larger distances. The variable stars with evolved C-rich shells and infrared carbon stars are in region VII. The panels not covered within the observing sample are populated by objects with optically thick envelopes having no visual counterparts, and by planetary nebulae. The list of targets is presented in Table 1 together with the location in the IRAS colour-colour diagram, the morphological class identified by Cox et al. (2012) from the Herschel/PACS images, and general characteristics such as spectral type, variability class, IRAS 12 μ m flux, period, distance, and mass-loss rate.

2.2. Observing strategy

In this work we concentrate on possible asymmetries developing in the dust-forming region. Danchi et al. (1994) and more recently Norris et al. (2012) observed that dust is forming between 3 and 5 stellar radii, and even closer to the star in the case of Mira variables, as Draine (1981) already predicted. As a consequence, one needs to have an angular resolution of ~ 20 mas to observe the *locus* of dust formation for AGBs within 1 kpc. For this reason, the MIDI instrument (Leinert et al. 2003) installed at the ESO Very Large Telescope Interferometer (VLTI) on Cerro Paranal (Chile) until March 2015 was chosen. The MIDI instrument is a two-beam combiner interferometer observing in the *N* band (8–13 μ m). For every observation, the instrument delivers one visibility spectrum (sometime shortened to visibility in the text), one total flux spectrum, and one differential phase spectrum (phase difference between different spectral channels; Sect. 4.2). Depending on the correlated magnitude of the target, either the HIGH-SENS (where the correlated and total flux are measured one after the other) or SCI-PHOT (where the correlated and total flux are measured simultaneously) mode was chosen. All the LP data have spectral resolution $R = \lambda/\Delta\lambda \sim 30$.

To optimise the observations for studying the geometry the following strategy was used. The choice for the baseline configurations was split in two different categories, based on the Herschel data available: configurations for non-spherical (such as the bow shock in the case of TX Psc; Jorissen et al. 2011), and for

spherical objects (such as the detached-shell object U Ant; Kerschbaum et al. 2010). For the non-spherical cases we selected one baseline oriented in the direction of the asymmetry and one baseline perpendicular to the latter. A third baseline, with orientation in between the two, was selected to put constraints on the possible elongation. Baselines with random orientation were selected for the symmetric stars, as well as in the cases where PACS images were not yet available. Thus, we are able to constrain any possible deviation from sphericity. We also tried to sample the same spatial frequencies by choosing the same baseline lengths for all points. The baseline length also has to be selected carefully for resolving the dust formation zone. Given the fact that not all the targets of the sample had a measured photospheric diameter, the latter was estimated through the $(V-K)$ relation of van Belle et al. (1999). Following the results of Danchi et al. (1994), we thus assumed that the diameter in the *N* band is approximately three times the photospheric diameter, and the baseline was selected accordingly.

For planning the observations, we used ASPRO and ASPRO2 developed by the Jean-Marie Mariotti Center Aspro service¹. The observations were carried out between 2011 April 23 and 2012 July 01 on the 1.8 m Auxiliary Telescopes (ATs). We used the recommended observation sequence CAL-SCI-CAL. The following selection criteria for calibrator stars were applied: brightness (difference between calibrator and science target of ± 1 mag), position (RA and Dec as close as possible to the science target), size (the calibrator should be as small as possible), and spectral type (if possible the calibrator should have a spectral type earlier than M0). The list of calibrators and their main characteristics are presented in Table 2. The journal of the MIDI observations is available as online material (Appendix B).

2.3. Observations and data reduction

The MIDI data were reduced using the data reduction pipeline MIA+EWS² (Jaffe 2004a; Ratzka 2005; Leinert et al. 2004). A detailed description of the data quality tests that were applied during the data reduction can be found in Klotz et al. (2012b). Data were reduced with all calibrators observed in the same night (if possible within ± 2 hours) and with the same baseline configuration as the science target. The final calibrated visibilities are then the mean of all the visibilities, differential phases, and fluxes reduced with suitable calibrators. The error is derived from the standard deviation of that series. If the former error is lower than $\pm 10\%$ or only one calibrator was available during the night, a multiplicative error of $\pm 10\%$ was used (Chesneau 2007).

The extraction of the differential phase was carried out following the standard procedure of EWS (Jaffe 2004b). The differential phase was corrected for the changing index of refraction of air by subtracting a linear slope, so that the mean phase over the *N* band is zero. We did not correct for higher order effects owing to water vapour content (PWV). Instead, we employed a very simplistic approach, by calibrating the differential phases using several calibrators taken over the night and deriving our error estimate on the phase from the scatter of these multiple calibrations. The instrumental phase measured for the calibrators during the different nights is usually stable and of the order of $\pm 5^\circ$. Any uncertainty on the differential phase caused by the

¹ Available at <http://www.jmmc.fr/aspro>

² <http://www.strw.leidenuniv.nl/~jaffe/ews/MIA+EWS-Manual/index.html>

Table 1. Target list.

Target	IRAS colour-colour region	Herschel/PACS ^(a) morphology	Spectral Type	Variability	F_{12} [Jy]	Period [d]	Distance ^(b) [pc]	Mass-loss rate [$M_{\odot}\text{yr}^{-1}$]
θ Aps	II (O-rich shells)	Fermata	M6.5III	SRb	734.30	119 ^(c)	113 ⁺⁷ ₋₆	0.4×10^{-7} ^(d)
R Crt	II (O-rich shells)	Eye	M7III	SRb	637.90	160 ^(c)	261 ⁺⁸⁶ ₋₅₂	8×10^{-7} ^(d)
R Leo	I	Fermata	M8IIIe	M	2161.00	310 ^(e)	110 ⁺¹⁷ ₋₁₁	9.4×10^{-8} ^(f)
T Mic	II (O-rich shells)	Fermata	M7III	SRb	493.80	347 ^(c)	200 ⁺³⁷ ₋₃₇	8×10^{-8} ^(d)
RT Vir	IIIa	Fermata	M8III	SR	462.20	375 ^(g)	136 ⁺¹⁷ ₋₁₄	5×10^{-7} ^(d)
π^1 Gru	II/IIIa/VII	Irregular	S5+G0V	SRb	908.50	198 ^(h)	153 ⁺²³ ₋₁₈	4.6×10^{-7} ⁽ⁱ⁾
omi Ori	VIa/I	Irregular	S+WD	SR	85.35	...	200 ⁺³³ ₋₂₅	$< 0.4 \times 10^{-7}$ ^(j)
U Ant	VIa	Ring	N:var	Lb	167.50	...	270 ⁺⁴³ ₋₃₄	2×10^{-8} ^(k)
R Lep	VII	Point Source	CIIe	M	379.50	427 ^(c)	470 ⁺³⁰¹ ₋₁₂₂	1.6×10^{-6} ^(k)
Y Pav	VII	Point Source	CII	SRb	72.38	233 ^(c)	400 ⁺¹²⁶ ₋₇₇	4×10^{-7} ^(l)
TX Psc	VIa	Fermata	CII	Lb	162.90	...	275 ⁺³³ ₋₂₇	3.2×10^{-7} ^(k)
S Sct	VIa	Ring	CII	SR	65.31	148 ^(c)	386 ⁺¹⁰⁹ ₋₇₀	5.6×10^{-6} ^(k)
AQ Sgr	VII	Fermata	CII	SR	56.64	199 ^(c)	333 ⁺⁹⁶ ₋₆₁	7.7×10^{-7} ^(k)
X TrA	VII	Ring	C	Lb	201.00	...	360 ⁺⁶⁸ ₋₄₉	1.8×10^{-7} ^(k)

References. (a) Cox et al. (2012); (b) van Leeuwen (2007); (c) Samus et al. (2009); (d) Olofsson et al. (2002a); (e) Whitelock & Feast (2000); (f) Knapp et al. (1998); (g) Imai et al. (1997); (h) Tabur et al. (2009); (i) Jorissen & Knapp (1998); (j) Groenewegen & de Jong (1998); (k) Bergeat & Chevallier (2005); (l) Winters et al. (2003).

Table 2. Calibrator list.

HD	Spectral type ^a	F_{12} ^(a) [Jy]	θ ^(b) [mas]	used for
18884	M1.5IIIa	234.7	12.28 ± 0.05	omi Ori, R Lep
20720	M3/M4III	162.70	10.14 ± 0.04	R Lep
25025	M1IIIb	109.6	8.74 ± 0.09	R Leo
29139	K5III	699.7	20.398 ± 0.087	R Leo, U Ant
32887	K4III	56.82	5.90 ± 0.06	R Lep
39425	K1IIICN+1	28.0	3.752 ± 0.017	omi Ori
48915	A1V	143.1	6.08 ± 0.03	R Leo, R Lep, U Ant
50778	K4III	24.6	3.904 ± 0.015	omi Ori
61421	F5IV-V	79.1	5.25 ± 0.21	R Leo
81797	K3II-III	157.6	9.142 ± 0.045	θ Aps, R Crt, RT Vir, R Leo
112142	M3III	47.0	5.90 ± 0.7	R Crt, RT Vir, AQ Sgr
120323	M4.5III	255.4	13.25 ± 0.06	R Crt, RT Vir, R Leo, U Ant, AQ Sgr
123139	K0III	56.9	5.33 ± 0.057	R Crt, RT Vir, R Leo, AQ Sgr
129456	K5III	21.4	3.37 ± 0.014	T Mic
133216	M3/M4III	200.7	11.154 ± 0.046	RT Vir
150798	K2II-III	144.0	8.76 ± 0.12	θ Aps, R Crt R Leo, Y Pav, X TrA
151249	K5III	52.18	5.515 ± 0.179	Y Pav
152786	K3III	82.1	8.02 ± 3.23	θ Aps, R Crt R Leo, AQ Sgr
165135	K1III	23.4	3.47 ± 0.015	T Mic
167618	M3.5III	213.7	11.665 ± 0.043	θ Aps, T Mic
168454	K3III	62.17	5.874 ± 0.026	S Sct, AQ Sgr
169916	K0IV	31.2	3.995 ± 0.019	T Mic, Y Pav, S Sct, AQ Sgr
177716	K1III	26.0	3.78 ± 0.21	T Mic
206778	K2Ib	103.9	7.59 ± 0.046	θ Aps, R Leo, π^1 Gru
211416	K3III	59.3	5.92 ± 0.28	AQ Sgr
224935	M3III	86.90	7.25 ± 0.03	π^1 Gru

Notes. ^(a) <http://simbad.u-strasbg.fr/simbad/>;

^(b) http://www.eso.org/observing/dfo/quality/MIDI/qc/calibrators_obs.html

lack of correction for the dispersion effects due to PWV is therefore transferred to the errors on our phases.

A word of caution must be issued concerning the MIDI spectra. The water vapor content in the Earth atmosphere can change conspicuously on a timescale of half an hour without any changes in seeing or coherence time. So, it is possible that the water vapour content and thus the transmission of the Earth atmosphere changes between science and calibrator. Whereas the calibration of the interferometric visibility is not affected, the fluxes (i.e. the MIDI spectra) are affected. To limit such ef-

fects, fluxes were only derived if the airmass difference to the science target was smaller than 0.2 and the calibrator was observed within ± 2 hours from the science target. Only calibrators of spectral type earlier than M0 were selected for the flux calibration. Henceforth the possibility that the science spectra is contaminated by possible dust around the calibrator is minimised (Chesneau 2007). Adding the LP to the archive data (Sect. 2.4), we collected a total of 201 visibility points; 60% of these data were of good quality and were used in this work.

2.4. Additional observations and variability check

Archive MIDI observations were available for TX Psc, AQ Sgr, U Ant, T Mic, R Crt, R Leo, RT Vir, π^1 Gru, omi Ori, and R Lep. Some of these data were observed in GRISM mode (spectral resolution $R = 230$). These high resolution archive observations were convolved to a spectral resolution $R = 30$ before any comparison with the LP data. We also noticed that most of these observations were carried out with different baselines but at the same position angle. Such data sets allow us to probe the atmosphere at different spatial scales, i.e. these data sets are optimal for tomography studies. Moreover these observations carry information about intra-cycle and cycle-to-cycle interferometric and spectroscopic variability. When possible we assigned a variability phase calculated from the visual light curve to every MIDI observation. For this purpose light curves were collected from the American Association of Variable Star Observers (AAVSO), the All Sky Automated Survey (ASAS), and the Association Française des Observateurs d'Étoiles Variables (AFOEV). The phase is determined from the light curve using the following relation:

$$\phi = \frac{(t - T_0)}{P} - \text{int}\left(\frac{(t - T_0)}{P}\right),$$

where t stands for the date of the MIDI observation(s) expressed in Julian date, T_0 is the phase-zero point that was selected as the maximum light closest in time to the first MIDI observation, and P is the period of variability already listed in Table 1. Visual phases are assigned to the stars θ Aps, R Crt, R Leo, T Mic, RT Vir, R Lep, Y Pav, S Sct, and AQ Sgr. The values are listed in Appendix B, and errors are assumed to be of the order of 10% of the period.

The analysis of spectroscopic variability is performed by comparing MIDI spectra obtained at different visual phase, and also by comparing the MIDI spectra to available ISO and/or IRAS spectra. The interferometric variability was studied by comparing (when available) sets of visibilities at similar baseline lengths and position angles, observed at different dates. If no interferometric variability is detected, one can assume that the data can be combined for the geometric fit. The (u, v) -coverages obtained for all the data of the LP, including the archive data is shown in Fig. 2.

3. Geometric fitting

A model-independent way to identify departure from spherical symmetry of the CSE is by comparing visibilities taken at similar baseline and different position angle. We performed this check where the data set allowed it. As a second approach we employ the software GEM-FIND (GEometrical Model Fitting for INterferometric Data; Klotz et al. 2012b) to interpret our observations. This software fits geometrical models to interferometric visibility data, where different spherically symmetric, centrosymmetric, and asymmetric models are available. The different parameters of the models can be either wavelength dependent (e.g. diameter, flux ratio of two components) or wavelength independent (e.g. inclination or axis ratio of a disk) as GEM-FIND fits each wavelength point separately. This gives us the possibility to study the dependence of the model parameters on, for example molecular and dust features. The output of GEM-FIND is a χ^2_{red} , the best-fitting parameters, and wavelength-dispersed visibilities and differential phases. The errors of the best-fitting

parameters given by GEM-FIND are the 1σ statistical errors derived from the covariance matrix (calculated within the MPFIT³ IDL routines implemented in GEM-FIND). It is known that the models in the Fourier space are not linear, therefore the errors are not Gaussian distributed. We tested the validity of the approach with Monte Carlo simulations (Klotz et al. 2012b). We find that 1σ errors from the Monte Carlo simulations are comparable to those derived from the covariance matrix. Therefore, in the following, errors are computed from the covariance matrix.

For the study of the geometry of the circumstellar environment, the following models were used to fit the data: circular uniform disk (UD, representing an approximation of the stellar disk), circular Gaussian distribution (Gauss, approximation to an object with a molecular or dusty environment and limb darkening), elliptical uniform disk (Ell. UD, such as in the UD case with non-central symmetric brightness distribution), elliptical Gaussian distribution (Ell. Gauss, such as in the Gauss case with non-central symmetric brightness distribution). The latter two models were applied only for the objects with more than two position angles available. In the case where a sufficient number of observations sampling different spatial frequencies were available, a spherical two-component model (a circular UD plus circular Gaussian, where the two components typically represent the photosphere and an optically thin dust and/or molecular component) was used additionally. In this latter case the diameter of the UD was fixed to a value corresponding to the $\theta_{(V-K)}$ diameter (van Belle et al. 1999) to simulate the central star (or to the observed K -band value, when available). Only the Gaussian envelope was fitted. The fit with GEM-FIND was performed in two stages: first only the LP data are fitted, and afterwards the LP data are merged with the archive data and a new fit is performed. The reasoning behind this strategy is that the LP data are chosen to sample the same spatial frequencies and different position angles, therefore they are more suitable for detecting possible elongations owing to a non-central symmetric distribution. The fit with all data (LP + archive) is performed for completeness, and it allows us to study the stratification of the stars.

4. Results

This section summarises the general findings of the LP. Detailed discussion for the single targets are given in Appendix A.

4.1. Visibility versus wavelength

A visual inspection of the visibility spectrum reveals certain spectral features characterising the chemical composition of the CSE. For this study, we inspect the visibilities in the range between $0.1 \lesssim V \lesssim 0.9$. In the case of $V \geq 0.9$, it is not possible to distinguish details of the spectral signature, or even distinguish the visibilities from those of a point source owing to the typical errors. At $V \lesssim 0.1$ the relation between visibility and spatial frequency may not be univocal (as the visibility function may consist of several lobes). Fig. 3 shows the spectrally dispersed visibility curves for stars with different chemistry.

M-type and S-type stars. The most prominent molecular feature of oxygen-rich stars in the N band is SiO around $8 \mu\text{m}$. In some cases, this is followed by silicates and Al_2O_3 dust. For stars not showing a pronounced silicate feature such as R Leo (upper left panel of Fig. 3), T Mic, and the S-type stars omi Ori and π^1 Gru (upper right panel of Fig. 3), the visibility is rather

³ <http://pur1.com/net/mpfit>

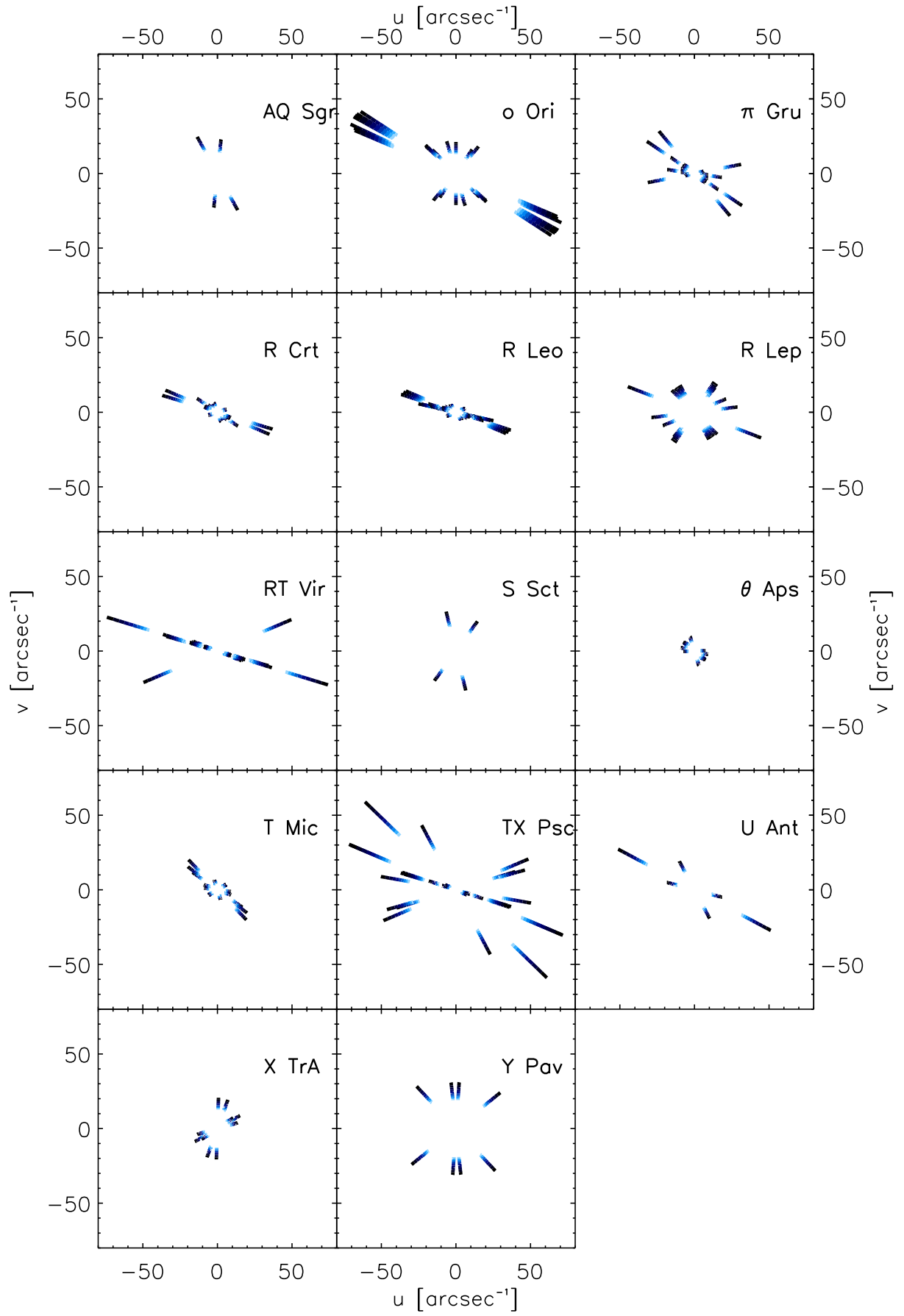


Fig. 2. (u, v) coverages obtained for all the targets. The different wavelengths from 8 – 13 μm are colour-coded (dark to light, respectively).

Table 3. Reduced χ^2_{red} from GEM-FIND fitting.

Target	Baseline [m]	Year	N_{OB}	UD	Gauss	Ell. UD	Ell.Gauss.	UD+Gauss
θ Aps	10–17	2011/12	6	0.78	0.69	0.41	0.38	...
R Crt	10–16	2012	5	10.17	2.53	1.18	1.04	...
	10–64	2009/11/12	8	46.27	28.31	18.18	17.74	0.69
R Leo	11–16	2012	4	0.93	0.78	0.09	0.11	...
	11–64	2006/07	18	38.55	14.73	8.03	10.84	7.17
T Mic	11–16	2011	4	0.28	0.27	0.09	0.11	...
	11–46	2004/11	7	1.16	0.96	0.49	0.46	0.24
RT Vir	13–15	2012	2	1.31	1.13
	12–128	2008/09/11/12	14	49.10	25.13	22.80	20.51	3.04
π^1 Gru	10–15	2011	3	4.83	3.44	0.57	0.42	...
	10–62	2006/11	11	23.23	23.56	21.59	21.49	0.73
σ^1 Ori	32–46	2011	7	1.30	1.30	0.79	0.78	...
	32–129	2005/11	14	2.04	2.01	1.90	1.85	1.43
U Ant	30	2012	1
	30–95	2008–2012	3	1.20	1.23	0.65	0.63	...
R Lep	34–40	2012	6	1.59	0.93	1.32	0.90	...
	34–79	2011/12	10	2.38	3.65	1.39	3.55	0.96
Y Pav	50–63	2011	4	0.77	0.78	0.44	0.44	...
TX Psc	60–140	2011	6	0.99	1.19	0.90	1.09	...
	11–140	2004–2011	15	1.28	1.32	1.29	1.32	1.34
S Sct	40–45	2011	2	2.63	2.61
X TrA	21–34	2011	5	0.95	0.89	0.31	0.30	...
AQ Sgr	37–42	2011	2	2.39	2.47

Notes. The range in baseline length is given as 'Baseline'. The number of observations used for the fitting is given as N_{OB} . The first row corresponds to the data of the LP. The second row corresponds to fits where the LP and archive data were merged. If only data points with similar position angles were available, the elliptical models were not fitted. The χ^2_{red} of the model best fitting the data is highlighted in boldface. The resulting best-fitting parameters are given in Table 4, whereas the dates of the observations are given in Appendix B.

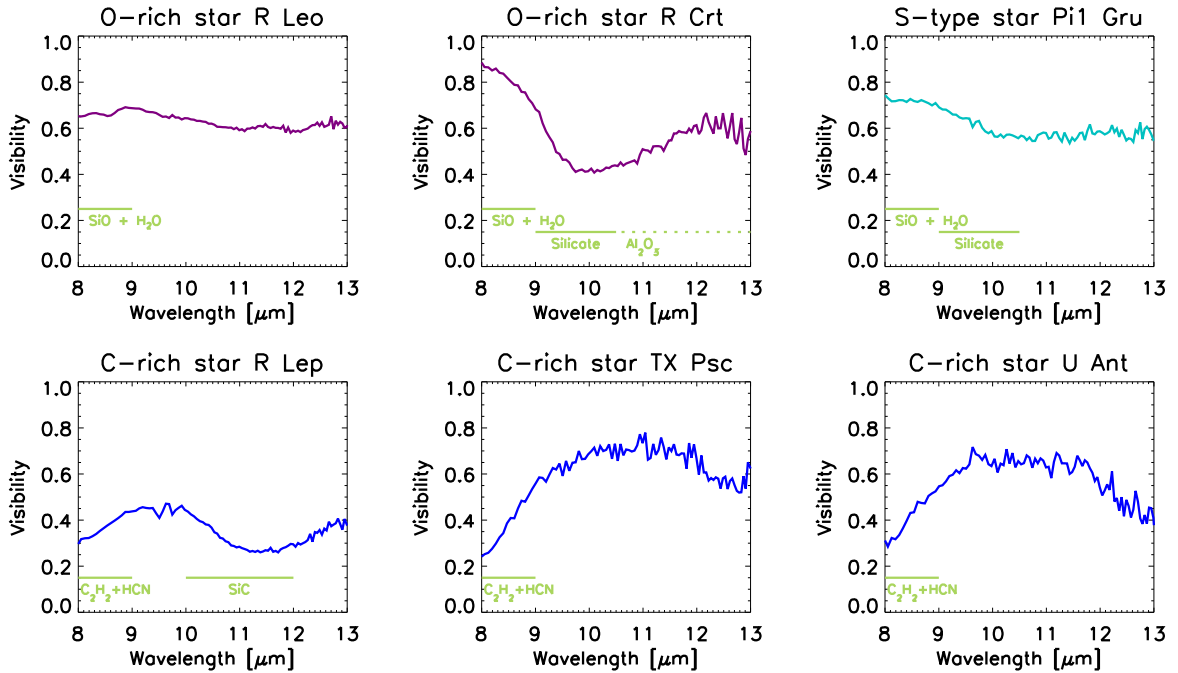


Fig. 3. Some examples of visibility spectra for given baselines. The complete sample can be found in Appendix A. Molecular and dust features are highlighted for stars with different chemistry: R Leo and R Crt are M-type stars, π^1 Gru is an S-type object, while R Lep and TX Psc are C-type stars. The lower right panel shows an example of the visibility spectra of the carbon star U Ant (cf. Sect. 4.1). The typical error bars are of the order of 10%.

flat with a small bump at short wavelengths. The diameter increases slightly at longer wavelengths. For stars showing the dust and molecular features (R Crt shown in the central upper

panel of Fig. 3; RT Vir, and θ Aps) the visibility has a peak in the 8-9 μm region, a decrease of between 9-11 μm , and a subsequent increase.

C-type stars. The molecules contributing to the carbon stars opacity in the N band are mainly C_2H_2 and HCN. Concerning the dust, evolved carbon-rich objects show SiC dust at 11.3 μm and amorphous carbon dust (featureless). Examples of visibilities of stars with SiC dust were shown by e.g. Ohnaka et al. (2007), Sacuto et al. (2011), Paladini et al. (2012), and Rau et al. (2015). The lower left panel of Fig. 3 shows the visibility of the C-rich Mira R Lep with the typical drop at 11.3 μm because SiC. Y Pav, X Tra, and AQ Sgr show similar visibility curves. The visibilities of carbon-rich stars *without* SiC have a typical bow shape. The visibility gets lower (i.e. the star is larger) between 8-9 μm and after 12.5 μm where the molecular opacity is higher. Fig. 3 shows an example of this kind of star, i.e. TX Psc (also presented in Klotz et al. 2013).

Other stars. The IRAS and MIDI spectra of U Ant show the signature of SiC dust feature, while there is no trace of such a feature in the (spatially resolved) interferometric observations (lower right panel of Fig. 3). This could be the result of resolving out part of the total emission, only revealing the emission of the spatial scale to which the interferometer is sensitive (at the employed baselines).

The case of S Sct is slightly different. There is no trace of SiC in the (spatially resolved) interferometric observations nor in the MIDI spectrum. The dust feature is observed in the ISO spectrum recorded 14 years before the LP observations. The IRAS spectrum of S Sct obtained ~ 30 years before is very noisy but seems to agree with the MIDI spectrum (Fig. A.21). The latter was derived by averaging data taken on two different days, therefore one should be able to rule out a problem with the calibration. The S Sct observations suggest a temporal variability in the stratification of SiC.

To our knowledge it is the first time that such findings are reported for AGB stars. Section 5 provides a detailed discussion of these findings.

4.2. Differential phase

Except for the cases where the differential phase is equal to 180°, and/or it is accompanied by a null value in the visibility, a non-zero differential phase measured by MIDI implies an asymmetric brightness distribution. The latter can be explained by two effects (Tristram et al. 2014): first, the object is composed of two sources (for example, the photosphere and resolved dust component) with different spectral distribution through the N band; and, second, the object is composed of two objects with a spatial distribution more resolved at a certain wavelength than at another across the N band. In nature we usually observe a mixture of these two effects, which are very difficult to distinguish, unless one has enough information for detailed modelling or to attempt an image reconstruction. Non-zero differential phase was observed in a few AGB stars. Usually this is interpreted as a typical signature of a disc (Kervella et al. 2014; Ohnaka et al. 2008a; Deroo et al. 2007) or the signature of a clump (Sacuto et al. 2013; Paladini et al. 2012). Since modelling very few differential phases gives highly non-unique solutions, no attempt to interpret the differential phase is carried out here.

We report non-zero differential phase only for two objects: R Leo and RT Vir (Figs. 4 and 5). The morphology of the differential phases of R Leo can be classified in two groups, according to the projected baseline used for the observations. The three upper panels of Fig. 4 show a jump of the differential phase around

9 μm . These data are acquired at different times (see Sect. 4.3), at the same position angles, and very similar projected baselines. The lower panels show a much more complex behaviour with features at ~ 10 and $\sim 11.8 \mu\text{m}$.

The differential phase of RT Vir shown in Fig. 5 is characterised by a jump between 8 and 9 μm , followed by a monotonic increase. For an interpretation of the RT Vir differential phase with a geometric model, we refer to Sacuto et al. (2013).

All the non-zero differential phases occur at visibility spectra below 10%.

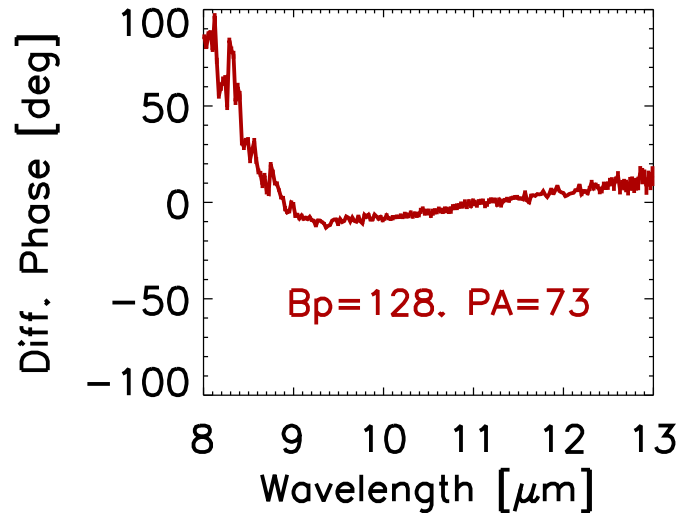


Fig. 5. Same as Fig. 4 for RT Vir.

4.3. Spectroscopic and interferometric variability

As already mentioned in Sect. 2.4, we used archive spectroscopic and interferometric observations to study the N -band variability.

The spectroscopic variability typically corresponds to the variation in the colour (temperature) or a specific variation in certain line strength. On the other hand, the interferometric variability is usually connected with a change in the morphology of the object, in particular the spatial scale of the N -band emission region. Of course the real picture is more complex, and interferometric variability might also be due to brightness variation. When the stellar atmosphere is spatially resolved, and there are multiple components in the FOV of the interferometer (i.e. photosphere plus extended molecular/dust layer, or photosphere plus clumpy structures), it is possible to observe variation in the visibility (at the same spatial frequency) because of a change in the flux ratio between the two components.

In Fig. 6 we compared the level of the MIDI spectra with ISO and IRAS spectra (when the ISO observations were not available). The ISO and IRAS observations are taken approximately 30 years apart from the MIDI observations. Such a comparison can in principle provide information around long-time variability due to dust formation and/or mass-loss variation. On the other hand, this can be caused by the FOV difference between the various telescopes. The FOV of the MIDI observations is $\sim 2.3'' \times 1.6''$, and it is smaller than the FOV of IRAS and ISO, $45'' \times 45''$, and $33'' \times 20''$, respectively). Only a detailed modelling is able to distinguish between these effects. Such modelling is beyond our scope, and we simply report cases of suspected variability and leave the modelling to a future investigation (Rau et al. 2017, in press).

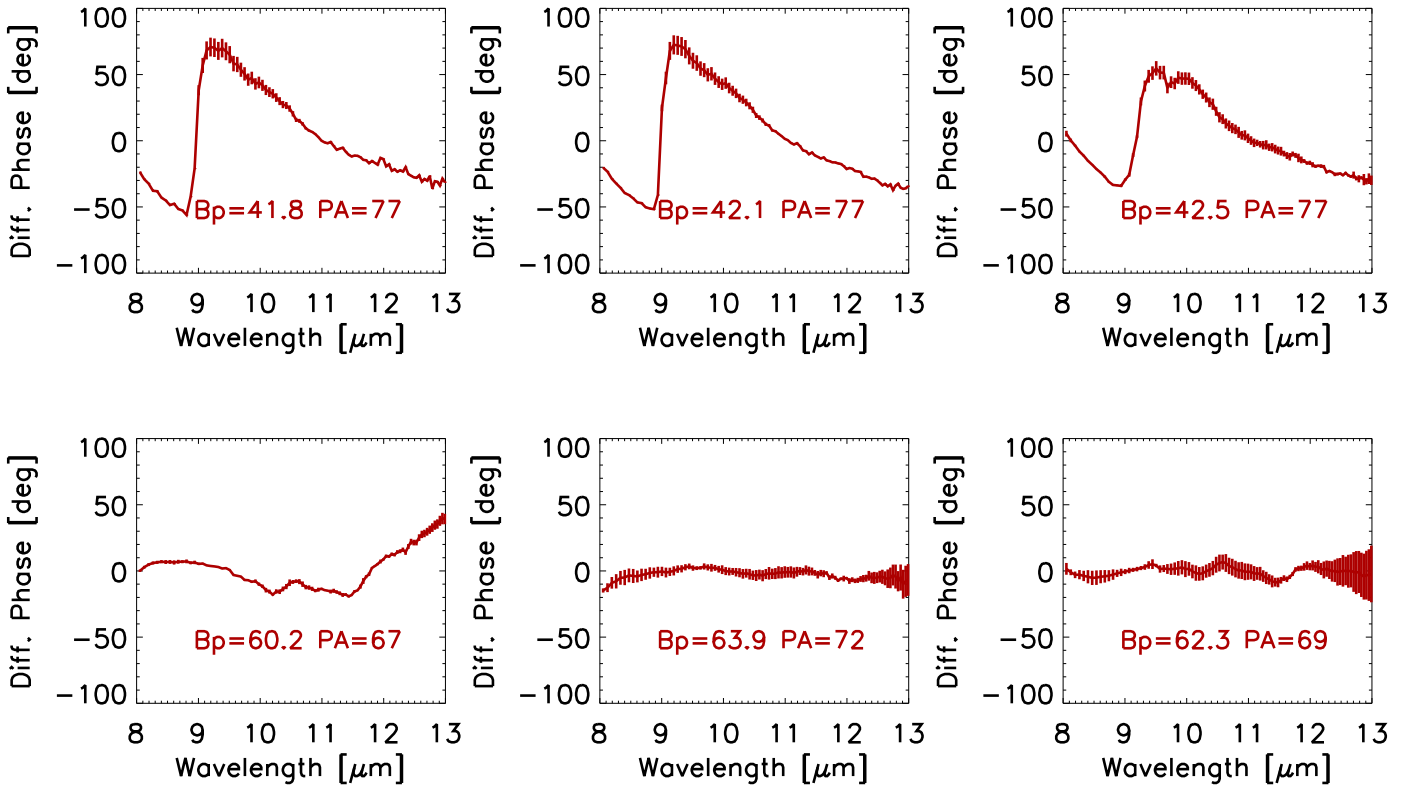


Fig. 4. Non-zero differential phases measured by MIDI for R Leo ordered in increasing projected baseline (B_p).

We observe that 3 stars out of 13 have a mid-infrared flux very similar to the IRAS flux (U Ant, omi Ori, and R Crt). AQ Sgr, Y Pav, RT Vir, and T Mic have a flux level below that observed by ISO/IRAS. The shape of the spectrum is usually consistent, with an exception made for Y Pav where a calibration problem cannot be excluded. This hypothesis is also supported by the fact that in the Y Pav spectrum, one can still see the telluric ozone feature at $9.7 \mu\text{m}$.

For R Crt, R Leo, R Lep, and RT Vir, we had several MIDI spectra observed at different visual phases. By plotting the flux at various wavelengths ($8, 10$, and $12 \mu\text{m}$) versus visual phase, we study the intra-cycle and cycle-to-cycle variability of the star (Figs. A.3, A.5, A.9, and A.15). R Crt shows no significant variability (Fig. A.3). R Lep and R Leo show variations. RT Vir is by far the star with the best coverage in phase. The variation of the flux over the pulsation period resembles a sinusoid (Fig. A.9). The flux variation within the cycle corresponds to an amplitude of variability of 0.48 mag at $8 \mu\text{m}$, and 0.75 mag at 10 and $12 \mu\text{m}$.

The interferometric variability of the visibility spectrum was studied only for θ Aps, R Leo, RT Vir, and R Lep. The intra-cycle observations of the carbon-rich mira R Lep are taken at very similar visual phases (0.01 difference), therefore it is not a surprise if no interferometric variability is detected (Fig. A.16, left panel). However, a cycle-to-cycle variation is observed in the level of the visibility spectrum (Fig. A.16, right panel). The variation is more pronounced in the molecular dominated region between 9 and $10 \mu\text{m}$. We do not observe variation between 11 and $12 \mu\text{m}$, where SiC is located. The visibility level is higher before the visual phase minimum ($\phi_V = 1.43$), corresponding to a smaller diameter.

Neither θ Aps and RT Vir show any evidence of variability in the visibility spectrum. Two sets of data are available to check

the interferometric variability for R Leo. The first set includes three observations taken with the short baseline configurations. The visibility level is ~ 0.6 ; the observations are taken at similar visual phases, but one of them was observed six cycles before. No variability is observed for this set of data (Fig. A.6, left panel). The second set of data also includes three data points, but the first two were averaged because they were taken within two consecutive days (with very similar PA and projected baseline). The observations are shown in the right panel of Fig. A.6 and the difference between the visual phases is 0.13 . It is obvious that in this case we observe a variation in the visibility level from one visual phase to the other. However these observations are associated with a differential phase signature (Fig. 4, upper row). The differential phase also changes from one set of observations to the other.

4.4. The geometric fitting results

Large Programme data only. As a first step the geometric models are only fitted to the LP data. As described in Sect. 2.2, the LP observations sample very similar spatial frequencies (i.e. the same part of the star) at different position angles. In Table 3, for each star, we present in the first row the results of the fit on the large-programme data only. The model with the χ^2_{red} closest to 1 is considered as the one best fitting the data, and it is highlighted in bold in Table 3. The elliptical models have been tested for 10 objects out of 14 because in some cases not enough data points were available. One oxygen-rich star (R Crt) out of the 4 tested with elliptical models is asymmetric. Both S-type objects (π^1 Gru and omi Ori) also show indications of ellipticity from the GEM-FIND fit. Out of the sample of 4 carbon-rich objects that were tested, none turned out to be asymmetric. It has to be stressed out that an elliptical solution does not necessarily

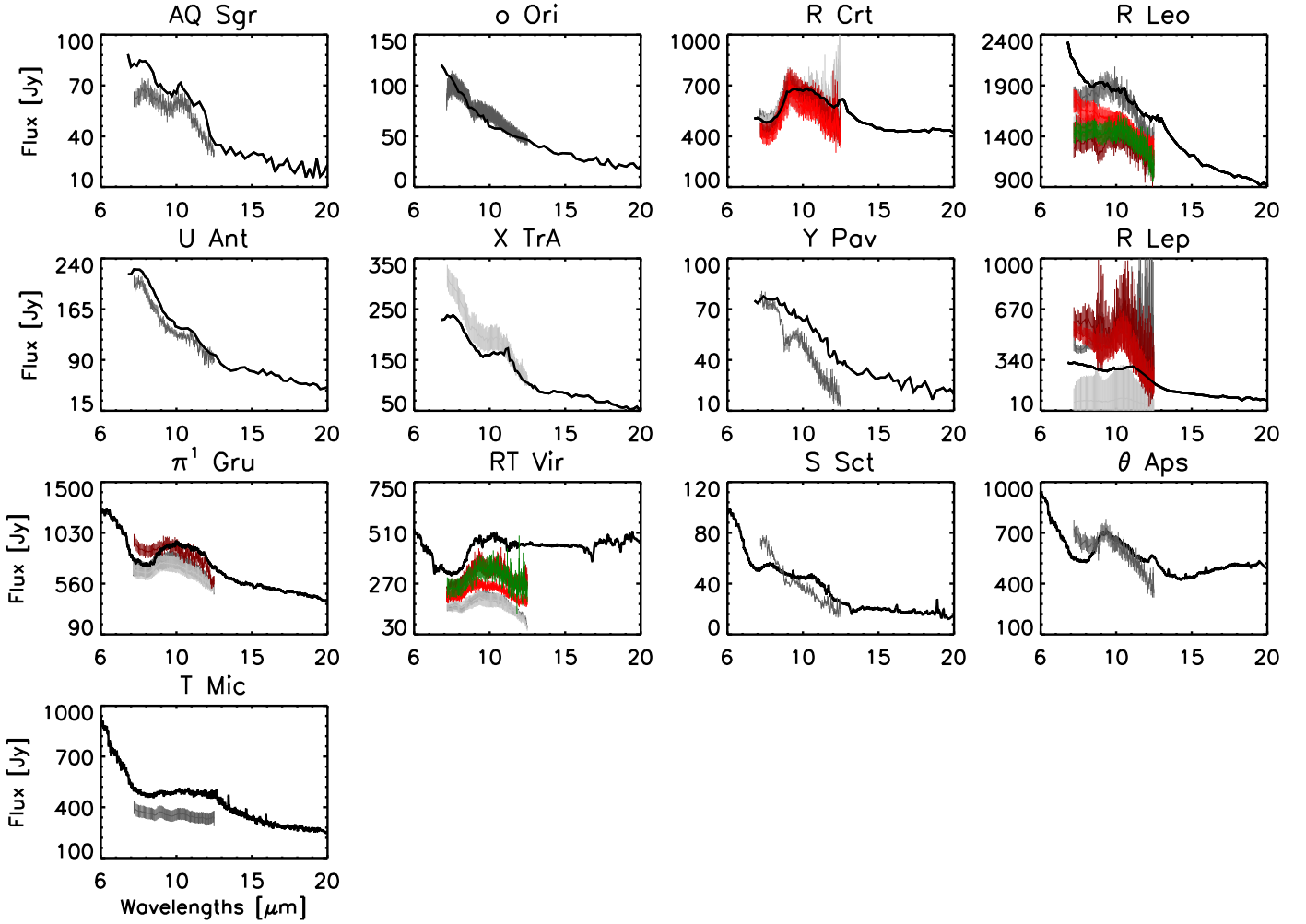


Fig. 6. IRAS or ISO spectra (black lines) compared with the MIDI spectroscopic observations (shaded areas).

imply that the environment has a truly elliptical shape. It only means that the CSE is non-central symmetric. More complex geometries than ellipses cannot be excluded.

Large Programme & archive data. Nine stars of our sample have archive data, and two of these stars have non-zero differential phases. There are, therefore, a total of five targets showing evidence of asymmetric environment. All these asymmetric stars have O-rich chemistry and are located in the lower part of the IRAS colour-colour diagram, as shown in panel a) of Fig. 7.

After excluding interferometric variability, we combined the data of the LP with those obtained from the archive. Besides R Lep and TX Psc, all the other stars have archive data that sample mostly the same position angle but at different spatial scales. As already stated in Sect. 2.4, such data are optimal for studying the stratification of the star, but they are obviously less sensitive to asymmetries. Exception made to TX Psc, every time archive data are added to the fit, the composite (UD plus Gaussian) model turns out to be the best-fitting model (Table 3). This implies that the stars have an extended environment because of molecular and/or dust opacities. We note that the additional archive data *wash away* the elliptical solution for all the three objects mentioned at the beginning of this section. This is a consequence of the fact that the additional data always have the same position angle. Because these additional data are more numerous than the LP data, they drive the fit solution towards

symmetric solutions; but this result certainly does not imply that the asymmetry detected by the dedicated LP data must be considered spurious. Very likely the best-fitting model would be an elliptical UD+Gaussian, but this model has too many free parameters to be tested versus our data set. By looking at the LP+archive fitting results of Table 3, one notes the following: six stars are best fit by the composite model UD+Gauss, i.e. six stars have an extended, optically thin, component. However, it is possible that by adding more visibility points, other objects also increase in complexity and they are best fitted with a composite geometric model. This is very likely for X TrA, AQ Sgr, θ Aps, and Y Pav where the coverage of the visibility spectrum does not extend below 0.6. Given the fact that no dust feature is detected around S Sct, we expect that the visibility spectrum are reproduced only with one component, even by adding other visibility points. So far, in our sample only TX Psc has a visibility that goes down to $V \sim 0.2$ without showing departure from uniform disc: no dust envelope is detected. The carbon stars in region VIa, following the loop for the carbon stars, can be fit with single component models and are supposed to be younger than those located in region VII. The only carbon mira of the sample is fit with the composite model in region VII. All the objects in region VIa do not show SiC in the visibility. The geometry of the CSE increases in complexity from left to right, where this

complexity could be caused by dust or an increased asymmetry of the CSE.

4.5. The diameters

In Sect. 2.2 the strategy for choosing the baseline that allows us to resolve the dust-forming region was explained. One of the output of the GEM-FIND fitting is the diameter (or the full width half maximum for the Gaussian profile) of the object in the fitted wavelength. If one assumes that the UD or Gaussian are a crude approximation of the stellar disk, then one can hazard a comparison between the diameter computed from the $V - K$ relation and that derived in the N band via geometric fitting. Such a comparison is presented in Table 4. The photospheric angular diameter (see Sect. 2.2) calculated from the $V - K$ relation (van Belle et al. 1999) are shown in Col. 2, while in Col. 3 we list (when available) the measured $K - band$ values. Column 4 lists the best-fitting GEM-FIND model. Columns 5 and 6 report the value of the angular UD-diameters and/or FWHM resulting from the geometric fitting at $8 \mu\text{m}$. Whereas the best-fitting model is the composite model (UD+Gauss; Table 3), both θ and $FWHM$ values are given. In the latter case we do not indicate the error on the UD diameter to point out that in the composite model we kept the value of the UD fixed to the θ_{V-K} or to the observed K -band value (see Sect. 3). Columns 7, 8, 9, and 10 are the same as Cols. 5 and 6 at 10 and $12 \mu\text{m}$. The photospheric diameter and the $8 \mu\text{m}$ UD diameters (FWHM) are converted in linear sizes in Cols. 11 and 12 (Col.13), respectively. Finally, in Col. 14 we list the ratio between the $8 \mu\text{m}$ UD diameter (FWHM in the cases when Gaussian or the composite model is the best-fitting model) and the photospheric diameter. The comparison between the ratios is not straightforward because of the mix of UD and FWHM sizes, but overall most of the diameters at $8 \mu\text{m}$ are of the order of two times the photospheric diameter. The exceptions are the two S-type stars, the carbon Mira R Lep, and AQ Sgr, which have a much larger environment ($> 2.4 D_{V-K}$). T Mic and Y Pav have a diameter ratio that is smaller than one, indicating that the environment is very similar to that observed in the near-infrared. Another explanation could be that the θ_{V-K} diameter of these two stars is overestimated. Diameters at longer wavelength are even larger with some extreme cases for the more dusty stars such as R Crt and RT Vir. The diameters *ratio* obtained for the carbon stars are in general agreement with the ratio between the photospheric and 8-9 μm diameters predicted by dynamic model atmospheres (Paladini et al. 2009, Fig. 6). The sizes here derived are intended as a guideline for the preparation of future interferometric imaging campaigns. Detailed radiative transfer helps constrain the molecular and dust stratification, and will be performed in follow-up studies.

5. Discussion

5.1. Silicon carbide dust

Silicon carbide is a dust species observed around carbon stars. The typical signature in the spectrum is an emission feature at $\sim 11.3 \mu\text{m}$. The condensation temperature (and condensation radius) of SiC is matter of investigation, however there is increasing evidence that for galactic AGB stars SiC condenses at similar temperatures as (amorphous) carbon dust (Lagadec et al. 2007).

As a matter of fact, up to now, all the carbon stars observed with MIDI that were showing SiC in the spectrum, always had a signature of such dust component in the visibility (Ohnaka et al.

2007; Sacuto et al. 2011; Paladini et al. 2012; Zhao-Geisler et al. 2012; Rau et al. 2015).

van Boekel et al. (2004) showed the case of protoplanetary discs where the (normalised) correlated flux spectrum (or visibility spectrum) reveals certain chemical features that are not detected in the total flux spectrum. The MIDI observations of U Ant show a similar behaviour, although in this specific case the chemical feature (SiC) is present in the total flux and not in the correlated one.

Assuming that SiC forms in a uniform shell expanding because of a slow wind, then this shell will be not visible if (i) it is smaller than the resolving power of the interferometer, or (ii) if the contrast between the shell and the main source is very low. The maximum resolving power is given by the longest baseline, and in the case of the U Ant observations it corresponds to $\lambda/(2 \times B_{\text{max}}) = 11 \text{ mas}$ at $10 \mu\text{m}$. Since 10 mas is the diameter of the photosphere, it sounds more reasonable to believe that the SiC shell is optically thin. Further constraints can be given with detailed radiative transfer modelling and future observations with baselines longer than 95 m.

The MIDI observations (correlated and uncorrelated flux) of S Sct point to variability in the SiC abundance. We searched in the literature for possible variation in the mass-loss rate values to test if a recent strong stellar wind event might have pushed away or dissolved the SiC dust. No such event was reported within recent decades. A spectrum with VISIR is needed to confirm the lack of SiC in the uncorrelated MIDI flux and to eventually monitor the changes in abundance.

5.2. The variability

Mid-IR flux changes of up to 30% with less flux observed at the minimum visual phase are reported by Karovicova et al. (2011); Wittkowski et al. (2007), and Tevousjan et al. (2004). Monnier et al. (1998) studied multi-epoch mid-infrared spectra of 30 late-type stars and found that stars with a strong silicate feature exhibit spectral shape fluctuations, where a narrowing of the feature is detected near maximum light. They report that R Leo shows unusually large spectral shape variations that may be attributed to a dynamic dust condensation zone. Although based only on four targets, our findings on the N -band spectroscopic variability largely confirm previous literature results. The flux variation of RT Vir, which is the star in our sample with the best temporal coverage, is comparable to the amplitude of $\sim 0.8 - 1 \text{ mag}$ found by Le Bertre (1993) for O-rich mira stars.

Interferometric variability was so far observed in the carbon-rich miras V Oph (Ohnaka et al. 2007) and R For (Paladini et al. 2012). While the variability is interpreted as connected to pulsation for V Oph, the presence of an asymmetric structure plays a role for R For. The variability we observe in the case of R Lep is just within the 3 sigma uncertainties, however it goes in the same direction of the literature findings. The visibility level suggests that R Lep is smaller close to the minimum visual phases, similar to V Oph (Ohnaka et al. 2007), and model predictions at $10 \mu\text{m}$ showed in Fig. 7 of Paladini et al. (2009). Model predictions for O-rich Mira stars presented in Karovicova et al. (2011) show that the expected visibility changes with visual phase are wavelength dependent and in the range of 5 – 20%. During the pulsation phase, the largest difference within the N band is predicted at around $10 \mu\text{m}$. Karovicova et al. (2011) argue that these limited variations are because the sizes of the molecular and dust layers do not change significantly with visual phase. According to the authors, the changes are within their measurement uncertainties. The star observed by Karovicova et al. (2011) is a Mira

Table 4. Predicted, observed diameters, and geometric characteristics.

Target	θ_{V-K} [mas]	θ_K [mas]	GEM-FIND	$\theta_{UD,8}$ [mas]	FWHM ₈ [mas]	$\theta_{UD,10}$ [mas]	FWHM ₁₀ [mas]	$\theta_{UD,12}$ [mas]	FWHM ₁₂ [mas]	D_{V-K} or D_K [AU]	$D_{UD,8}$ [AU]	$D_{FWHM,8}$ [AU]	ratio
θ Aps	24	18.1 ^a	UD	40±5	...	85±3	...	86±5	...	2.0 ^{+0.1} _{-0.1}	4.6 ^{+0.8} _{-0.8}	...	2.24
R Crt	19	...	UD+Gauss	19	38±8	19	162±28	19	89±7	5.0 ^{+1.6} _{-1.6}	...	9.9 ^{+5.3} _{-5.3}	1.99
R Leo	25	...	UD+Gauss	25	49±1	25	50±1	25	57±1	1.8 ^{+0.9} _{-0.9}	...	3.5 ^{+0.9} _{-0.6}	1.96
T Mic	25	...	Gauss	...	36±7	...	55±8	...	64±9	5.3 ^{+1.3} _{-1.3}	4.4 ^{+1.5} _{-1.0}	...	0.84
RT Vir	15	15 ^c	UD+Gauss	15	28±5	15	115±15	15	52±3	2.0 ^{+0.9} _{-0.9}	...	3.7 ^{+1.1} _{-1.0}	1.84
π^1 Gru	28	21.6 ^d	UD+Gauss	21.6	131±52	21.6	172±46	21.6	179±31	3.5 ^{+0.3} _{-0.3}	...	21.4 ^{+11.5} _{-10.3}	6.36
omi Ori	11	9.78 ^e	UD+Gauss	9.78	214±21	9.78	214±22	9.78	221±22	1.9 ^{+0.3} _{-0.3}	...	42.8 ^{+19.3} _{-9.5}	21.92
U Ant	10	...	UD	16±1	...	12±1	...	17±1	...	2.7 ^{+0.3} _{-0.3}	4.2 ^{+0.8} _{-0.6}	...	1.56
R Lep	9	12.0 ^f	UD+Gauss	12	29±1	12	33±2	12	44±2	5.0 ^{+1.8} _{-1.8}	...	12.0 ^{+9.1} _{-3.9}	2.42
Y Pav	7	...	Gauss	...	5±1	...	5±2	...	12±1	2.8 ^{+0.9} _{-0.9}	...	2.1 ^{+1.3} _{-0.8}	0.76
TX Psc	11	...	UD	12±1	...	10±1	...	12 ± 1	...	3.0 ^{+0.3} _{-0.3}	3.4 ^{+0.5} _{-0.4}	...	1.13
S Sct	7	6.22 ^g	Gauss	...	12±1	...	11±2	...	13±3	2.4 ^{+0.3} _{-0.3}	...	4.5 ^{+1.8} _{-1.3}	1.89
AQ Sgr	6	6.13 ^h	UD	17±3	...	20±4	...	33±3	...	2.0 ^{+0.4} _{-0.4}	5.5 ^{+2.5} _{-2.0}	...	2.70
X Tra	11	...	UD	22±2	...	23±4	...	39±3	...	4.0 ^{+0.4} _{-0.5}	7.9 ^{+3.4} _{-2.0}	...	1.99

Notes. A detailed description of the various columns of the Table can be found in Sect. 4.5. The diameter of carbon stars showing SiC at 11.3 μm is usually comparable to that measured at 8 μm or 12 μm , depending on the visibility level (see Appendix A). ^(a) A dopted from Dumm & Schild (1998) ^(b) S everal diameters ranging between 11 mas (Mennesson et al. 2002) and 27 mas (Perrin et al. 1999) have been published for R Leo. Given the large range of numbers we decided to stick to the θ_{V-K} diameter for our calculations. ^(c) A dopted from Sacuto et al. (2008), and recently confirmed by VLT/PIONIER data (Paladini et al., prep.). ^(d) A dopted from Sacuto et al. (2013). ^(e) A dopted from Cruzalèbes et al. (2013b). ^(f) A dopted from Richichi et al. (2005). ^(g) R recently measured with VLT/PIONIER (Le Bouquin, private communications). ^(h) A dopted from Richichi et al. (2005).

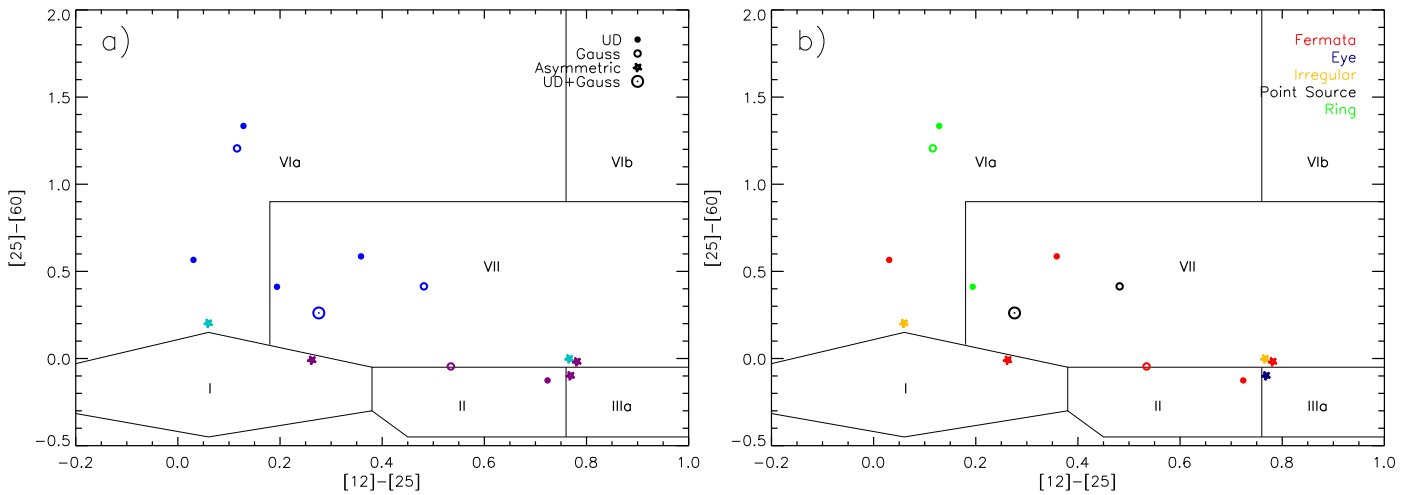


Fig. 7. *Panel a):* our sample of stars in the IRAS colour-colour diagram. The symbols show the results of the GEM-FIND fit. Asymmetric solutions are a result of the fit or due to non-zero differential phase. *Panel b):* same as Panel a) colour coded to highlight the Herschel/PACS morphology observed in Cox et al. (2012).

variable. As these objects are known to exhibit larger variability with visual phase, the size changes for our semi-regular stars (all except R Leo) are expected to be even smaller. In fact, the RT Vir and R Crt data suggest that interferometric variability for semi-regular O-rich stars should be less than 10%. The interferometric variability of R Leo reported here is associated with a non-zero differential phase, as in the case of R For (Paladini et al. 2012), and is therefore very likely caused by (variable) asymmetries. Since low visibilities are more constraining for the size changes, future interferometric snapshot campaigns on temporal variability should concentrate on those projected baselines that are able to probe $V \leq 0.2$.

5.3. The geometry

One may wonder why only two objects out of 14 show a non-zero differential phase. Both objects are O-rich M8III giants, the coolest objects of the sample. The fact that the two stars appear in a completely different part of the IRAS colour-colour diagram could be due to different masses, hence mass loss. What the observations of these stars also have in common are the spatial scales probed. In both cases the differential phase is detected while sampling visibilities below 0.2. Looking at our whole sample, these spatial scales are also probed in two observations of the carbon Mira R Lep. The differential phase is $< 10^\circ$, hence we conclude that R Lep is spherical (at least at $PA = 48^\circ$ and 248°). There have been only a few cases of non-zero differential phase in the literature detected with MIDI; these cases are R For (Paladini et al. 2012), BM Gem (Ohnaka et al. 2008a), IRAS+18006-3213 (Deroo et al. 2007), and L₂ Pup (Kervella et al. 2014). All these observations also had in common the fact of probing visibilities < 0.2 . Thereupon we can assume that the lack of detection of non-zero differential phase does not necessarily exclude the existence of asymmetries in the brightness distribution in the other targets of our sample. Very likely asymmetric structures show up in the differential phase when probing high spatial frequencies, similar to what is reported in the near-IR (Ragland et al. 2006; Cruzalèbes et al. 2013b).

If we include the objects with a differential phase signal, then $\sim 57\%$ of the stars with O-rich chemistry (O-type plus S-type stars) have a CSE geometry that is consistent with being an

asymmetric structure. These results suggest that asymmetries in the dusty environment are more common among the oxygen-rich objects. Near-infrared investigations of AGBs (Ragland et al. 2006; Cruzalèbes et al. 2015), on the other hand, indicate that asymmetries are more common among carbon stars. This result can be explained with the large-grains scenario for O-rich stars (Höfner 2008). Oxygen-rich dust grains are nearly transparent in the near-infrared, therefore not many brightness asymmetries are expected at those wavelengths. The dusty region of O-rich stars probed in the mid-IR should be more "blobby" than for C-rich stars because there are stronger non-linear effects in radiative acceleration. This is valid *if* the scattering on transparent grains scenario is correct; in fact scattering depends much more steeply on grain size (S. Höfner, private communications). Bipolar objects on the post-AGB are mainly O-rich (Lagadec et al. 2011). The latter well agrees with our results on the AGB.

The result obtained by fitting only the LP data, plus the results of the differential phase study, indicate that asymmetries in the dust-forming region are concentrated in the lower part of the IRAS colour-colour diagram. No object located in region VII so far showed asymmetries. More observations covering long baselines (high spatial frequencies), or (ideally) *N*-band images obtained with the next generation VLTI/MATISSE instrument (Lopez et al. 2006) are needed to confirm this finding.

5.4. Comparison with the MESS results

The aim of our programme is to observe the evolution of asymmetric structures through the atmosphere of a representative sample of AGBs. For this purpose we selected stars imaged with the Herschel/PACS instrument and we complemented these observations of the large scales of the atmospheres with interferometric VLTI/MIDI observations of the inner spatial scales. Panel d) of Fig. 7 shows the stars of our sample in the IRAS colour-colour diagram. The objects are colour coded to highlight their MESS classification. The symbols are the same as in panel b) and indicate the presence of a non-spherically symmetric environment. Three objects out of the LP sample are classified by Cox et al. (2012) as rings, six are fermata type, two irregulars, one eye, and two unresolved.

All the stars from the ring class are fitted with the one-component geometric model, and no asymmetry is detected in the dust-forming region. For two of these stars (S Sct and U Ant) no SiC dust component is spatially resolved. The dust observed in their spectra might have been pushed away by episodic wind, or it is optically thin. As already mentioned in the previous section, for X TrA we have only a few data points and we cannot exclude that by adding more visibilities the picture will become more complex.

The carbon-rich stars TX Psc and AQ Sgr, plus most of the Herschel images of our oxygen-rich sample, are of fermata type, i.e. show an interaction with the ISM. R Crt is classified as an eye morphology by Cox et al. (2012). However, the fact that R Crt is the only oxygen-rich AGB star in the MESS sample that is of eye shape, and the fact that the eye shape is not very pronounced may indicate that R Crt may also be of fermata type (Cox et al. 2012). If we consider R Crt among the possible fermata, three out of seven of the stars in this class show a direct detection of an asymmetry (via differential phase) or at least a hint of a non-spherically symmetric environment (detected by fitting only the LP data). This indicates that 42% of the stars classified as fermata have an asymmetric dust-forming region, and they all have O-rich chemistry.

The irregular class contains objects with diffuse irregular extended emission. Both the stars classified as irregular are S-type stars, and they can be fitted with two-components model and show non-central symmetric CSE in the LP data.

6. Conclusions and outlook

In this paper, we present mid-IR interferometric and spectroscopic data observed with VLTI/MIDI for a sample of 14 AGB stars. The sample is based on the list of objects observed within the frame of the MESS programme with Herschel PACS (Groenewegen et al. 2011). The aim of our study is to investigate the morphology of the dusty environment of these objects at different spatial scales and to answer the questions: i) Are the asymmetries of the outer CSE intrinsic to the mass-loss process, and are they only due to interaction with the ISM? ii) At which height does the mass-loss process become manifestly non-spherical? iii) How does the geometry of the atmosphere change at the different evolutionary stages (M-S-C stars, and from almost dust free to very dusty objects) within the AGB sequence?

The first question cannot be addressed using only the mid-infrared interferometric data presented here. These data, in fact, scan the stellar atmosphere between 1-2 and 10 stellar radii, and the intermediate spatial scales probed by VISIR are needed to have a connection with the Herschel/PACS images. Nevertheless, we report that all the objects in our sample classified as symmetric rings by Cox et al. (2012) so far have a symmetric dust-forming region. All the objects classified as irregular need a composite model (i.e. they have an extended environment), and the fit of the LP data indicates some asymmetric behaviour. Approximately 42% of the objects classified as fermata (i.e. show interaction with the ISM) also have an asymmetric dust-forming region.

To answer the second question, it is obvious that asymmetries in the brightness distribution appears already in the dust-forming region of AGB stars. We directly detected asymmetries via differential phase measurement in two cases: RT Vir (already reported by Sacuto et al. 2013), and R Leo. However, the fact that we find the other objects to be symmetric does not preclude the presence of clumps or small or very faint asymmetric structures. GEM-FIND fitting of the LP data shows that beside these

two stars, three more show a hint of non-central symmetric morphology. Concerning the third question, all the stars with asymmetric behaviour have O-rich chemistry. Therefore asymmetric structures in the mid-infrared are more common among O-rich and S-type stars. On the contrary literature suggests that C-rich stars are more asymmetric in the near-IR. We speculate that this result supports the large-grains scenario for O-rich stars.

Another major finding of our programme is that silicon carbide dust is not detected in the correlated flux of S Sct and U Ant. U Ant shows SiC in the total spectrum, and we speculate that SiC is optically thin. The case of S Sct might be related to variability in the stratification of this material.

Finally, by analysing archive data, we studied the spectroscopic and interferometric variability. Spectroscopic variability is reported in a few cases and the flux variations are in agreement with what was already observed in the literature (Le Bertre 1993). An exception is made for the carbon-rich Mira R Lep case, which nevertheless requires confirmation through monitoring campaigns; interferometric variability (i.e. change in the shell size) is observed in the O-rich Mira R Leo. In the latter case the variability is associated with an asymmetry in the brightness profile of the star. The lack of detection for the other stars suggest that interferometric variability in non-mira stars is less than $\sim 10\%$ of the visibility.

The next step of this study will be, as already mentioned, to bridge the gap between MIDI and Herschel with additional single-dish images in the mid-infrared. These observations will be crucial for completing the picture of the morphology of the dusty environment. Finally, MIDI was recently decommissioned, but a second generation instrument VLTI/MATISSE will be available at VLTI in 2018. This interferometer will combine the light from four telescopes, and it will observe in the *L*, *M*, and *N* bands. While MIDI, with only two telescopes, gave us a rough idea of the appearance of the stars within this sample, MATISSE will provide images allowing us not only to detect asymmetric structures, but also to unveil their nature (disk-like or clumps). Because of the complex nature of the targets here studied, a complete coverage of the visibility curve is mandatory. In the *N* band, this will require in certain cases baselines longer than the 150 m (for stars such as omi Ori and TX Psc), but also very short baselines. In this frame, an aperture masking experiment on the VISIR instrument matching the spectral resolution of MATISSE is required.

Acknowledgements. We thank the anonymous referee for comments that helped improving the paper. This work is supported by the Austrian Science Fund FWF under the project AP23006, the Belgian Federal Science Policy Office via the PRODEX Programme of ESA, the Belgian Fund for Scientific Research F.R.S.-FNRS, and the European Community's Seventh Framework Programme under Grant Agreement 312430. This research has made use of the SIMBAD database, operated at CDSm Strasbourg, France, and the Jean-Marie Mariotti Center Aspro service. We acknowledge with thanks the variable star observations from the AAVSO International Database contributed by observers worldwide and used in this research. We thank T. Lebzelter, M. Cesetti, and F. Bufano for helpful comments during the proposal preparation; the ESO Paranal team for supporting our VLTI/MIDI observations; G. C. Sloan for providing the IRAS and ISO spectra; J.-B. Le Bouquin who kindly provided us reduced PIONIER data of S Sct; S. Höfner and K. Tristram for useful discussion.

References

- Ake, T. B. & Johnson, H. R. 1988, *ApJ*, 327, 214
- Begemann, B., Dorschner, J., Henning, T., et al. 1997, *ApJ*, 476, 199
- Bergeat, J. & Chevallier, L. 2005, *A&A*, 429, 235
- Burns, D., Baldwin, J. E., Boysen, R. C., et al. 1998, *MNRAS*, 297, 462
- Chagnon, G., Mennesson, B., Perrin, G., et al. 2002, *AJ*, 124, 2821
- Chandler, A. A., Tatebe, K., Hale, D. D. S., & Townes, C. H. 2007, *ApJ*, 657, 1042

- Chesneau, O. 2007, *New A Rev.*, 51, 666
- Chiavassa, A., Lacour, S., Millour, F., et al. 2010, *A&A*, 511, A51
- Chiu, P.-J., Hoang, C.-T., Dinh-V-Trung, et al. 2006, *ApJ*, 645, 605
- Cox, N. L. J., Kerschbaum, F., van Marle, A.-J., et al. 2012, *A&A*, 537, A35
- Cruzalèbes, P., Jorissen, A., Chiavassa, A., et al. 2015, *MNRAS*, 446, 3277
- Cruzalèbes, P., Jorissen, A., Rabbia, Y., et al. 2013a, *MNRAS*, 434, 437
- Cruzalèbes, P., Rabbia, Y., Jorissen, A., et al. 2013b, *MNRAS*, 432, 1658
- Danchi, W. C., Bester, M., Degiacomi, C. G., Greenhill, L. J., & Townes, C. H. 1994, *AJ*, 107, 1469
- De Marco, O. 2009, *PASP*, 121, 316
- Decin, L., Richards, A. M. S., Neufeld, D., et al. 2014, *ArXiv e-prints*
- Deroo, P., van Winckel, H., Verhoelst, T., et al. 2007, *A&A*, 467, 1093
- Draine, B. T. 1981, in *Astrophysics and Space Science Library*, Vol. 88, *Physical Processes in Red Giants*, ed. I. Iben, Jr. & A. Renzini, 317–333
- Dumm, T. & Schild, H. 1998, *New A*, 3, 137
- Fabian, D., Posch, T., Mutschke, H., Kerschbaum, F., & Dorschner, J. 2001, *A&A*, 373, 1125
- Fedele, D., Wittkowski, M., Paresce, F., et al. 2005, *A&A*, 431, 1019
- Frankowski, A., Jancart, S., & Jorissen, A. 2007, *A&A*, 464, 377
- González Delgado, D., Olofsson, H., Schwarz, H. E., Eriksson, K., & Gustafsson, B. 2001, *A&A*, 372, 885
- González Delgado, D., Olofsson, H., Schwarz, H. E., et al. 2003, *A&A*, 399, 1021
- Groenewegen, M. A. T. & de Jong, T. 1998, *A&A*, 337, 797
- Groenewegen, M. A. T., Waelkens, C., Barlow, M. J., et al. 2011, *A&A*, 526, A162
- Gupta, R., Singh, H. P., Volk, K., & Kwok, S. 2004, *ApJS*, 152, 201
- Habing, H. J. & Olofsson, H., eds. 2003, *Asymptotic giant branch stars*
- Hofmann, K.-H., Balega, Y., Blöcker, T., & Weigelt, G. 2001, *A&A*, 379, 529
- Höfner, S. 2008, *A&A*, 491, L1
- Höfner, S. & Dorfi, E. A. 1997, *A&A*, 319, 648
- Hron, J., Uttenthaler, S., Aringer, B., et al. 2015, *A&A*, 584, A27
- Imai, H., Shibata, K. M., Sasao, T., et al. 1997, *A&A*, 319, L1
- Ireland, M. J., Scholz, M., Tuthill, P. G., & Wood, P. R. 2004a, *MNRAS*, 355, 444
- Ireland, M. J., Tuthill, P. G., Bedding, T. R., Robertson, J. G., & Jacob, A. P. 2004b, *MNRAS*, 350, 365
- Izumiura, H., Hashimoto, O., Kawara, K., Yamamura, I., & Waters, L. B. F. M. 1996, *A&A*, 315, L221
- Izumiura, H., Kester, D. J. M., de Jong, T., et al. 1995, *Ap&SS*, 224, 495
- Jaffe, W. J. 2004a, in *Society of Photo-Optical Instrumentation Engineers (SPIE) Conference Series*, Vol. 5491, *Society of Photo-Optical Instrumentation Engineers (SPIE) Conference Series*, ed. W. A. Traub, 715
- Jaffe, W. J. 2004b, in *Proc. SPIE*, Vol. 5491, *New Frontiers in Stellar Interferometry*, ed. W. A. Traub, 715
- Jorissen, A., Frayer, D. T., Johnson, H. R., Mayor, M., & Smith, V. V. 1993, *A&A*, 271, 463
- Jorissen, A. & Knapp, G. R. 1998, *A&AS*, 129, 363
- Jorissen, A., Mayer, A., van Eck, S., et al. 2011, *A&A*, 532, A135
- Kahane, C. & Jura, M. 1994, *A&A*, 290, 183
- Karovicova, I., Wittkowski, M., Boboltz, D. A., et al. 2011, *A&A*, 532, A134
- Karovicova, I., Wittkowski, M., Ohnaka, K., et al. 2013, *A&A*, 560, A75
- Kerschbaum, F., Ladjal, D., Ottensamer, R., et al. 2010, *A&A*, 518, L140
- Kervella, P., Montargès, M., Lagadec, E., et al. 2015, *A&A*, 578, A77
- Kervella, P., Montargès, M., Ridgway, S. T., et al. 2014, *A&A*, 564, A88
- Kholopov, P. N., Samus, N. N., Frolov, M. S., et al. 1998, in *Combined General Catalogue of Variable Stars*, 4.1 Ed (II/214A). (1998), 0
- Klotz, D., Paladini, C., Hron, J., et al. 2013, *A&A*, 550, A86
- Klotz, D., Sacuto, S., Kerschbaum, F., et al. 2012a, *A&A*, 541, A164
- Klotz, D., Sacuto, S., Paladini, C., Hron, J., & Wachter, G. 2012b, in *Society of Photo-Optical Instrumentation Engineers (SPIE) Conference Series*, Vol. 8445, *Society of Photo-Optical Instrumentation Engineers (SPIE) Conference Series*
- Knapp, G. R., Jorissen, A., & Young, K. 1997, *A&A*, 326, 318
- Knapp, G. R., Pourbaix, D., Platais, I., & Jorissen, A. 2003, *A&A*, 403, 993
- Knapp, G. R., Young, K., & Crosas, M. 1999, *A&A*, 346, 175
- Knapp, G. R., Young, K., Lee, E., & Jorissen, A. 1998, *ApJS*, 117, 209
- Ladjal, D. 2011, PhD thesis, Institute of Astronomy, Katholieke Universiteit Leuven, Belgium
- Lagadec, E., Verhoelst, T., Mékarnia, D., et al. 2011, *MNRAS*, 417, 32
- Lagadec, E., Zijlstra, A. A., Sloan, G. C., et al. 2007, *MNRAS*, 376, 1270
- Lambert, D. L., Gustafsson, B., Eriksson, K., & Hinkle, K. H. 1986, *ApJS*, 62, 373
- Lattanzi, M. G., Munari, U., Whitelock, P. A., & Feast, M. W. 1997, *ApJ*, 485, 328
- Leão, I. C., de Laverny, P., Mékarnia, D., de Medeiros, J. R., & Vandame, B. 2006, *A&A*, 455, 187
- Le Bertre, T. 1992, *A&AS*, 94, 377
- Le Bertre, T. 1993, *A&AS*, 97, 729
- Le Bouquin, J.-B., Lacour, S., Renard, S., et al. 2009, *A&A*, 496, L1
- Lebzelter, T., Seifahrt, A., Uttenthaler, S., et al. 2012, *A&A*, 539, A109
- Leinert, C., Graser, U., Przygodda, F., et al. 2003, *Ap&SS*, 286, 73
- Leinert, C., van Boekel, R., Waters, L. B. F. M., et al. 2004, *A&A*, 423, 537
- Lopez, B., Wolf, S., Lagarde, S., et al. 2006, in *Proc. SPIE*, Vol. 6268, *Society of Photo-Optical Instrumentation Engineers (SPIE) Conference Series*, 62680Z
- Loup, C., Forveille, T., Omont, A., & Paul, J. F. 1993, *A&AS*, 99, 291
- Lykou, F., Klotz, D., Paladini, C., et al. 2015, *A&A*, 576, A46
- Maercker, M., Mohamed, S., Vlemmings, W. H. T., et al. 2012, *Nature*, 490, 232
- Maercker, M., Olofsson, H., Eriksson, K., Gustafsson, B., & Schöier, F. L. 2010, *A&A*, 511, A37
- Makarov, V. V. & Kaplan, G. H. 2005, *AJ*, 129, 2420
- Mauron, N. & Huggins, P. J. 2006, *A&A*, 452, 257
- Mayer, A., Jorissen, A., Kerschbaum, F., et al. 2011, *A&A*, 531, L4
- Mayer, A., Jorissen, A., Kerschbaum, F., et al. 2013, *A&A*, 549, A69
- Mayer, A., Jorissen, A., Paladini, C., et al. 2014, *A&A*, 570, A113
- McDonald, I., Zijlstra, A. A., & Boyer, M. L. 2012, *MNRAS*, 427, 343
- Mennesson, B., Perrin, G., Chagnon, G., et al. 2002, *ApJ*, 579, 446
- Mečina, M., Kerschbaum, F., Groenewegen, M. A. T., et al. 2014, *A&A*, 566, A69
- Meyer, C., Rabbia, Y., Froeschle, M., Helmer, G., & Amieux, G. 1995, *A&AS*, 110, 107
- Monnier, J. D., Geballe, T. R., & Danchi, W. C. 1998, *ApJ*, 502, 833
- Monnier, J. D., Geballe, T. R., & Danchi, W. C. 1999, *ApJ*, 521, 261
- Monnier, J. D., Millan-Gabet, R., Tuthill, P. G., et al. 2004, *ApJ*, 605, 436
- Norris, B. R. M., Tuthill, P. G., Ireland, M. J., et al. 2012, *Nature*, 484, 220
- Ohnaka, K., Bergeat, J., Driebe, T., et al. 2005, *A&A*, 429, 1057
- Ohnaka, K., Driebe, T., Hofmann, K.-H., Weigelt, G., & Wittkowski, M. 2008a, *A&A*, 484, 371
- Ohnaka, K., Driebe, T., Weigelt, G., & Wittkowski, M. 2007, *A&A*, 466, 1099
- Ohnaka, K., Izumiura, H., Leinert, C., et al. 2008b, *A&A*, 490, 173
- Olofsson, H., Bergman, P., Eriksson, K., & Gustafsson, B. 1996, *A&A*, 311, 587
- Olofsson, H., Bergman, P., Lucas, R., et al. 2000, *A&A*, 353, 583
- Olofsson, H., Carlstrom, U., Eriksson, K., & Gustafsson, B. 1992, *A&A*, 253, L17
- Olofsson, H., González Delgado, D., Kerschbaum, F., & Schöier, F. L. 2002a, *A&A*, 391, 1053
- Olofsson, H., González Delgado, D., Kerschbaum, F., & Schöier, F. L. 2002b, *A&A*, 391, 1053
- Paladini, C., Aringer, B., Hron, J., et al. 2009, *A&A*, 501, 1073
- Paladini, C., Sacuto, S., Klotz, D., et al. 2012, *A&A*, 544, L5
- Perrin, G., Coudé du Foresto, V., Ridgway, S. T., et al. 1999, *A&A*, 345, 221
- Pluzhnik, E. A., Ragland, S., LeCoroller, H., et al. 2009, *ApJ*, 700, 114
- Pojmanski, G. 2002, *Acta Astron.*, 52, 397
- Ragland, S., Traub, W. A., Berger, J.-P., et al. 2006, *ApJ*, 652, 650
- Ramstedt, S., Mohamed, S., Vlemmings, W. H. T., et al. 2014, *ArXiv e-prints*
- Ratzka, T. 2005, PhD thesis, Max-Planck-Institute for Astronomy, Königstuhl 17, 69117 Heidelberg, Germany
- Rau, G., Hron, J., Paladini, C., et al. 2017, in press, *A&A*
- Rau, G., Paladini, C., Hron, J., et al. 2015, *A&A*, 583, A106
- Richards, A. M. S., Elitzur, M., & Yates, J. A. 2011, *A&A*, 525, A56
- Richichi, A., Chandrasekhar, T., Lisi, F., et al. 1995, *A&A*, 301, 439
- Richichi, A., Percheron, I., & Kristoforova, M. 2005, *A&A*, 431, 773
- Sacuto, S., Aringer, B., Hron, J., et al. 2011, *A&A*, 525, A42
- Sacuto, S., Jorissen, A., Cruzalèbes, P., et al. 2008, *A&A*, 482, 561
- Sacuto, S., Ramstedt, S., Höfner, S., et al. 2013, *A&A*, 551, A72
- Sahai, R. 1992, *A&A*, 253, L33
- Samus, N. N., Durevich, O. V., & et al. 2009, *VizieR Online Data Catalog*, 1, 2025
- Schuller, P., Salomé, P., Perrin, G., et al. 2004, *A&A*, 418, 151
- Sloan, G. C., Little-Marenin, I. R., & Price, S. D. 1998, *AJ*, 115, 809
- Tabur, V., Bedding, T. R., Kiss, L. L., et al. 2009, *MNRAS*, 400, 1945
- Tatebe, K., Chandler, A. A., Hale, D. D. S., & Townes, C. H. 2006, *ApJ*, 652, 666
- Tatebe, K., Wishnow, E. H., Ryan, C. S., et al. 2008, *ApJ*, 689, 1289
- Tevoujan, S., Abdeli, K.-S., Weiner, J., Hale, D. D. S., & Townes, C. H. 2004, *ApJ*, 611, 466
- Teyssier, D., Hernandez, R., Bujarrabal, V., Yoshida, H., & Phillips, T. G. 2006, *A&A*, 450, 167
- Tristram, K. R. W., Burtscher, L., Jaffe, W., et al. 2014, *A&A*, 563, A82
- Tuthill, P. G., Monnier, J. D., Danchi, W. C., & Lopez, B. 2000, *ApJ*, 543, 284
- Valiante, R., Schneider, R., Bianchi, S., & Andersen, A. C. 2009, *MNRAS*, 397, 1661
- van Belle, G. T., Dyck, H. M., Thompson, R. R., Benson, J. A., & Kannappan, S. J. 1997, *AJ*, 114, 2150
- van Belle, G. T., Lane, B. F., Thompson, R. R., et al. 1999, *AJ*, 117, 521
- van Belle, G. T., Paladini, C., Aringer, B., Hron, J., & Ciardi, D. 2013, *ApJ*, 775, 45
- van Boekel, R., Min, M., Leinert, C., et al. 2004, *Nature*, 432, 479
- van der Veen, W. E. C. J. & Habing, H. J. 1988, *A&A*, 194, 125
- Van Eck, S., Jorissen, A., Udry, S., et al. 2000, *A&AS*, 145, 51

van Leeuwen, F. 2007, A&A, 474, 653

Weigelt, G., Balega, Y., Bloecker, T., et al. 1998, A&A, 333, L51

Weigelt, G., Balega, Y. Y., Blöcker, T., et al. 2002, A&A, 392, 131

Whitelock, P. & Feast, M. 2000, MNRAS, 319, 759

Whitelock, P. A., Feast, M. W., Marang, F., & Groenewegen, M. A. T. 2006, MNRAS, 369, 751

Wiesemeyer, H., Thum, C., Baudry, A., & Herpin, F. 2009, A&A, 498, 801

Winters, J. M., Le Bertre, T., Jeong, K. S., Nyman, L.-Å., & Epchtein, N. 2003, A&A, 409, 715

Wittkowski, M., Boboltz, D. A., Ireland, M., et al. 2011, A&A, 532, L7

Wittkowski, M., Boboltz, D. A., Ohnaka, K., Driebe, T., & Scholz, M. 2007, A&A, 470, 191

Woitke, P. 2006, A&A, 460, L9

Woodruff, H. C., Ireland, M. J., Tuthill, P. G., et al. 2009, ApJ, 691, 1328

Woodruff, H. C., Tuthill, P. G., Monnier, J. D., et al. 2008, ApJ, 673, 418

Zhao-Geisler, R., Quirrenbach, A., Köhler, R., & Lopez, B. 2012, A&A, 545, A56

Zhao-Geisler, R., Quirrenbach, A., Köhler, R., Lopez, B., & Leinert, C. 2011, A&A, 530, A120

Appendix A: MIDI results on individual stars

Appendix A.1: θ Aps

θ Aps is a semi-regular variable star located at a distance of 113 pc (van Leeuwen 2007). In its ISO spectrum the star shows silicate emission that is typical for an oxygen-rich AGB star (e.g. Fabian et al. 2001) with features at 10, 13, 19.5, and $32\mu\text{m}$. The mass-loss rate of the star was determined to be $0.4 \times 10^{-7} \text{ M}_{\odot} \text{ yr}^{-1}$ by Olofsson et al. (2002b). The Herschel image is of fermata-type with indications for a companion (Cox et al. 2012). Mayer et al. (2013) find indications for a jet that is interfering with the wind-ISM bow shock.

θ Aps was observed in 2011 and 2012. Six out of seven data sets are of good quality. There are no archive data.

Appendix A.1.1: Variability

The variability period for θ Aps is given as $P=119$ d (Samus et al. 2009). We calculated visual phases of the observations adopting phase-zero point $T_0 = 2\,454\,622$ JD.

The MIDI spectra have similar visual phases. Thus, a check for intra-cycle variability is not possible. However, a check for cycle-to-cycle spectroscopic variations can be performed by comparing the MIDI with ISO and IRAS data (Fig. 6). The flux level of the ISO and MIDI spectra is the same at least in the range $\sim 9.8 - 12.5 \mu\text{m}$, i.e. no spectroscopic cycle-to-cycle variations are found. However, below $\sim 9.8 \mu\text{m}$, a clear change in flux level is observed.

To check for interferometric variability, a set with similar baseline lengths and position angles observed at different visual phases is shown in Fig. A.1. No interferometric variability is detected.

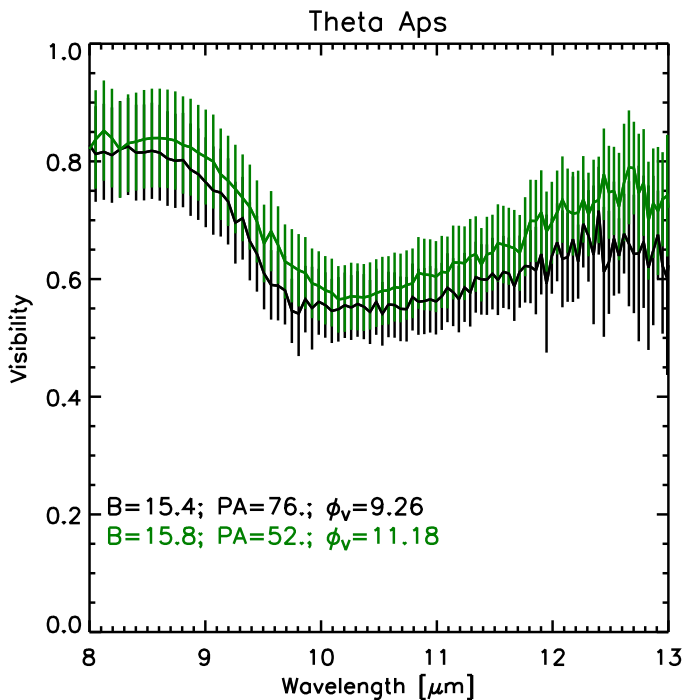


Fig. A.1. Interferometric variability check for θ Aps. B is the projected baseline, PA is the position angle, and ϕ_v is the visual phase.

Appendix A.1.2: Morphology

Calibrated visibilities are shown in Fig. A.2. No differential phase signature is detected, i.e. no asymmetries are observed in the brightness distribution.

The χ^2_{red} of the GEM-FIND fitting for the different models are given in Table 3. The increase of the UD diameter from $8 - 10 \mu\text{m}$ is pronounced for θ Aps, indicating that the star shows a strong silicate feature. This is in agreement with the ISO spectrum. The difference between the K -band (18.1 mas, Dumm & Schild 1998) and N -band diameter ($\sim 40 - 90$ mas) is evidence for dusty material in the circumstellar surrounding of the star. As θ Aps has a low mass-loss rate, the circumstellar environment can be assumed to be optically thin, therefore one cannot exclude that observations at larger baselines would point to a two-component structure of the CSE of θ Aps, as is the case for RT Vir and R Crt.

Appendix A.2: R Crt

R Crt is a semi-regular variable star. Its distance is given as 261 pc (van Leeuwen 2007). The star was part of many maser and CO-line studies. The CO-envelope seems to be consistent with a uniformly expanding envelope (Kahane & Jura 1994). The Herschel image was interpreted to be of ‘eye’-shape (Cox et al. 2012). This shape, however, is not well constrained (A. Mayer, private communication). The strength of the silicate feature is quite large (Begemann et al. 1997). R Crt also has a higher mass-loss rate ($8 \times 10^{-7} \text{ M}_{\odot} \text{ yr}^{-1}$) than the other O-rich sources.

R Crt was observed in 2009, 2011, and 2012, and 8 out of 12 data sets are of good quality.

Appendix A.2.1: Variability

The variability period of R Crt is given as $P = 160$ d (Samus et al. 2009). We calculated the visual phase of our observations assuming a phase-zero point $T_0 = 2\,454\,225$ JD. The observations were carried out at different visual phases within different cycles. This makes a check for cycle-to-cycle and intra-cycle variability necessary.

Possible variability effects can be checked in Fig. A.3, which gives the visual phase versus flux at 8, 10, and $12 \mu\text{m}$. Fluxes agree within the errors for 8 and $10 \mu\text{m}$. At $12 \mu\text{m}$ there seems to be a variation in the flux level when comparing MIDI and IRAS.

No sets with similar baseline lengths and position angles observed at different epochs are available. Therefore, no statement can be made concerning the interferometric variability.

Appendix A.2.2: Morphology

Calibrated visibilities are shown in Fig. A.4; the differential phase is always zero.

As for θ Aps, the strong silicate feature can be seen in the visibility profile at $\sim 9.8 \mu\text{m}$ for short baselines. On the other hand, for R Crt we also have at our disposal long baseline observations. The shape of the visibility for the longer baselines may still show some silicate feature, but much less pronounced than for the short features. Contributions from other molecular and dust species may shape the visibility profile (e.g. SiO, H₂O, and Al₂O₃).

The LP observations of R Crt are best described by an elliptical Gaussian profile with an axis ratio of 0.7 and an inclination angle of $\phi_{\text{incl}} = 157^\circ$.

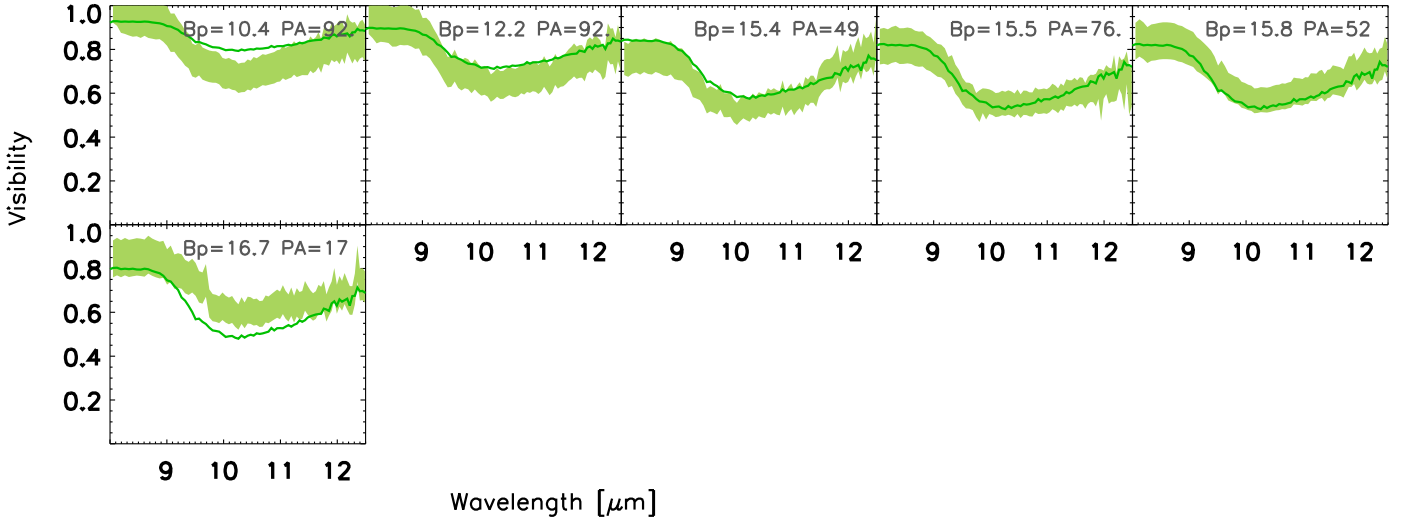


Fig. A.2. Best-fitting GEM-FIND model (solid line) for the MIDI visibilities of θ Aps.

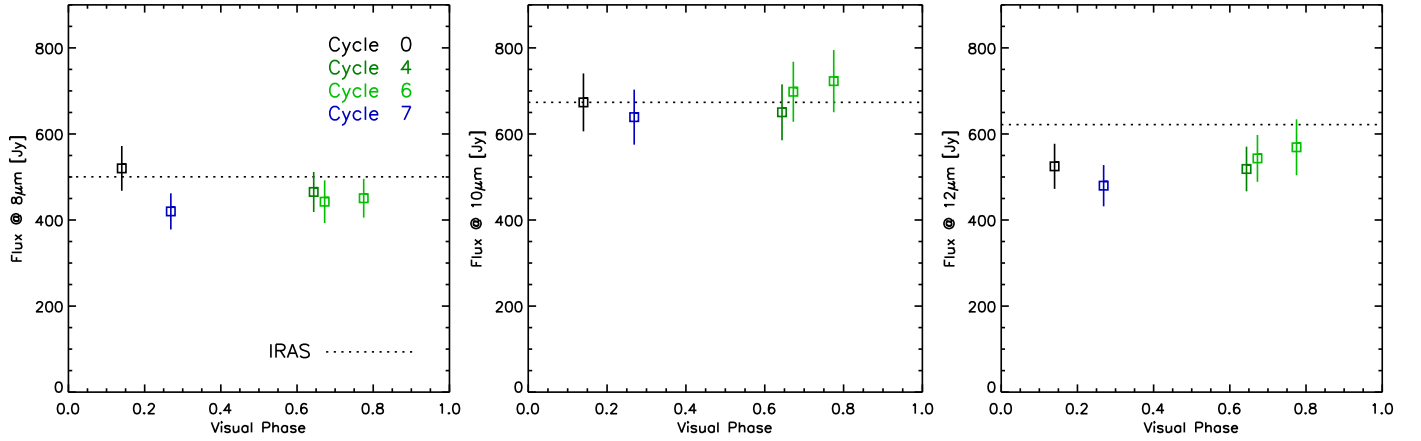


Fig. A.3. MIDI fluxes at 8, 10, and 12 μm observed for R Crt at various visual phases. These fluxes are compared with the IRAS flux.

As can be seen in the second row of Table 3, all one-component models fail to fit the observations of the LP combined with the archive data. The best-fitting model is a two-component model (CircUD+CircGauss; Fig. A.4). This suggests that the environment of R Crt is optically thin, where the outer environment is dominated by silicate-rich dust.

Appendix A.3: R Leo

R Leo is a well-studied O-rich AGB star of Mira type. Its distance is 110 pc (van Leeuwen 2007). Its magnitude in the V band ranges from 11.3 to 4.4 (Kholopov et al. 1998). Knapp et al. (1998) determined a mass-loss rate of $9.4 \times 10^{-8} M_{\odot} \text{ yr}^{-1}$. The Herschel image suggests that R Leo is of ‘fermata’ type (Cox et al. 2012).

Asymmetries. Evidence for asymmetries were found by Ireland et al. (2004b) and Burns et al. (1998) from the closure phases obtained with optical interferometry (650–1000 nm). Non-zero closure phases are also reported in the mid-infrared by Tatebe et al. (2008). They suggest that the closure phase signal of the star comes from an asymmetry that is located in the southern hemisphere of the star. Wiesemeyer et al. (2009) claim that

they detect a planet at a separation of 24 mas in their SiO maser data. They do not mention whether such a planet could be responsible for the closure phase signals observed in the other wavelength ranges. Perrin et al. (1999) used near-infrared interferometry and show that their observations at low spatial frequency ($< 40 \text{ arcsec}^{-1}$) are well represented by a UD model. On the other hand, data at high spatial frequencies ($40\text{--}80 \text{ arcsec}^{-1}$) cannot be explained by a UD or Gaussian intensity distribution, which may point to the presence of one or more extra structures. This is confirmed by the observations of Mennesson et al. (2002). Perrin et al. (1999) mention that the low spatial frequency observations within the first null cannot resolve small structures such as spots and this may be the reason why a UD model fits those data well. Monnier et al. (2004), however, report that both the low and high frequency data ($1\text{--}50 \text{ arcsec}^{-1}$) in the near-infrared can be perfectly fitted with a UD model. This may depend on the visual phase and is further discussed below under the heading Visual phase-dependent diameter. The CO line profile of R Leo shows an asymmetric shape with the red side being stronger (Knapp et al. 1998; Teyssier et al. 2006).

Ellipticity. Reports of an elliptical shape of the CSE of R Leo are reported in the optical (Lattanzi et al. 1997) and in the

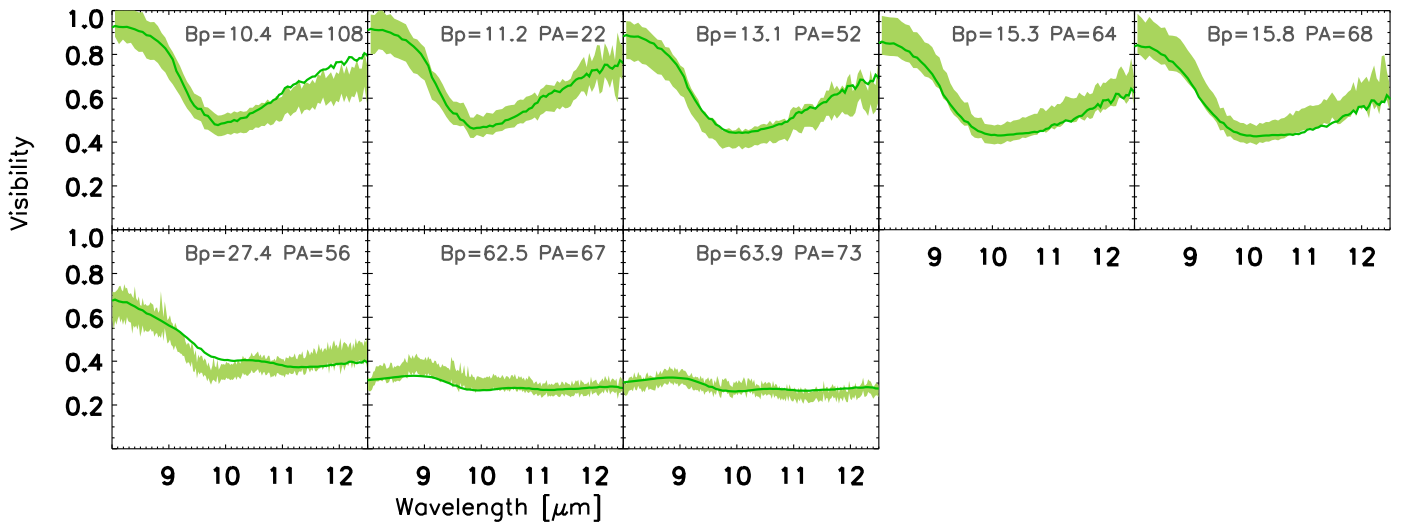


Fig. A.4. Best-fitting GEM-FIND model (solid line) for the MIDI visibilities of R Crb.

mid-infrared (Tatebe et al. 2008). On the other hand, several other studies do not find any signs of ellipticity (e.g. Burns et al. 1998; Monnier et al. 2004).

Wavelength-dependent diameter. A dependence of the diameter on wavelength is reported in the optical by Hofmann et al. (2001), where the size is twice as large in the TiO band-head as in the continuum. A size increase from the *K* band to the *L* band of 20–30% was reported by Mennesson et al. (2002) and Schuller et al. (2004). The multiwavelength study of Woodruff et al. (2009) in the near-infrared showed that there is a clear anti-correlation between the angular diameter and the features seen in the spectrum.

Visual phase-dependent diameter. Chagnon et al. (2002) interferometrically observed the star in the near-IR at two different visual phases and find that one set can be modelled with a UD, the other not. This is confirmed by Fedele et al. (2005) who find that their pre-maximum data can be explained by a UD, however, the post-maximum data cannot. Such a variability in the size of R Leo is detected by several authors in the near-IR (Perrin et al. 1999; Chagnon et al. 2002; Mennesson et al. 2002; Fedele et al. 2005; Woodruff et al. 2008, 2009), with the star being largest at visual minimum as already predicted by pulsation models; none of these models, however, can reproduce the pulsation amplitude of R Leo (Ireland et al. 2004a). Such variability was also detected in the optical (Burns et al. 1998) and mid-infrared (Tatebe et al. 2006, 2008). Mennesson et al. (2002) mention that such changes may be caused by variations in the spatial extent and/or in the opacity of the outer atmospheric layers.

R Leo was observed in 2006, 2007, and 2012. Out of 26 data sets, 17 are of good quality.

Appendix A.3.1: Variability

The variability period of R Leo is $P = 310$ d (Whitelock & Feast 2000) and we adopted phase-zero point $T_0 = 2453\,540$ JD to calculate the corresponding visual phase. The observations were carried out at different visual phases within different cycles. This makes a check for cycle-to-cycle and intra-cycle variability possible.

The variation of the flux with visual phase was detected in the mid-infrared by Monnier et al. (1999) and Tatebe et al. (2006), where the flux is 30% lower at visual minimum. We confirm the trend of lower fluxes towards the minimum in Fig. A.5, which shows visual phase versus flux at 8, 10, and $12\,\mu\text{m}$.

The interferometric observations with similar baselines and position angle shown in green in the left panel of Fig. A.6 are taken at very similar visual phase, therefore it does not come as a surprise that no intra-cycle variability is detected. A third observation (black line in the left panel of Fig. A.6) is taken six cycles apart. Even in this case no cycle-to-cycle interferometric variability is observed. Changes in the visibility with visual phase are shown in the right panel, Fig. A.6. The black line here is the result of the average of two observations taken at the same baseline and position angle, and one day apart. The variability in the visibility is accompanied with a non-zero differential phase. Such variations were found in the mid-infrared by Tatebe et al. (2006) and Tatebe et al. (2008). This may be an indication that for R Leo observations at different visual phase should not be combined.

Appendix A.3.2: Morphology

Calibrated visibilities are shown in Fig. A.7.

The χ^2_{red} of the GEM-FIND fitting for the LP data is given in the first row of Table 3. The morphology of R Leo seems to be very complex. When performing a GEM-FIND fit on the whole LP data sets, the best model is a UD. However, combining the LP and archive data, none of the GEM-FIND models were able to provide a good fit (confirmed by the high value of χ^2_{red} for the best-fitting model). One explanation could be that the environment of R Leo is made of more than two components, i.e. multiple shells are observed with MIDI. Another possible explanation could be variability in the *N* band, which was already reported by Tatebe et al. (2006) and Tatebe et al. (2008) and confirmed in this work. Therefore, considering that there may be intra-cycle variability, we combined all data at similar visual phases to do the fitting. Also in this case the UD model does not provide a good fit to the data. As all the observations in the archive were observed at approximately the same position angle, they do not provide supplementary constraints to fit more complex asymmetric models.

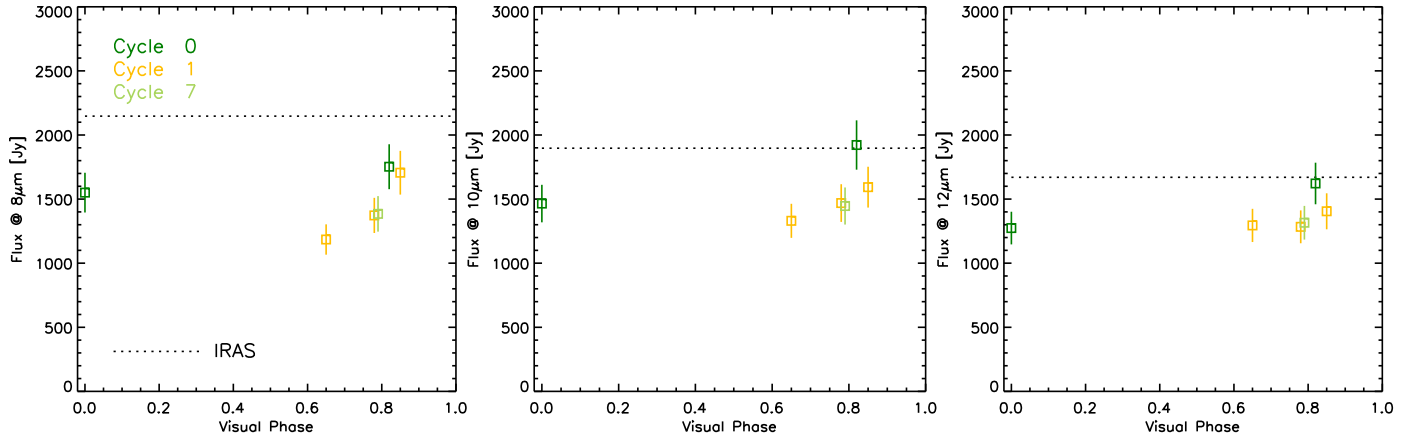


Fig. A.5. Visual phase vs MIDI flux at 8, 10, and 12 μm for R Leo.

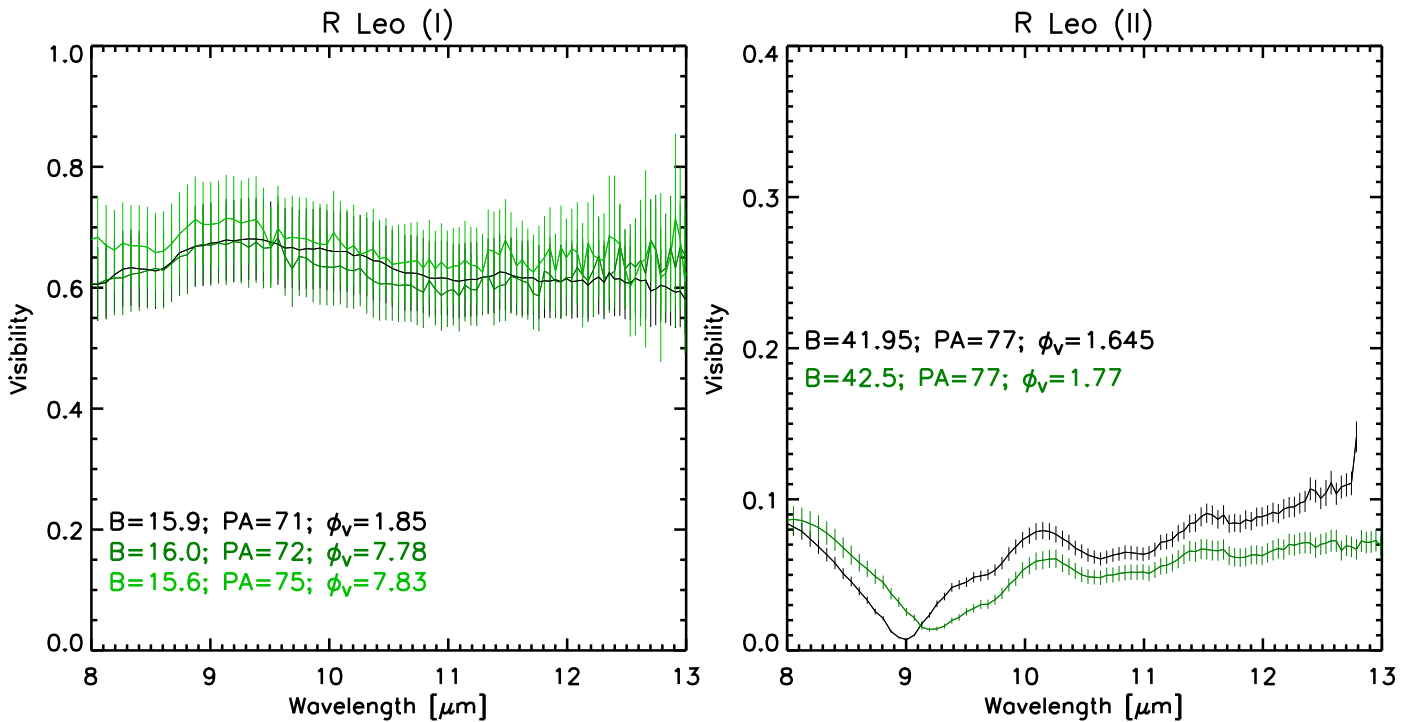


Fig. A.6. Interferometric variability check for R Leo. The black line shown in the right panel is the result of the average of two observations. The latter were observed one day apart with similar projected baseline and PA.

There is a differential phase signature present for observations with baselines ~ 40 and ~ 60 m (Fig. 4).

Appendix A.4: T Mic

T Mic is a semi-regular variable star located at a distance of 200 pc (Loup et al. 1993). This star was part of different photometric, spectroscopic, and CO-line-profile studies. Its mass-loss rate is estimated to be $8 \times 10^{-8} M_{\odot} \text{ yr}^{-1}$ (Olofsson et al. 2002b). The Herschel image is interpreted as of ‘fermata’-type (Cox et al. 2012), i.e. shows signs of interaction with the ISM. T Mic was observed in 2004, 2010, and 2011. Out of 10 data sets, 7 are of good quality.

Appendix A.4.1: Variability

We derived visual phases for the observations, however the values need to be considered with caution. In fact light curves available from AAVSO, ASAS, DIRBE, and HIPPARCOS do not cover the epoch of the ISO or MIDI data. The adopted origin for the visual phase determination is $T_0 = 2\,452\,832$ JD. The observations were carried out at different visual phases within different cycles. The two spectra obtained on 2004 July 30 and 31 were averaged. The flux level of the ISO and MIDI spectra in Fig. 6 is not the same, i.e. the level of N -band emission may have changed. No data set with similar baseline lengths and position angles observed at different epochs is available. Therefore, no statement can be made on the interferometric variability.

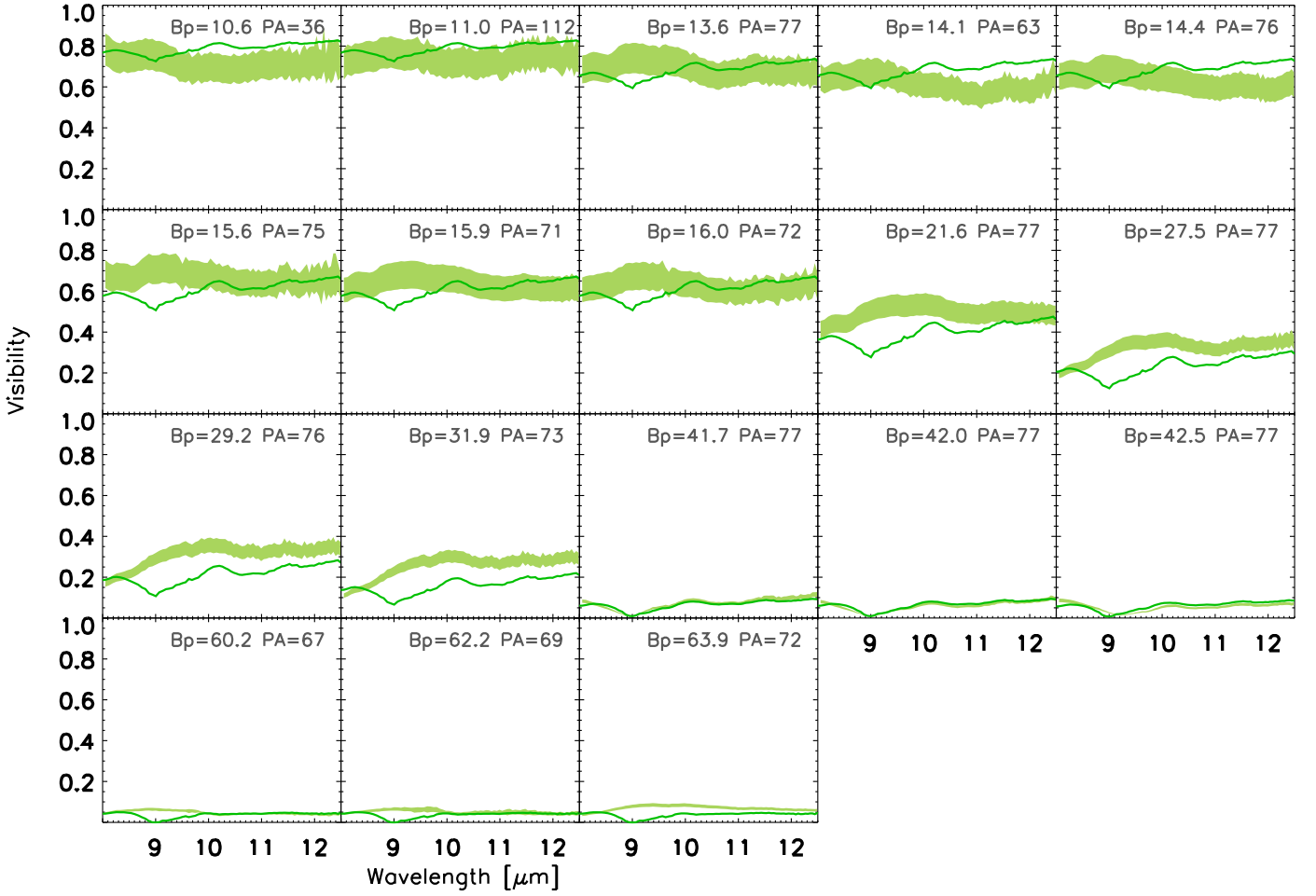


Fig. A.7. Best-fitting GEM-FIND model (solid line) for the MIDI visibilities of R Leo.

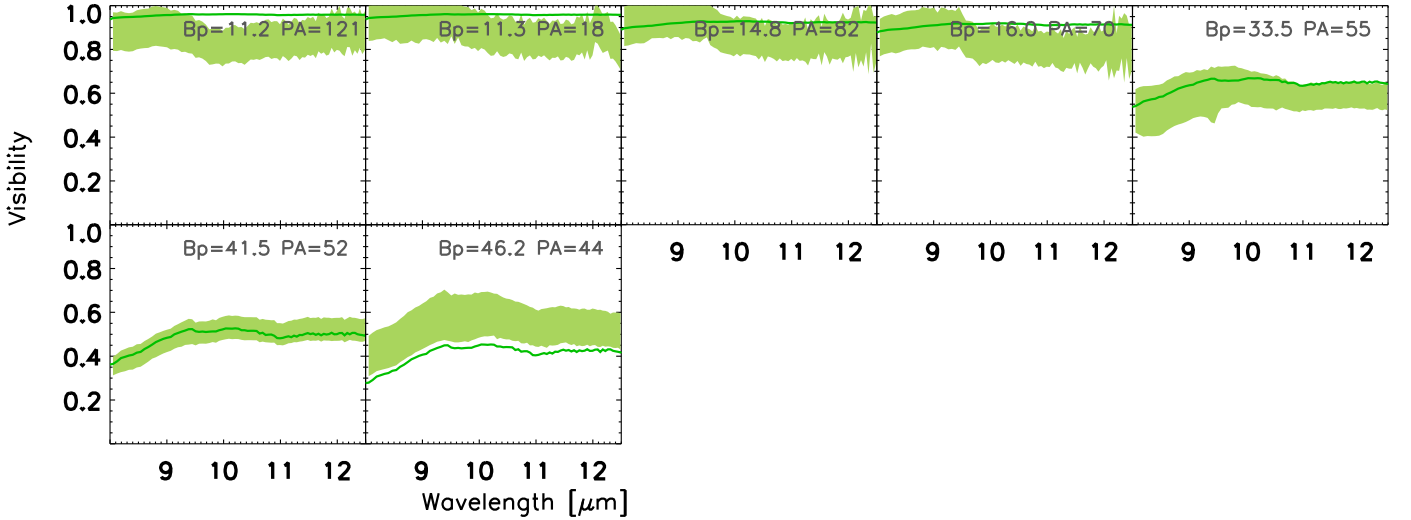


Fig. A.8. Best-fitting GEM-FIND model for the MIDI visibilities of T Mic.

Appendix A.4.2: Morphology

Calibrated visibilities are shown in Fig. A.8.

T Mic does not show a strong silicate feature. However, the slight drop that is observed in the visibility of baselines shorter than 16 m at $\sim 9.8 \mu\text{m}$ can be attributed to silicate dust. No differ-

ential phase signature is detected in T Mic, i.e. no asymmetries are detected with MIDI.

The fitting of the LP data of 2011 with GEM-FIND reveals that T Mic can be well described with a circular UD model. The

χ^2_{red} of the GEM-FIND fitting for the different models is given in the first row in Table 3.

If the LP data are combined with the archive data, the best-fitting model is a circular Gaussian model. The fit, however, does not describe the short baseline and 46 m baseline data well. This could mean that the close environment of T Mic is more complex and cannot be described with a one-component or two-component geometric models. The other possibility is that the short-baseline data (observed in 2011) cannot be combined with the longer baseline data (2004 and 2010) because of a variability effect.

Appendix A.5: RT Vir

RT Vir is a semi-regular variable star that is located at a distance $d = 136$ pc (van Leeuwen 2007). RT Vir is a well-studied and, one of the brightest, water maser sources (Richards et al. 2011). Several mass-loss estimates are given, lying between $1.1 \times 10^{-7} M_{\odot} \text{ yr}^{-1}$ (Knapp et al. 1998) and $5 \times 10^{-7} M_{\odot} \text{ yr}^{-1}$ (Olofsson et al. 2002b). Sacuto et al. (2013) recently reported an asymmetry revealed through the MIDI differential phase at 9 stellar radii (12 AU), and also spectroscopic cycle-to-cycle variability. The Herschel image is interpreted as being of ‘fermata’ type (Cox et al. 2012).

RT Vir was observed in 2008, 2009, 2011, and 2012. For our programme, we obtained six data sets, but only two turned out to be of good quality. The archive data, on the other hand, are of good quality. Twelve out of 13 data sets can be used.

Appendix A.5.1: Variability

The visual phase of the MIDI observations is derived using the light curve from ASAS (Pojmanski 2002). The variability period for RT Vir is given as $P=375$ d (Imai et al. 1997) and the phase-zero point is $T_0 = 2454854$ JD (adopted from Sacuto et al. 2013). The observations were carried out at different visual phases within different cycles.

The flux level of the ISO and MIDI spectra is not the same, i.e. the level of N -band emission has changed. From Fig. A.9, one can see that the flux is lowest at visual minimum. At a glance, it also seems that the flux follows a sinusoid with maximum flux shifted from the visual maximum. This kind of behaviour was already predicted by model atmosphere simulations (Ireland et al. 2004a, for near-infrared wavelengths), and observed by Zhao-Geisler et al. (2012). Since these observations are carried at different cycles, the effect of cycle-to-cycle variation cannot be completely ruled out (Sacuto et al. 2013).

To check for interferometric variability, data sets with similar baseline lengths and position angles observed at different visual phases are shown in Fig. A.10. Although photometric variability is present, we do not report any interferometric variability, confirming the results of Sacuto et al. (2013). It would be interesting to monitor the atmosphere with long baselines to check whether interferometric variability can be detected at high spatial frequencies, where the object also presents an asymmetry (see following section). As no interferometric variability is so far observed, all data sets can be combined in the further analysis.

Appendix A.5.2: Morphology

Calibrated visibilities are shown in Fig. A.11. The drop that is observed in the visibility can be attributed to amorphous sili-

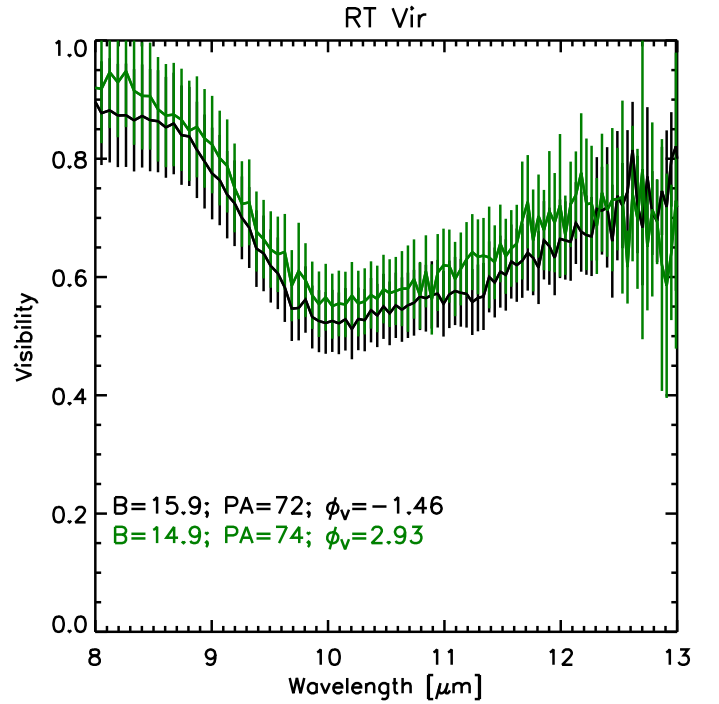


Fig. A.10. Interferometric variability check for RT Vir.

cate. For RT Vir, a non-zero differential phase is detected for the longest baselines (89 and 128 m) by Sacuto et al. (2013). This is the signature of an asymmetry. Sacuto et al. (2013) used GEM-FIND to fit different geometric models to a subset of the data. Not only one-component but also two- and three-component models are used in their work. The best-fitting model is a three-component model: a UD that describes the central star, a spherical Gaussian that represents the optically thin dust environment, and a Dirac function that represents the unresolved asymmetry (which could be a companion or a dust clump). This model is also able to reproduce the observed differential phase.

Although Sacuto et al. (2013) find the environment of RT Vir to be asymmetric, we start by fitting spherically symmetric models to the LP data that do not show any asymmetry. The LP data can be fitted best with a circular Gaussian profile with a FWHM of ~ 60 mas at $10 \mu\text{m}$ (see first row in Table 3). As only two observations with the same position angle are available, no attempt to fit elliptical models was made. If we combine the LP data with the archive data, a one-component model is no longer able to describe the observations (see second row in Table 3). Therefore, we fit a spherical model, composed of a circular UD and a circular Gaussian, to the data. The best-fitting diameter of the circular UD is 16 mas. The diameter derived by Richichi et al. (2005) in the K band is $\theta_K=12.4$ mas. Our model does not fit the short-baseline data well enough. The model of Sacuto et al. (2013), on the other hand, fits all the visibility and differential phase observations (as the model is asymmetric). The diameter of their UD is wavelength dependent and larger than the K -band diameter determined by Richichi et al. (2005), which suggests that the environment is composed of more than one silicate-rich layer (Sacuto et al. 2013).

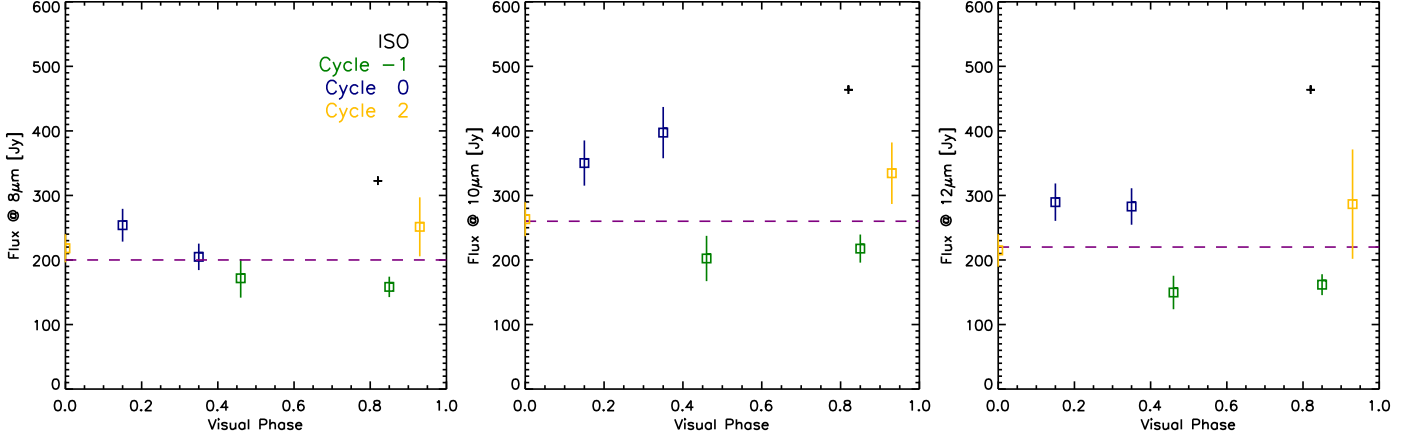


Fig. A.9. Visual phase vs. 8 (left), 10 (centre), and 12 μm (right) flux for RT Vir. The colours refer to the cycles, while the cross indicates the ISO flux. A cyan horizontal line was drawn to guide the eye and to make the sinusoidal-like variations clearer.

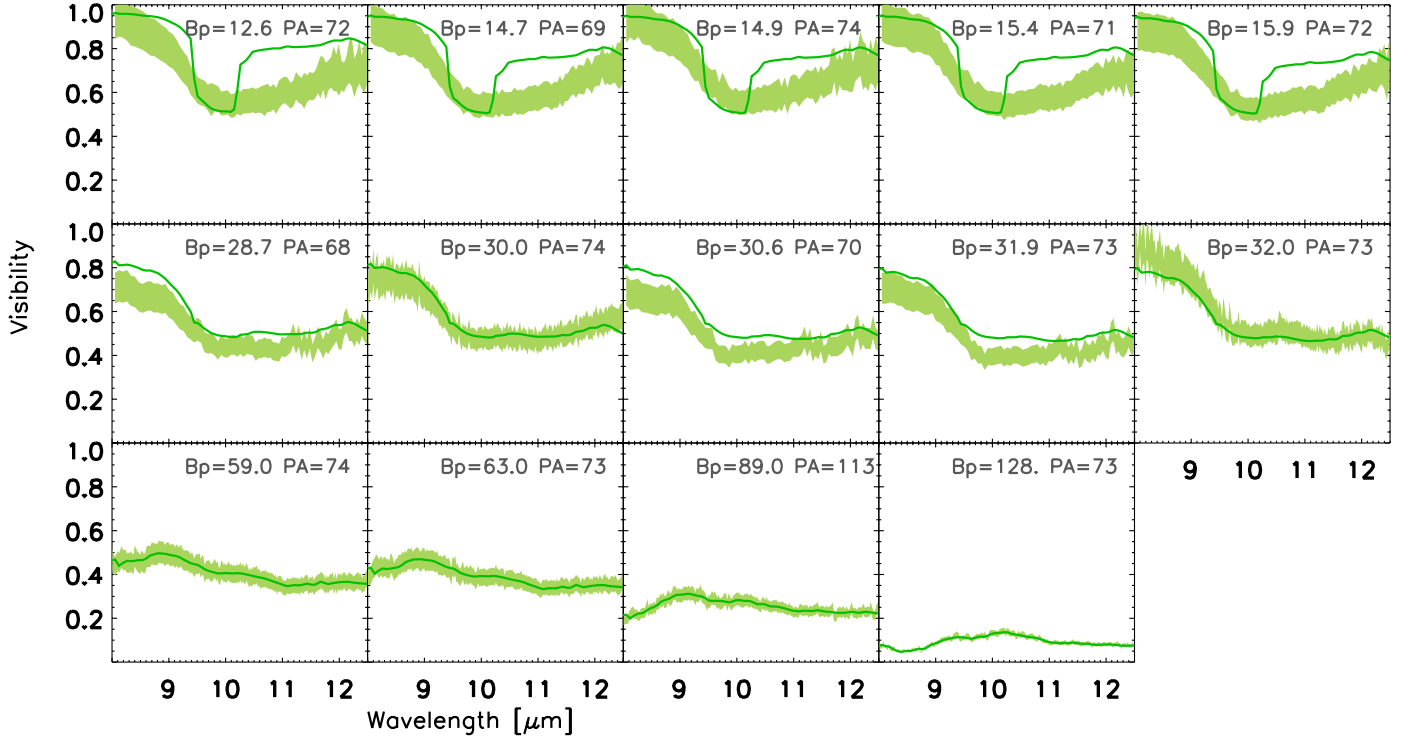


Fig. A.11. Best-fitting GEM-FIND model (solid line) for the MIDI visibilities of RT Vir.

Appendix A.6: π^1 Gru

π^1 Gru is a well-studied S-type star close to the tip of the AGB (Jorissen et al. 1993; Van Eck et al. 2000). The star is known to have a G0V companion located $\approx 2.7''$ (≈ 450 AU) away from the primary, and possibly a third component much closer as suggested by Makarov & Kaplan (2005); Frankowski et al. (2007) and more recently, Mayer et al. (2014). CO line observations (Sahai 1992; Knapp et al. 1999; Chiu et al. 2006) reveal an asymmetric, double-peaked structure and extended emission wings, which are interpreted as an expanding disk and a fast bipolar outflow oriented perpendicular to the disk. The Herschel/PACS image shows an elliptical emission and a hook east of the star at a distance of $38''$ (Fig. 5, Mayer et al. 2014). These kinds of hooks or arcs is most probably part of an Archimedean spiral

formed by the interaction with a companion (e.g. α Cen; Mayer et al. 2011). Therefore the presence of the companion(s) affects the geometry of the atmosphere at different spatial scales. The star was observed with MIDI in 2008 and 2011. We have a total of 11 data sets to fit, 4 of which are from the LP.

Appendix A.6.1: Variability

π^1 Gru is a SRb variable with period 198 d. However, as already stated in Sect. 2.2 of Sacuto et al. (2008), because of the semi-regular nature of the object, it is very difficult to assign a visual phase to a given observation. Sacuto et al. (2008) give two explanations for the discrepancy between the level of the ISO and the 2006 MIDI spectra: first, MIDI is missing some of the flux

that is seen by the larger ISO beam; and, second, there is a difference in the emission due to pulsation. The difference we observe between the 2011 LP data, ISO, and the 2006 data could be due to cycle-to-cycle variability.

Appendix A.6.2: Morphology

Concerning the shape of the visibility versus wavelength, we observe the typical shape of silicate dust with a bump between 8 and 9 μm . A drop is also observed in the visibilities at wavelengths longer than 12 μm . The lower left panel of Fig. A.12 shows a slightly different shape in the visibility with respect to the other panels. This may be a residual of a non-perfect calibration (Sacuto et al. 2008). A fit including only the LP data points to an elliptical UD morphology with axis ratio 0.2 and inclination 140°. The visibilities observed for π^1 Gru can be well fitted with a composite model UD+Gaussian, as shown in Fig. A.12.

Appendix A.7: *omi Ori*

omi Ori is one of the two S-type stars of our sample. According to the recent parameter determination by Cruzalèbes et al. (2013a), the star has a K -band angular diameter of 9.78 mas. Cruzalèbes et al. (2013b) reports asymmetric structures detected (via a closure-phase signature) in the near-infrared. The star is known to have a white dwarf companion (Ake & Johnson 1988), but the separation between the two stars, and more generally the orbit of the system, are not known. The star was classified among the irregular morphologies in the Herschel/PACS images (Cox et al. 2012). *omi Ori* was observed by MIDI in 2005 and 2011, and we collected a total of 14 data sets, 7 of which are archive data.

Appendix A.7.1: Variability

Classified as SRb, *omi Ori* has a period of 30 days. We collected a light curve from ASAS, but the data are limited to 2010, therefore we could not estimate the visual phase for the MIDI data of the LP. A comparison of the IRAS spectrum with the MIDI spectrum from 2005 shows no evidence of variability. The data of the LP were collected within a few days, therefore we do not need to worry about interferometric intra-cycle variability. As there is no overlap between the baselines and position angles of the archive data and those from the LP, it is not possible to issue any statement concerning cycle-to-cycle interferometric variability. As a consequence, one should consider the results from the χ^2_{red} combining all the data only as indicative.

Appendix A.7.2: Morphology

The visibility curve of *omi Ori* does not show any sign of dust when plotted versus wavelength. The feature observed around 9.58 μm is due to telluric ozone. The LP data sample the upper part of the visibility curve. Therefore a fit on these data cannot really distinguish between Gaussian and UD profiles. As a confirmation, the χ^2_{red} of the two models are very close to each other. GEM-FIND fits of the LP data point to an elliptical UD model with inclination 55° and axis ratio 0.4. The χ^2_{red} obtained by fitting all the data (archive+LP) points towards a composite model (UD+Gauss) with a very extended Gaussian (FWHM > 220 mas) enshrouding the UD (see also Fig. A.13). The flux ratio is > 50, meaning that the central source is the dominant contributor.

Appendix A.8: *U Ant*

U Ant is a nearby N-type carbon star. Knapp et al. (2003) reported a distance of 260 pc. Bergeat & Chevallier (2005) estimated its parameters as follows: $T_{\text{eff}} = 2810\text{K}$, the $C/O = 1.44$, $\dot{M} = 2.0 \times 10^{-6} M_{\odot} \text{ yr}^{-1}$. More recently, McDonald et al. (2012) estimated a much hotter temperature (3317 K) through spectral energy distribution (SED) fitting. Five spherical detached shells were detected at long wavelength and large scales $\sim 25'', 37'', 43'', 50'', 3'$ (Izumiura et al. 1996; Olofsson et al. 1996; González Delgado et al. 2001, 2003; Maercker et al. 2010). Herschel-PACS imaged in the FIR a shell with a distance from the star of 42'' (Kerschbaum et al. 2010).

The star was observed with MIDI in 2008 and 2012. For our programme, we obtained five observations, but only one of them turned out to be of any use. The reason for this is mostly poor seeing conditions during the nights of observation. Most of the archive data are also of mediocre quality. Only two points out of five from the archive is hereafter used.

Appendix A.8.1: Variability

Since *U Ant* is an irregular variable of type Lb, it is not possible to determine at which visual phase the observations were taken. Moreover, there are no V -band measurements available at the time of the MIDI observations. Therefore, a study of the interferometric variability is not possible for this star. We retrieved the IRAS spectrum from the archive and compared it with the MIDI spectrum in Fig. 6. The star is classified as SiC+ by Sloan et al. (1998). This class of objects is characterised by a spectrum with a weak 8.5-9 μm feature, a weak dust continuum, and a weak SiC feature that is observed in our spectra. The MIDI spectrum is within the error bars of the the IRAS spectrum.

Appendix A.8.2: Morphology

Three visibility points (Fig. A.14) are definitely too few to have an idea about the morphology of the star, especially if one considers that the data are taken four years apart. Therefore, for this star, we can only derive sizes and study the molecular and dust components. The diameter of the best-fitting FWHM varies between 7 and 10 mas as a function of wavelength.

Even though both MIDI and IRAS spectra exhibit a weak SiC feature, the visibilities are typical of the carbon stars without SiC (Fig. 3). Indeed the typical visibility drop around 11.3 μm is not observed here. A small decrease of the visibility is observed only for one of the observations with the 30 m baseline. On the other hand, the high level of visibility and, consequently, its large associated uncertainty, do not allow us to infer whether or not that decrease is real and due to SiC.

Appendix A.9: *R Lep*

R Lep is one of the closest carbon-rich Miras in the southern hemisphere showing intermediate mass-loss rates and very red colours (Whitelock et al. 2006, $J - K = 2.23$). van Belle et al. (1997) reported a K -band diameter of 11.50 mas, while Chagnon et al. (2002) measured 37.10 mas in the L' band. Signatures of asymmetric structures were observed by Ragland et al. (2006) with the IOTA interferometer in the near-IR. The object is classified as non-detection by Cox et al. (2012). Nevertheless, the authors predict the presence of a bow shock at a distance < 1 pc from the stellar envelope. The star was observed with MIDI in 2010, 2011, and 2012.

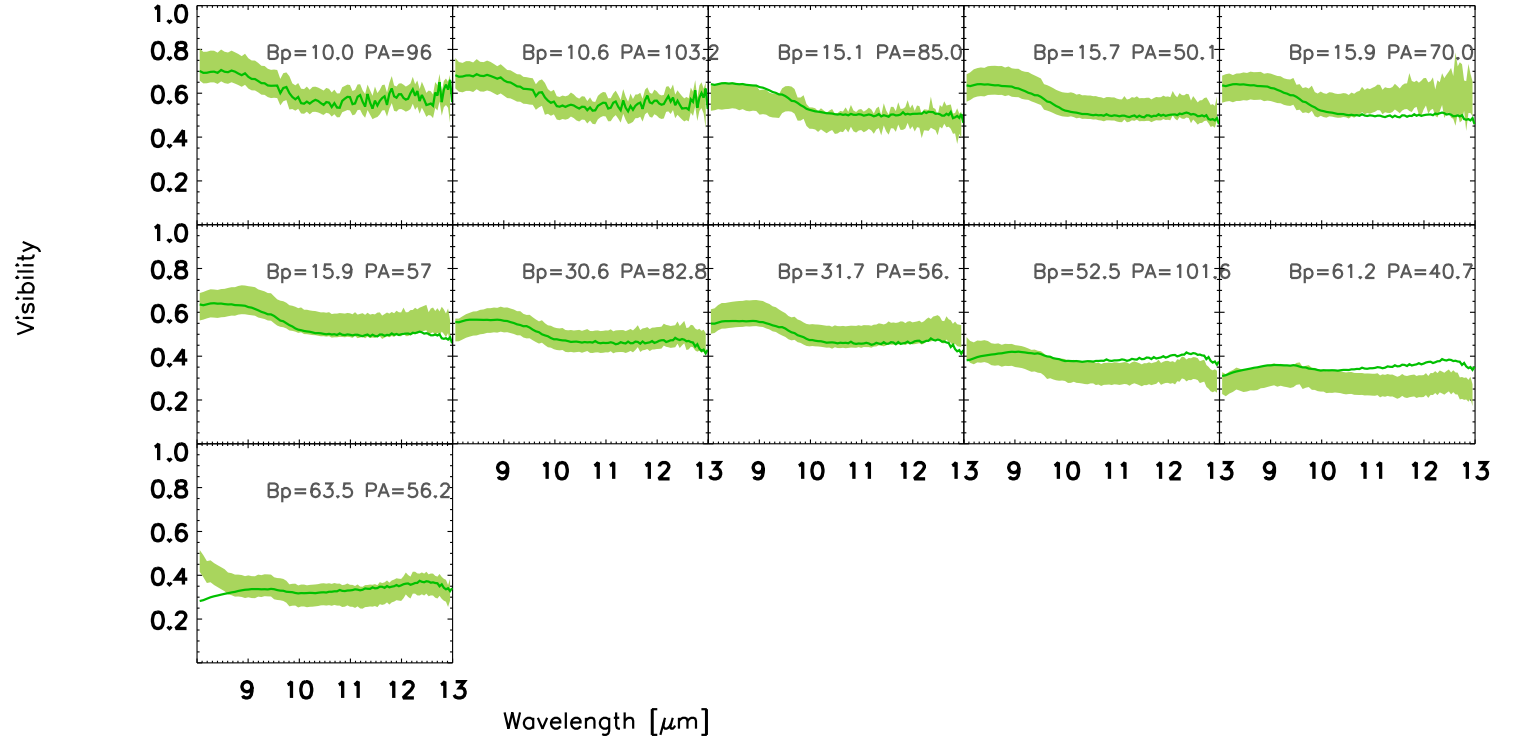


Fig. A.12. Best-fitting GEM-FIND model (solid line) for the MIDI visibilities of π^1 Gru.

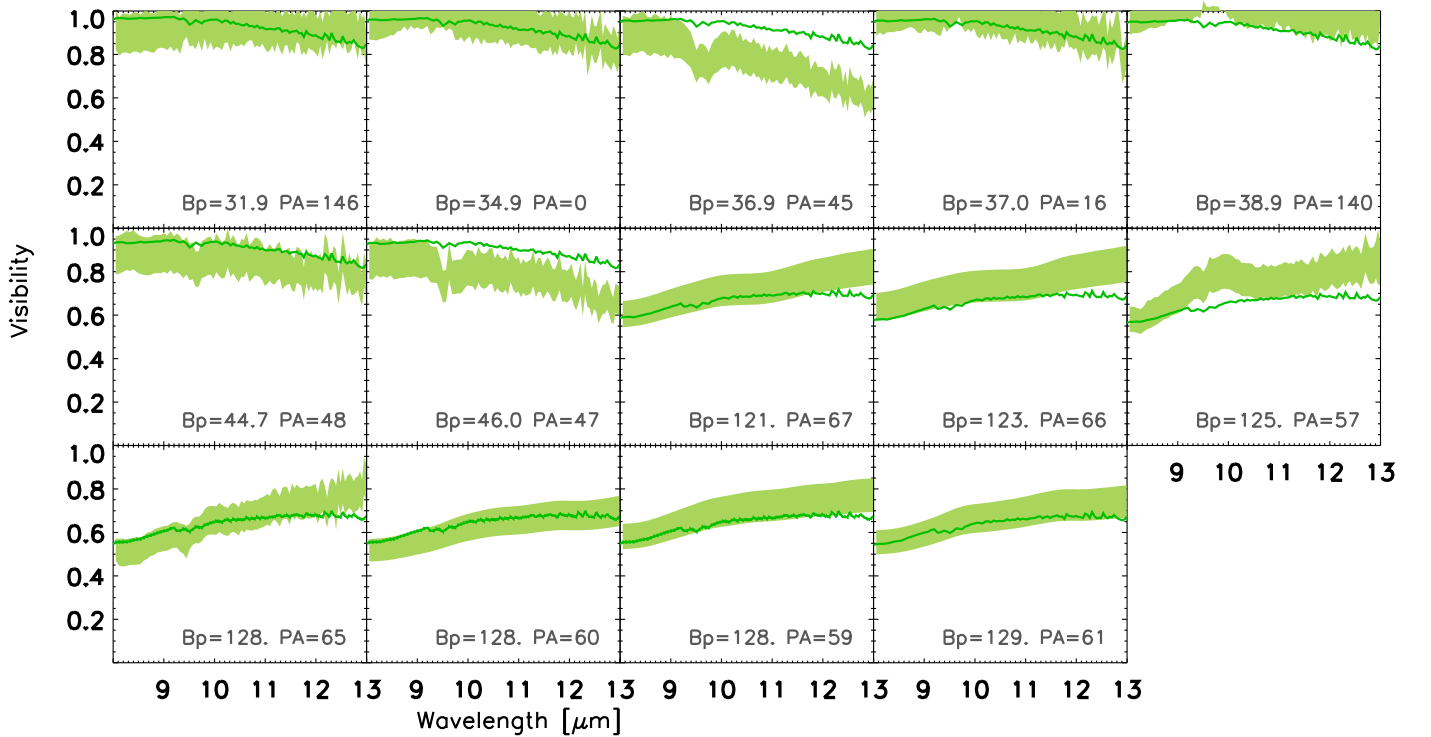


Fig. A.13. Best-fitting GEM-FIND model for the MIDI visibilities of omi Ori.

Appendix A.9.1: Variability

The MIDI spectra of R Lep, shown in Fig. 6, are very noisy. The flux also changes a lot within the MIDI data and between MIDI and IRAS. Excluding the data point from cycle 0 (yellow square in Fig. A.15), which has an unrealistic low flux, the

variations within the MIDI data are of the order of 0.2 magnitude. This is a reasonable value if compared with the variations⁴ $\Delta m_N < 0.48$ mag predicted by Le Bertre (1992). The flux varia-

⁴ Le Bertre (1992) observed a decrease in the amplitude of variability of Mira stars towards the long wavelengths. There are no N -band mea-

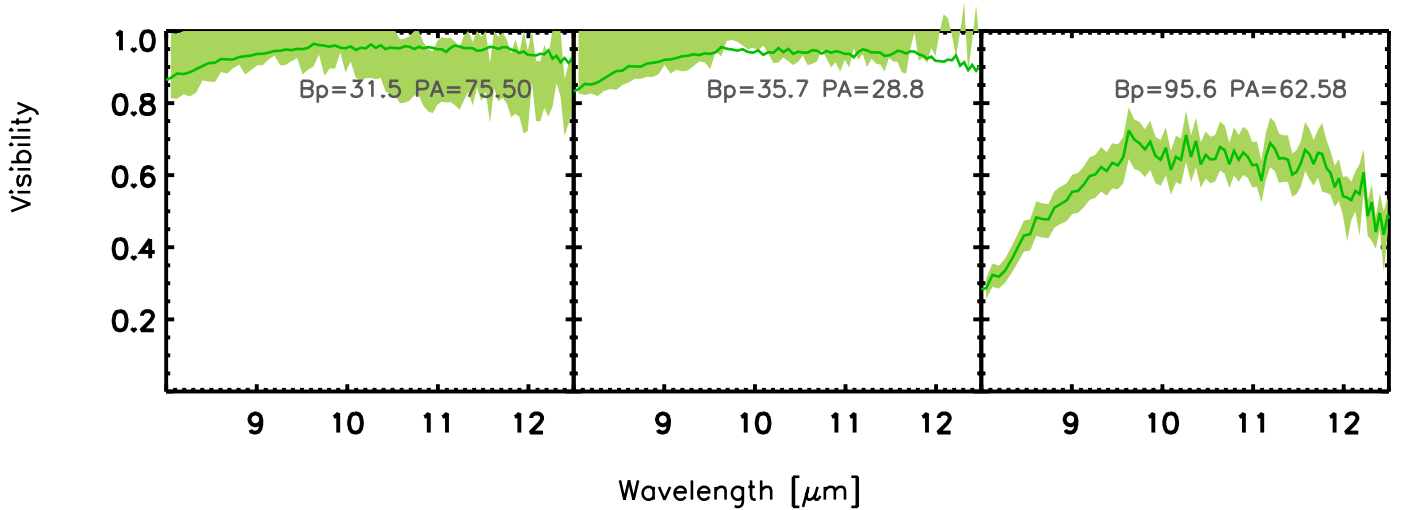


Fig. A.14. Best-fitting Gaussian profile (solid-line) for the MIDI visibilities of U Ant.

tion between the MIDI data from cycle 2 and the IRAS spectrum is of the order of 0.7 mag. Nevertheless, the MIDI spectra should be considered with caution. Regarding interferometric variability, the left panel of Fig. A.16 shows data sets that are too close in time to detect any intra-cycle variability. On the other hand, in the right panel of Fig. A.16 there is a hint for a cycle-to-cycle variability: the visibility from cycle 0 is systematically lower than the others in the range where molecular opacities are at play (8–10 μm). Since the variability effect is small, the data are still combined together for the GEM-FIND fit.

Appendix A.9.2: Morphology

The visibility curve of R Lep (Fig. A.17) is typical for a carbon Mira with a SiC feature, and it is described in Sect. 4. By using only the LP data, we obtain a better χ^2_{red} for the Gaussian model, whereas we have a good fit of the data with a two-component model by adding all the observations together (UD+Gaussian; see Fig. A.17). We do not observe any asymmetric structure that might be related to the asymmetries observed at other spatial scales and wavelengths (i.e. near-infrared by Ragland et al. 2006). The SiC depression is always present in the visibility curve, but we note that at long baselines and long wavelengths the visibility increases again. This might be explained by the fact that at those spatial frequencies, there is some extra molecular opacity appearing to make the object smaller. SiC is clearly present in the IRAS spectrum of the star, and since we are sampling the spatial frequencies at 2 stellar radii (using as a reference the photospheric diameter given by van Belle et al. 1997), we can say that SiC is already observed at 2 stellar radii.

Appendix A.10: Y Pav

Y Pav is a semi-regular C-rich variable with period 232 days and distance 400 pc (van Leeuwen 2007). The object is classified class X by Cox et al. (2012); no bow-shock nor detached shell were identified. Sloan et al. (1998) classified the spectrum of this object as Br1 (Broad 1). This class includes stars showing broad emission features extending from 8–9 μm to 12 μm , and

measurements reported for R Lep, but the variability in the *M* band is 0.48 mag, i.e. the variability in the *N* band must be smaller than this value.

the authors are not able to identify the opacities contributing to these extended features. It is observed that the Br1 stars have similar colour distribution as the SiC class, but the central object is cooler. According to the IRAS colour-colour diagram, this object is evolving towards a carbon Mira. Y Pav was observed only in the framework of our programme in 2011, and we used four out of seven observations for the modelling (*u, v*-coverage shown in Fig. 2). The data discarded suffered from poor weather conditions.

Appendix A.10.1: Variability

No interferometric variability can be assessed, as the data were taken at a single epoch. The difference between the IRAS and MIDI spectra is very likely due to calibration problems. They are not mentioned further.

Appendix A.10.2: Morphology

The visibility versus wavelength plotted in Fig. A.19 shows a minimum in the visibility curve slightly shifted towards shorter wavelength than the SiC feature. The difference is very small and can also be seen in Fig. A.18. It is not clear whether this difference is related to the Br1 spectral classification, mainly because this is the only Br1 of the sample. A detailed modelling of the visibilities and of the ISO spectrum by means of model atmospheres clarifies what kind of opacities are contributing most (Rau et al., prep.).

The visibility obtained are very high and can be well fitted by a Gaussian profile (Fig. A.19).

Appendix A.11: TX Psc

A detailed mid-infrared spectro-interferometric study of TX Psc can be found in Klotz et al. (2013). In this section, we present the new visibility data from the LP and discuss the morphology of the source. As the spectral type of the calibrators used for the LP data are M1 and M3, the MIDI spectra were not flux calibrated (see details in Sect. 2.3), and therefore we do not discuss spectroscopic variability.

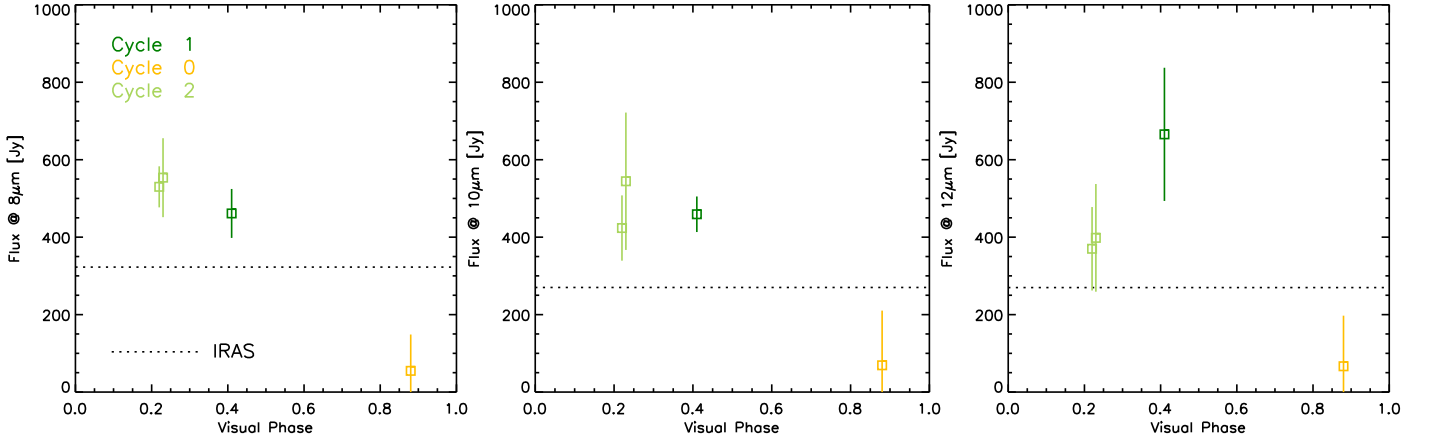


Fig. A.15. MIDI fluxes at 8, 10, and 12 μm for R Lep. The dotted line represents the IRAS flux.

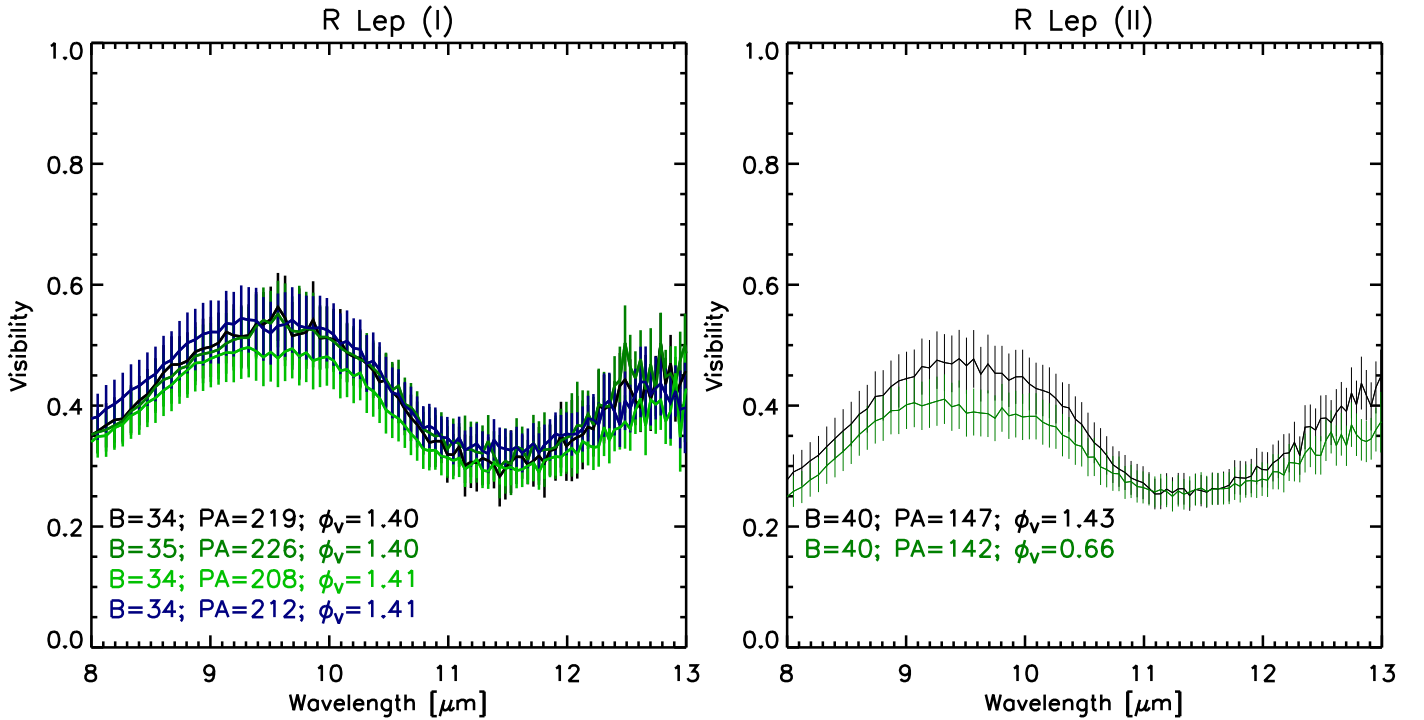


Fig. A.16. Interferometric variability for R Lep.

Appendix A.11.1: Morphology

The model fitting best both the archive and LP data is a UD with size between 12 and 9 mas. The star is larger in the 8 – 9 μm region where C_2H_2 and HCN opacities contribute, following the same wavelength dependency plotted in Fig. 3 (right panel) of Klotz et al. (2013). We confirm that no asymmetric structures are observed, and that the object can be described by a single component. This result is in line with the finding of Klotz et al. (2013), however asymmetric structures are detected much further than 10 R_\star by several authors (see Hron et al. 2015, and references therein). The object is classified in class N (naked) by Sloan et al. (1998). This class includes stars that do not exhibit dust excess in the ISO spectrum. We confirm that the visibilities do not show signs of dust (Fig. A.20).

Appendix A.12: S Sct

S Sct is a carbon-rich semi-regular pulsator with a variability amplitude of 1.5 mag in the V band and an uncertain distance (between 367 pc and 580 pc according to van Leeuwen 2007; Bergeat & Chevallier 2005, respectively). The temperature of the star is 2755 K according to Bergeat & Chevallier (2005) and 2895 K following Lambert et al. (1986). The mass-loss rate reported in literature is of the order of $10^{-6} M_\odot \text{ yr}^{-1}$ (see Table 1). The star is one of the targets surrounded by a detached shell (Olofsson et al. 1992) that formed $\sim 10^4$ yrs ago because of a superwind episode with a mass-loss rate of $\sim 10^4 M_\odot \text{ yr}^{-1}$. This shell is also observed in the Herschel/PACS images and was recently modelled by Mečina et al. (2014). The inner spatial scales probed by VLTI/PIONIER (H-band 4-beam combiner interferometer; Le Bouquin et al. 2009) can be well fitted by a UD of

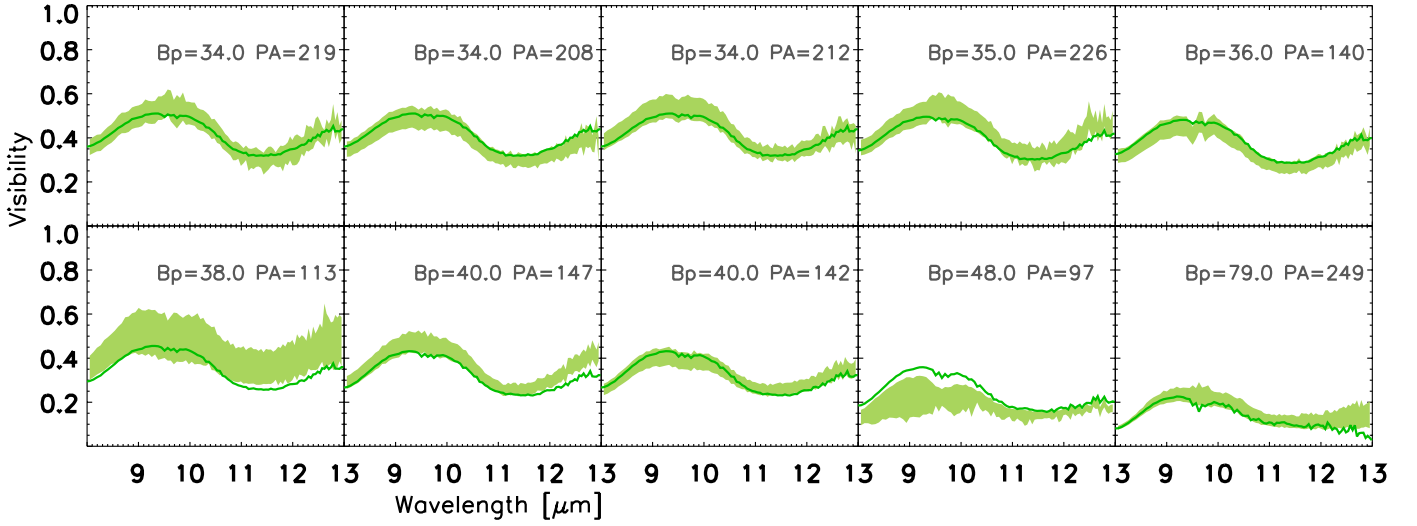


Fig. A.17. Best-fitting UD+Gaussian profile (solid line) for the MIDI visibilities of R Lep.

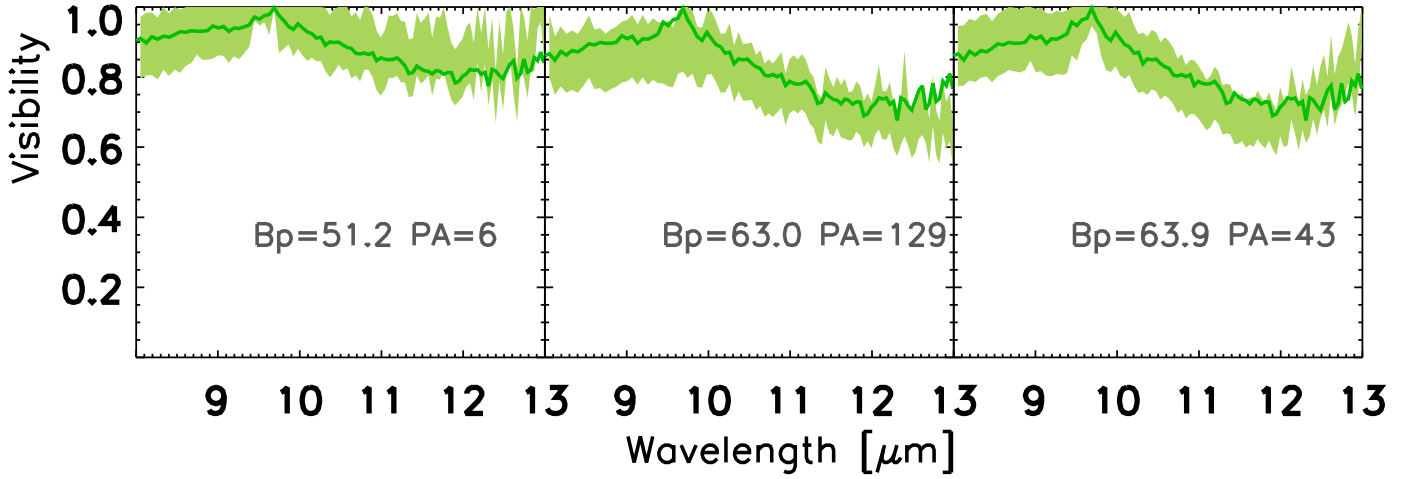


Fig. A.19. Best-fitting Gaussian profile (solid line) for the MIDI visibilities of Y Pav.

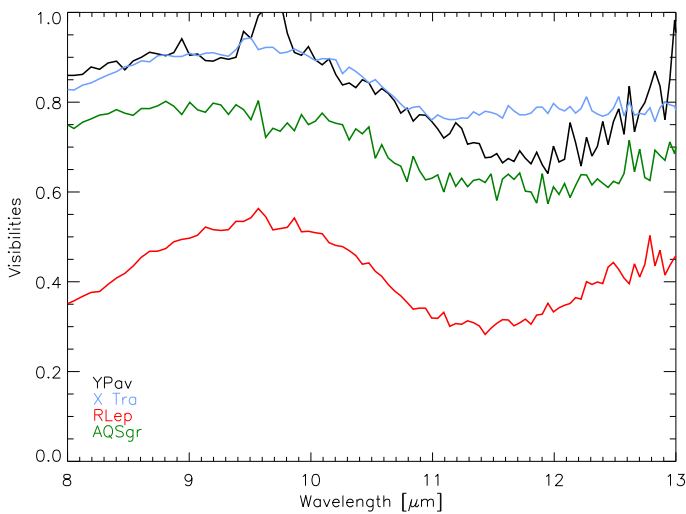


Fig. A.18. Comparison between the shape of the visibility of all the stars showing SiC.

diameter 6.22 ± 0.3 mas ($\chi^2 = 1.4$). PIONIER did not detect any asymmetric structure (Le Bouquin, private communication).

MIDI observed this object seven times between the 2011 May 28 and 30. For the modelling and data interpretation, we use only two data sets, keeping in mind that the data set of May 30 is very good, while the data of May 28 are very noisy after $11.5 \mu\text{m}$. The other five observations were affected by poor weather conditions.

Appendix A.12.1: Variability

The MIDI spectrum agrees with the flux level of the ISO observations. However, ISO shows a small bump around $11.3 \mu\text{m}$ attributable to SiC, while nothing similar is seen by MIDI. Although we cannot exclude that the shape of the MIDI spectrum is still affected by calibration problems, it is an interesting coincidence that neither is SiC observed in the visibilities (see following Section), nor that the shape of the MIDI spectrum resembles that from IRAS (Fig. A.21). Like TX Psc, S Sct is also classified as N (naked) in the Sloan et al. (1998) classification based on IRAS spectra. This could mean that the amount of SiC was too small at the time of the IRAS observations, and that it increased

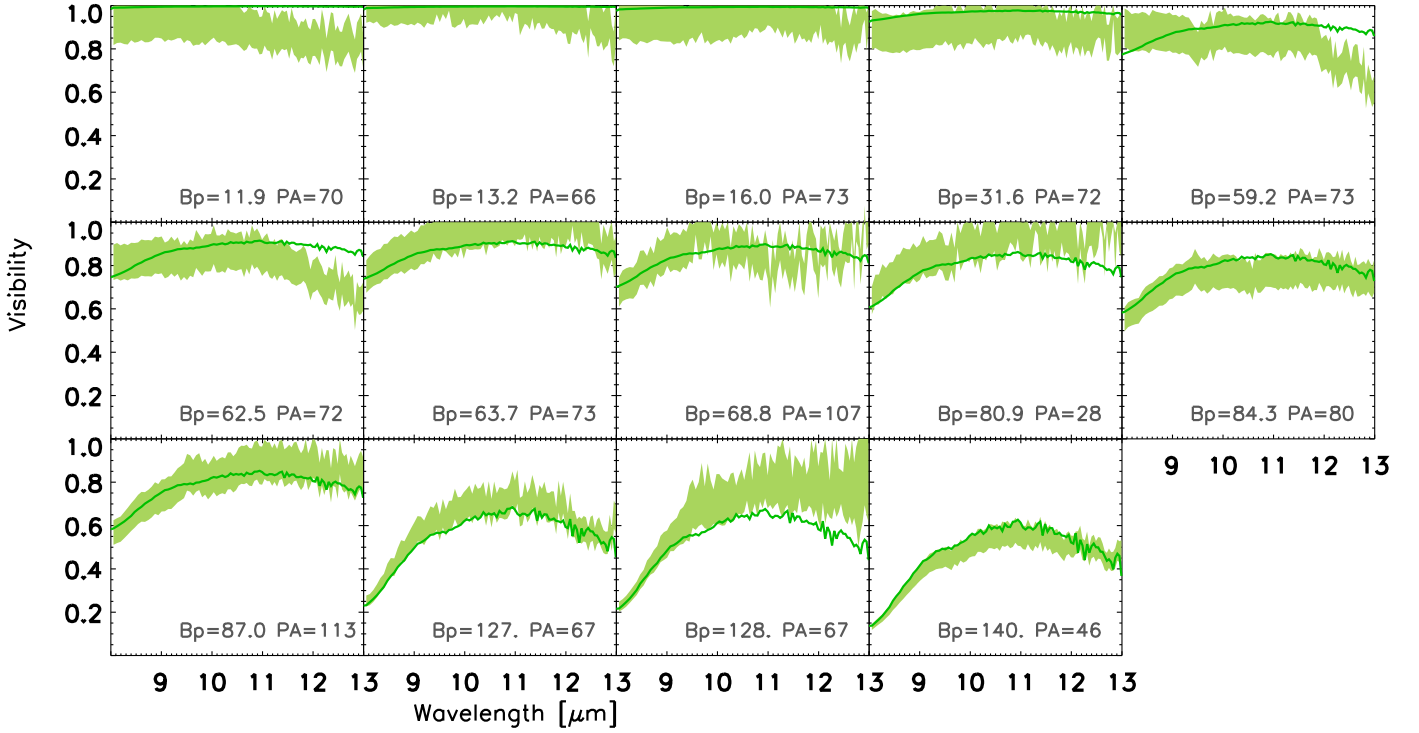


Fig. A.20. Best-fitting GEM-FIND model (solid line) for the MIDI visibilities of TX Psc.

afterwards. But given the shape of the MIDI spectrum, one presumes that the feature recently disappeared again (Fig. A.21). A more likely possibility would be a photospheric variation, i.e. no change in the SiC, but rather in the molecular opacity at wavelengths $> 10 \mu\text{m}$.

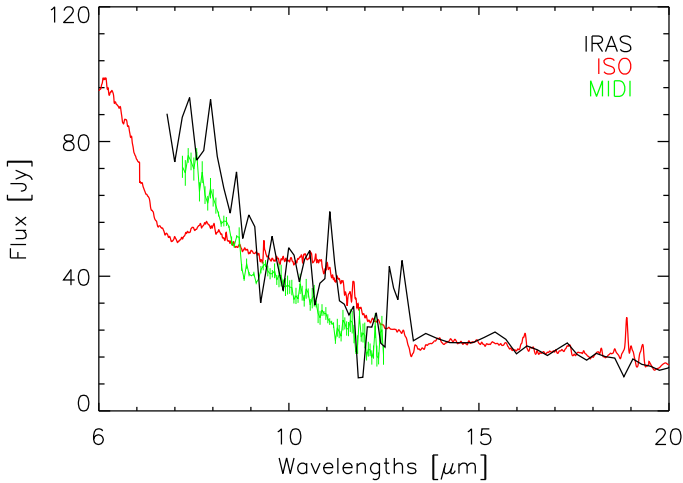


Fig. A.21. Comparison of MIDI spectrum of S Sct with those from IRAS and ISO. While the flux levels are very similar, the MIDI and IRAS spectra do not show any signature of SiC, despite being clearly visible in the ISO spectrum.

Appendix A.12.2: Morphology

The two visibility points shown in Fig. A.22 are easily fitted with circular models and the fit shows a slight preference for the Gaussian shape. Nevertheless, the robustness of that conclu-

sion should not be overestimated because of the high visibilities and small amount of data available. As in the case of U Ant, we stress that the visibility of S Sct does not show any signature of SiC. By comparing the *N*-band UD diameter with the *H*-band UD diameter measured by PIONIER, we conclude that molecular and dust (amorphous carbon) material enshrouds the object in the *N* band. No SiC is detected either in the correlated or uncorrelated flux.

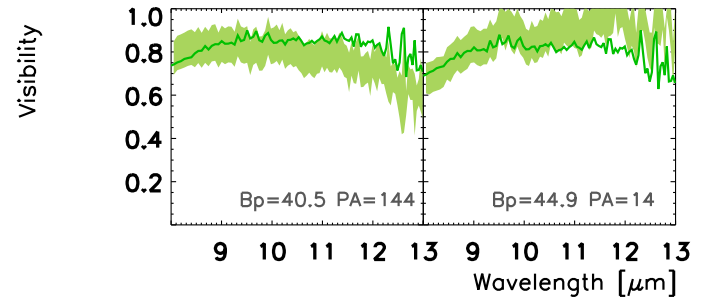


Fig. A.22. Best-fitting GEM-FIND model for the MIDI visibilities of S Sct.

Appendix A.13: AQ Sgr

AQ Sgr is a carbon-enriched semi-regular variable. The period of variability is 190 d and the distance is 330 pc (van Leeuwen 2007). The mass-loss estimates vary between $7.7 \times 10^{-7} M_{\odot} \text{ yr}^{-1}$ (Bergetat & Chevallier 2005), and $10^{-7} M_{\odot} \text{ yr}^{-1}$ (Ramstedt et al. 2014). The star is classified as fermata by Cox et al. (2012). Richichi et al. (2005) report a K-band diameter of 6.13 mas. The star was already observed with MIDI in 2008, but those data are very noisy and they were discarded during data reduction. Only

two points from the LP were used for the analysis. The archive data are corrupted by weather.

Appendix A.13.1: Variability

The MIDI spectrum of AQ Sgr is compared with the spectrum from IRAS in Fig. 6, and they fit within the uncertainties of IRAS. The shape of the spectra is rather similar, and we observe a bump around $11.3 \mu\text{m}$ due to SiC. The star was classified as SiC+ by Sloan et al. (1998) and Gupta et al. (2004). No interferometric variability can be determined from the available data set.

Appendix A.13.2: Morphology

The visibility curve presented in Fig. A.23 matches the shape of the spectrum, showing the SiC signature. The observations are well fitted by a UD profile with a diameter between 17 and 33 mas (depending on wavelength). The level of visibility at $11.3 \mu\text{m}$ is comparable to that at $12 \mu\text{m}$, where the UD diameter measures 32 mas. By comparing the latter value with the K -band diameter, we can conclude that SiC is being detected at $5 R_\star$.

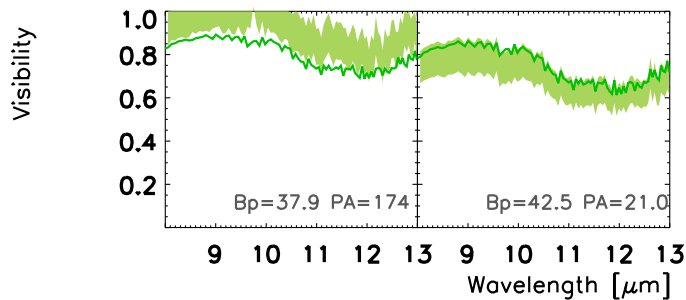


Fig. A.23. Best-fitting GEM-FIND model (solid line) for the MIDI visibilities of AQ Sgr.

Appendix A.14: X TrA

X TrA is a carbon-rich irregular variable. A detailed near-infrared spectroscopic study with line identification was presented for this object by Lebzelter et al. (2012). The star is a single object, as no indication of binarity was reported so far. Izumiura et al. (1995) detected a detached shell at a distance of $1.3'$. In Cox et al. (2012) the star is classified among the rings, but the ring detected by Herschel is faint with only a bright arc to the east. These authors conclude that more observations are needed. X TrA was observed for the first time with MIDI within the frame of our LP. Four points out of seven are used for the geometric modelling. The other points were affected by weather conditions.

Appendix A.14.1: Variability

Because of the irregular nature of the light curve, time variability cannot be studied in detail for this star. However a comparison between the MIDI and IRAS spectra (Fig. 6) shows that the flux level is unchanged and SiC is observed. The object is classified as SiC+ in the Sloan et al. (1998) classification. The presence of SiC is already detected in the IRAS spectrum shown in Fig. 6 and in the MIDI spectra as well.

Appendix A.14.2: Morphology

The X TrA MIDI data can be reproduced with a UD of size 22 - 39 mas. The χ^2_{red} of the Gaussian (Table 3) is similar for the already mentioned reason: the data sample the upper part of the visibility curve, where both Gaussian and UD profiles are very similar. The visibility curve versus wavelength shown in Fig. A.24 exhibits the shape typical of stars with SiC. The level of visibility at $11.3 \mu\text{m}$ is comparable to the level of visibility at $12 \mu\text{m}$, as do the diameters. Therefore we can conclude that for X TrA, SiC is detected at $\sim 4 R_\star$.

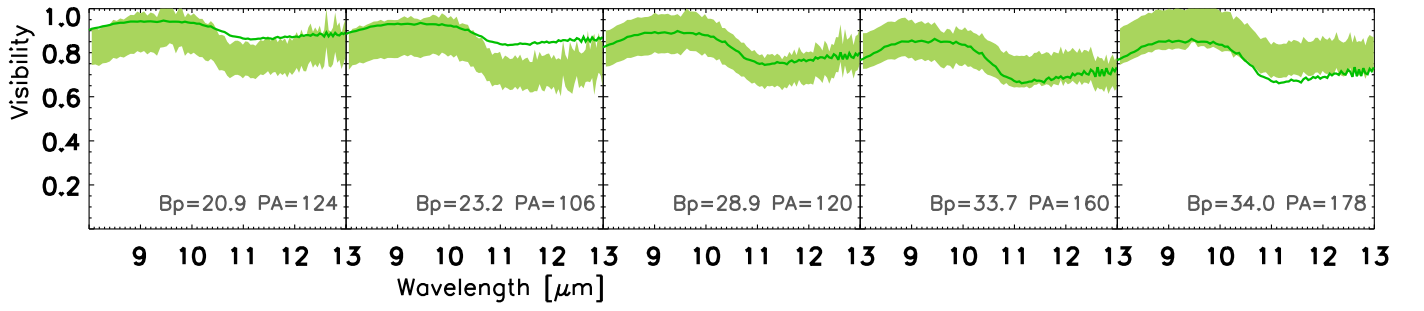


Fig. A.24. Best-fitting GEM-FIND model (solid line) for the MIDI visibilities of X Tra.

Appendix B: Journal of observations

This section presents the journal of observations for the LP dataset and the archive data used in this work. Where calibrated fluxes are available, points are marked with ‘F’. Calibrators used to calibrate the visibilities are given below the science observation. If no calibrator is listed, the science point was not used in the astrophysical interpretation.

Table B.1. Journal of the MIDI Auxiliary Telescopes observations of θ Aps.

Target	UT date & time	ϕ_V	Config.	B_p [m]	PA [°]	Seeing ["]	Airmass	Mode
LP data								
θ Aps	2011-06-11 00:28	9.27	A1-B2	10.4	92	1.01	1.651	SCIPHOT/PRISM
HD167618	2011-06-11 06:24	0.69	1.036	SCIPHOT/PRISM
HD167618	2011-06-11 08:20	0.63	1.101	SCIPHOT/PRISM
θ Aps	2011-06-11 01:21	9.27	A1-C1	15.5	76	1.66	1.630	SCIPHOT/PRISM
HD167618	2011-06-11 07:23	0.67	1.231	SCIPHOT/PRISM
HD206778	2011-06-11 07:54	0.64	1.286	SCIPHOT/PRISM
HD167618	2011-06-11 09:14	0.46	1.453	SCIPHOT/PRISM
θ Aps	2011-06-12 05:34	9.28	D0-C1	12.2	92	1.01	1.981	SCIPHOT/PRISM
HD150798	2011-06-12 05:18	1.01	1.428	SCIPHOT/PRISM
HD152786	2011-06-12 05:48	1.02	1.225	SCIPHOT/PRISM
θ Aps	2011-06-22 01:37	9.36	D0-C1	15.4	49	1.87	1.643	SCIPHOT/PRISM
HD150798	2011-06-22 01:19	1.46	1.510	SCIPHOT/PRISM
θ Aps ^F	2012-01-25 08:43	11.18	C1-A1	15.8	52	1.23	1.693	SCIPHOT/PRISM
HD81797	2012-01-25 05:57	0.71	1.040	SCIPHOT/PRISM
HD81797	2012-01-25 06:38	0.69	1.057	SCIPHOT/PRISM
HD81797	2012-01-25 07:01	0.67	1.083	SCIPHOT/PRISM
HD81797	2012-01-25 07:33	1.14	1.138	SCIPHOT/PRISM
HD150798	2012-01-25 08:11	0.91	2.138	SCIPHOT/PRISM
HD152786	2012-01-25 09:03	1.80	1.795	SCIPHOT/PRISM
θ Aps ^F	2012-01-26 08:41	11.19	D0-C1	16.7	17	1.87	1.691	SCIPHOT/PRISM
HD150798	2012-01-26 08:21	1.56	2.055	SCIPHOT/PRISM
θ Aps	2012-01-28 08:56	11.21	B2-A1	10.2	86	0.73	1.668	SCIPHOT/PRISM

Table B.2. Journal of the MIDI Auxiliary Telescopes observations of R Crt.

Target	UT date & time	ϕ_V	Config.	B_p [m]	PA [°]	Seeing ["]	Airmass	Mode
LP data								
R Crt ^F	2012-01-24 04:57	6.66	C1-A1	13.1	52	1.60	1.242	SCIPHOT/PRISM
HD81797	2012-01-24 05:16	1.08	1.057	SCIPHOT/PRISM
HD123139	2012-01-24 07:53	1.16	1.252	SCIPHOT/PRISM
HD112142	2012-01-24 08:25	0.81	1.069	SCIPHOT/PRISM
HD123139	2012-01-24 08:59	1.05	1.097	SCIPHOT/PRISM
R Crt ^F	2012-01-25 06:18	6.66	C1-A1	15.3	64	0.73	1.047	SCIPHOT/PRISM
HD81797	2012-01-25 05:57	0.71	1.040	SCIPHOT/PRISM
HD81797	2012-01-25 06:38	0.69	1.057	SCIPHOT/PRISM
HD81797	2012-01-25 07:01	0.67	1.083	SCIPHOT/PRISM
HD81797	2012-01-25 07:33	1.14	1.138	SCIPHOT/PRISM
HD150798	2012-01-25 08:11	0.91	2.138	SCIPHOT/PRISM
HD152786	2012-01-25 09:03	1.80	1.795	SCIPHOT/PRISM
R Crt ^F	2012-02-01 05:05	6.71	B2-A1	10.4	108	1.06	1.126	SCIPHOT/PRISM
HD81797	2012-02-01 04:44	0.96	1.057	SCIPHOT/PRISM
HD81797	2012-02-01 07:43	1.24	1.238	SCIPHOT/PRISM
HD81797	2012-02-01 08:15	1.25	1.366	SCIPHOT/PRISM
R Crt	2012-02-01 06:43	6.71	C1-B2	11.2	24	1.28	1.009	SCIPHOT/PRISM
R Crt	2012-02-01 08:00	6.71	B2-A1	10.9	122	1.38	1.037	SCIPHOT/PRISM
R Crt ^F	2012-02-12 05:47	6.78	C1-A1	15.8	68	0.86	1.014	SCIPHOT/PRISM
HD81797	2012-02-12 04:36	0.88	1.041	SCIPHOT/PRISM
HD81797	2012-02-12 05:11	1.13	1.047	SCIPHOT/PRISM
HD81797	2012-02-12 05:27	0.99	1.058	SCIPHOT/PRISM
HD81797	2012-02-12 06:05	0.80	1.104	SCIPHOT/PRISM
R Crt ^F	2012-05-01 00:26	7.27	C1-B2	11.2	22	1.59	1.017	SCIPHOT/PRISM
HD81797	2012-05-01 00:04	1.05	1.048	SCIPHOT/PRISM
HD81797	2012-05-01 00:46	1.29	1.091	SCIPHOT/PRISM
Archive								
R Crt ^F	2009-03-17 04:30	0.14	H0-D0	63.9	73	0.78	1.010	SCIPHOT/GRISM
HD81797	2009-03-17 04:05	1.07	1.130	SCIPHOT/GRISM
R Crt ^F	2009-03-18 03:17	0.14	H0-D0	62.5	67	1.09	1.020	SCIPHOT/GRISM
HD81797	2009-03-18 03:31	0.85	1.080	SCIPHOT/GRISM
HD120323	2009-03-18 05:23	1.46	1.070	SCIPHOT/GRISM
R Crt	2011-02-08 05:54	4.47	D0-A0	125.9	68	0.85	1.020	SCIPHOT/GRISM
R Crt	2011-02-08 06:06	4.47	K0-A0	126.8	69	0.78	1.010	SCIPHOT/GRISM
R Crt ^F	2011-03-08 02:28	4.64	H0-G0	27.4	56	1.33	1.190	SCIPHOT/GRISM
HD81797	2011-03-08 01:56	1.23	1.090	SCIPHOT/GRISM
HD81797	2011-03-08 02:44	1.14	1.040	SCIPHOT/GRISM

Table B.3. Journal of the MIDI Auxiliary Telescopes observations of R Leo.

Target	UT date & time	ϕ_V	Config.	B_p [m]	PA [°]	Seeing ["]	Airmass	Mode
LP data								
R Leo	2012-01-24 06:18	7.78	C1-A1	15.7	75	0.77	1.235	SCIPHOT/PRISM
R Leo ^F	2012-01-25 07:18	7.78	C1-A1	16.0	72	0.75	1.289	SCIPHOT/PRISM
HD81797	2012-01-25 05:57	0.71	1.040	SCIPHOT/PRISM
HD81797	2012-01-25 06:38	0.69	1.057	SCIPHOT/PRISM
HD81797	2012-01-25 07:01	0.67	1.083	SCIPHOT/PRISM
HD81797	2012-01-25 07:33	1.14	1.138	SCIPHOT/PRISM
HD150798	2012-01-25 08:11	0.91	2.138	SCIPHOT/PRISM
HD152786	2012-01-25 09:03	1.80	1.795	SCIPHOT/PRISM
R Leo	2012-01-28 03:32	7.79	B2-A1	10.7	120	0.91	1.605	SCIPHOT/PRISM
R Leo	2012-01-28 04:39	7.79	C1-B2	8.5	21	0.89	1.333	SCIPHOT/PRISM
R Leo ^F	2012-01-28 05:55	7.79	B2-A1	11.0	112	1.08	1.236	SCIPHOT/PRISM
HD81797	2012-01-28 03:11	0.79	1.297	SCIPHOT/PRISM
HD81797	2012-01-28 03:51	0.99	1.169	SCIPHOT/PRISM
HD81797	2012-01-28 05:35	1.32	1.041	SCIPHOT/PRISM
HD152786	2012-01-28 09:26	0.90	1.605	SCIPHOT/PRISM
R Leo ^F	2012-01-28 07:27	7.79	C1-B2	10.6	36	1.08	1.341	SCIPHOT/PRISM
HD81797	2012-01-28 04:20	1.10	1.107	SCIPHOT/PRISM
HD81797	2012-01-28 04:59	1.12	1.059	SCIPHOT/PRISM
HD81797	2012-01-28 07:10	0.94	1.115	SCIPHOT/PRISM
HD81797	2012-01-28 07:48	0.89	1.203	SCIPHOT/PRISM
R Leo ^F	2012-02-12 04:55	7.83	C1-A1	15.6	75	0.86	1.237	SCIPHOT/PRISM
HD81797	2012-02-12 04:36	0.88	1.041	SCIPHOT/PRISM
HD81797	2012-02-12 05:11	1.13	1.047	SCIPHOT/PRISM
HD81797	2012-02-12 05:27	0.99	1.058	SCIPHOT/PRISM
HD81797	2012-02-12 06:05	0.80	1.104	SCIPHOT/PRISM
R Leo	2012-02-12 07:34	7.83	C1-A1	14.7	65	0.97	1.601	SCIPHOT/PRISM
Archive								
R Leo	2006-01-02 07:18	0.63	G0-H0	30.6	75	0.94	1.244	HIGHSENS/PRISM
R Leo ^F	2006-02-25 03:16	0.81	D0-G0	29.2	76	0.70	1.271	HIGHSENS/PRISM
HD48915	2006-02-25 02:48	0.90	1.106	HIGHSENS/PRISM
R Leo ^F	2006-02-25 04:38	0.81	D0-G0	31.9	73	0.57	1.248	HIGHSENS/PRISM
HD48915	2006-02-25 02:48	0.90	1.106	HIGHSENS/PRISM
R Leo ^F	2006-03-03 05:29	0.83	A0-G0	62.2	69	1.06	1.395	HIGHSENS/PRISM
HD25025	2006-03-03 01:23	0.68	1.554	HIGHSENS/PRISM
HD25025	2006-03-03 02:10	1.99	2.034	HIGHSENS/PRISM
HD61421	2006-03-03 04:14	0.86	1.507	HIGHSENS/PRISM
HD123139	2006-03-03 07:22	0.76	1.035	HIGHSENS/PRISM
R Leo	2006-03-04 05:55	0.83	A0-G0	60.2	67	0.54	1.514	HIGHSENS/PRISM
HD61421	2006-03-04 01:10	0.65	1.159	HIGHSENS/PRISM
HD123139	2006-03-04 06:57	0.57	1.050	HIGHSENS/PRISM
R Leo	2006-04-20 02:17	0.98	D0-G0	31.3	69	0.69	1.38	SCIPHOT/PRISM
R Leo	2006-04-22 00:05	0.99	D0-G0	30.6	75	1.35	1.242	SCIPHOT/PRISM
R Leo ^F	2006-04-23 03:14	1.0	E0-G0	14.1	63	0.86	1.667	SCIPHOT/PRISM
α Hya	2006-04-23 03:38	1.649	SCIPHOT/PRISM
R Leo ^F	2006-04-24 23:17	1.0	E0-G0	14.4	76	0.87	1.283	SCIPHOT/PRISM
α Hya	2006-04-24 23:40	0.98	1.043	SCIPHOT/PRISM
α Hya	2006-04-24 00:39	0.73	1.055	SCIPHOT/PRISM
2Cen	2006-04-24 01:49	0.60	1.207	SCIPHOT/PRISM
2Cen	2006-04-24 02:35	0.77	1.103	SCIPHOT/PRISM
epsPeg	2006-04-24 09:26	1.18	1.682	SCIPHOT/PRISM
R Leo	2006-05-25 23:59	1.1	A0-G0	62.5	69	0.74	1.384	SCIPHOT/PRISM
R Leo	2006-11-11 08:27	1.64	H0-D0	41.7	77	0.77	1.681	SCIPHOT/PRISM
α Hya	2006-11-11 08:53	1.02	1.172	SCIPHOT/PRISM
R Leo ^F	2006-11-12 08:25	1.65	H0-D0	42	77	0.71	1.651	SCIPHOT/PRISM
α Hya	2006-11-12 09:03	0.70	1.138	SCIPHOT/PRISM
R Leo ^F	2006-12-15 07:27	1.75	E0-G0	13.6	77	0.78	1.338	SCIPHOT/PRISM
α Hya	2006-12-15 07:46	0.64	1.061	SCIPHOT/PRISM

Table B.4. Journal of R Leo continued.

Target	UT date & time	ϕ	Config.	B_p [m]	PA [°]	Seeing ["]	Airmass	Mode
R Leo ^F	2006-12-19 06:01	1.77	K0-G0	42.5	77	0.39	1.63	SCIPHOT/PRISM
α Hya	2006-12-19 05:49	0.50	1.28	SCIPHOT/PRISM
α Hya	2006-12-19 07:09	0.65	1.08	SCIPHOT/PRISM
α Hya	2006-12-19 07:46	0.68	1.049	SCIPHOT/PRISM
R Leo ^F	2006-12-21 07:07	1.78	H0-G0	27.5	77	0.91	1.33	SCIPHOT/PRISM
α Hya	2006-12-21 07:26	1.20	1.057	SCIPHOT/PRISM
R Leo ^F	2007-01-13 08:18	1.85	E0-G0	15.9	71	1.03	1.323	SCIPHOT/PRISM
α Tau	2007-01-13 01:38	1.80	1.223	SCIPHOT/PRISM
α Tau	2007-01-13 04:05	0.86	1.670	SCIPHOT/PRISM
2Cen	2007-01-13 07:32	1.19	1.436	SCIPHOT/PRISM
α Hya	2007-01-13 08:04	1.00	1.113	SCIPHOT/PRISM
2Cen	2007-01-13 08:36	1.35	1.889	SCIPHOT/PRISM
R Leo ^F	2007-01-18 04:07	1.86	H0-G0	21.6	77	-1.0	1.612	SCIPHOT/PRISM
α Hya	2007-01-18 03:54	0.95	1.271	SCIPHOT/PRISM
2Cen	2007-01-18 07:09	1.25	1.450	SCIPHOT/PRISM
α Hya	2007-01-18 07:41	0.97	1.462	SCIPHOT/PRISM
2Cen	2007-01-18 08:15	1.53	1.191	SCIPHOT/PRISM
α Hya	2007-01-18 08:50	1.62	1.296	SCIPHOT/PRISM
R Leo ^F	2007-01-21 07:29	1.87	H0-D0	63.9	72	0.70	1.296	SCIPHOT/PRISM
α Hya	2007-01-21 07:03	0.55	1.071	SCIPHOT/PRISM
2Cen	2007-01-21 07:54	0.62	1.491	SCIPHOT/PRISM
α Hya	2007-01-21 08:28	0.64	1.252	SCIPHOT/PRISM

Table B.5. Journal of the MIDI Auxiliary Telescopes observations of T Mic.

Target	UT date & time	ϕ_V	Config.	B_p [m]	PA [°]	Seeing ["]	Airmass	Mode
LP data								
T Mic	2011-06-06 07:02	0.36	B2-C1	11.3	18	1.33	1.040	SCIPHOT/PRISM
T Mic	2011-06-06 07:57	0.36	B2-C1	11.3	18	1.33	1.004	SCIPHOT/PRISM
HD167618	2011-06-06 07:39	1.60	1.096	SCIPHOT/PRISM
T Mic	2011-06-11 06:44	0.37	B2-A1	10.9	109	0.64	1.039	SCIPHOT/PRISM
T Mic	2011-06-11 07:40	0.37	C1-A1	16.0	70	0.73	1.003	SCIPHOT/PRISM
HD167618	2011-06-11 07:23	0.63	1.101	SCIPHOT/PRISM
HD167618	2011-06-11 09:14	0.46	1.453	SCIPHOT/PRISM
T Mic	2011-06-11 08:35	0.37	B2-A1	11.2	121	0.53	1.01	SCIPHOT/PRISM
HD167618	2011-06-11 08:20	0.67	1.231	SCIPHOT/PRISM
HD167618	2011-06-11 06:24	0.69	1.036	SCIPHOT/PRISM
T Mic	2011-06-11 09:29	0.37	C1-A1	14.8	82	0.55	1.079	SCIPHOT/PRISM
HD167618	2011-06-11 07:23	0.63	1.101	SCIPHOT/PRISM
HD167618	2011-06-11 09:14	0.46	1.453	SCIPHOT/PRISM
Archive								
T Mic	2004-07-08 10:09	0.08	U3-U2	33.5	55	0.77	1.735	HIGHSENS/PRISM
HD165135	2004-07-08 03:52	0.68	1.006	HIGHSENS/PRISM
HD165135	2004-07-08 04:43	0.71	1.036	HIGHSENS/PRISM
HD165135	2004-07-08 05:56	0.77	1.162	HIGHSENS/PRISM
HD165135	2004-07-08 07:12	0.56	1.458	HIGHSENS/PRISM
HD165135	2004-07-08 08:51	0.65	2.637	HIGHSENS/PRISM
T Mic ^F	2004-07-30 07:09	0.14	U3-U2	41.5	52	1.31	1.212	SCIPHOT/PRISM
HD129456	2004-07-30 01:20	0.52	1.196	SCIPHOT/PRISM
HD169916	2004-07-30 02:14	0.74	1.005	SCIPHOT/PRISM
HD169916	2004-07-30 04:57	1.08	1.175	SCIPHOT/PRISM
HD177716	2004-07-30 06:16	1.04	1.390	SCIPHOT/PRISM
T Mic ^F	2004-07-31 05:10	0.14	U3-U2	46.2	44	1.08	1.014	HIGHSENS/PRISM
HD169916	2004-07-31 01:32	0.59	1.029	HIGHSENS/PRISM
HD169916	2004-07-31 02:50	0.67	1.003	HIGHSENS/PRISM
HD165135	2004-07-31 03:31	0.65	1.057	HIGHSENS/PRISM
HD169916	2004-07-31 04:47	0.71	1.161	HIGHSENS/PRISM
T Mic	2010-10-09 00:51	0.34	D0-H0	62.8	76	0.90	1.021	SCIPHOT/GRISM

Table B.6. Journal of the MIDI Auxiliary Telescopes observations of RT Vir.

Target	UT date & time	ϕ_V	Config.	B_p [m]	PA [°]	Seeing ["]	Airmass	Mode
LP data								
RT Vir ^F	2012-01-24 07:33	0.76	C1-A1	12.6	72	0.86	1.338	SCIPHOT/PRISM
HD81797	2012-01-24 05:16	1.08	1.057	SCIPHOT/PRISM
HD112142	2012-01-24 07:17	0.86	1.207	SCIPHOT/PRISM
HD123139	2012-01-24 07:53	1.16	1.252	SCIPHOT/PRISM
HD112142	2012-01-24 08:25	0.81	1.069	SCIPHOT/PRISM
HD123139	2012-01-24 08:59	1.05	1.097	SCIPHOT/PRISM
RT Vir ^F	2012-01-24 08:42	0.76	C1-A1	14.9	74	0.81	1.182	SCIPHOT/PRISM
HD81797	2012-01-24 05:16	1.08	1.057	SCIPHOT/PRISM
HD112142	2012-01-24 07:17	0.86	1.207	SCIPHOT/PRISM
HD123139	2012-01-24 07:53	1.16	1.252	SCIPHOT/PRISM
HD112142	2012-01-24 08:25	0.81	1.069	SCIPHOT/PRISM
HD123139	2012-01-24 08:59	1.05	1.097	SCIPHOT/PRISM
RT Vir	2012-05-01 02:44	0.02	B2-A1	11.2	113	0.77	1.158	SCIPHOT/PRISM
RT Vir	2012-05-01 03:50	0.02	B2-A1	10.5	113	0.67	1.172	SCIPHOT/PRISM
RT Vir	2012-05-02 00:19	0.02	C1-B2	8.70	6	0.79	1.554	SCIPHOT/PRISM
RT Vir	2012-05-02 01:18	0.02	C1-B2	9.00	16	0.60	1.294	SCIPHOT/PRISM
Archive								
RT Vir*	2011-02-08 08:29	0.82	A0-G1	89.0	113	0.90	1.151	SCIPHOT/GRISM
HD120323	2011-02-08 08:06	0.90	1.053	SCIPHOT/GRISM
HD120323	2011-02-08 08:55	1.00	1.019	SCIPHOT/GRISM
RT Vir*	2011-03-06 06:10	0.89	G0-H0	30.0	74	1.20	1.169	SCIPHOT/GRISM
HD120323	2011-03-06 05:42	1.20	1.118	SCIPHOT/GRISM
HD120323	2011-03-06 06:35	1.20	1.043	SCIPHOT/GRISM
RT Vir*	2011-03-13 07:06	0.91	A0-K0	128.0	73	1.40	1.176	SCIPHOT/GRISM
HD120323	2011-03-13 06:46	1.30	1.018	SCIPHOT/GRISM
HD120323	2011-03-13 07:26	1.20	1.018	SCIPHOT/GRISM
RT Vir*	2009-03-18 05:03	0.98	D0-H0	59.0	74	1.70	1.189	SCIPHOT/GRISM
HD120323	2009-03-18 05:23	1.50	1.068	SCIPHOT/GRISM
RT Vir*	2009-03-18 06:03	0.98	D0-H0	63.0	73	1.00	1.152	SCIPHOT/GRISM
HD120323	2009-03-18 06:26	0.80	1.018	SCIPHOT/GRISM
RT Vir*	2009-06-03 01:33	0.18	G0-H0	32.0	73	1.00	1.166	SCIPHOT/GRISM
HD120323	2009-06-03 02:00	1.10	1.017	SCIPHOT/GRISM
RT Vir*	2009-07-01 00:26	0.26	A0-K0	126.0	72	2.40	1.017	SCIPHOT/GRISM
RT Vir ^F	2008-06-29 23:40	0.28	H0-G0	31.9	73	1.02	1.159	SCIPHOT/PRISM
HD133216	2008-06-29 01:59	1.10	1.016	SCIPHOT/PRISM
RT Vir	2008-06-29 01:09	0.28	H0-G0	30.6	70	0.90	1.317	SCIPHOT/PRISM
HD133216	2008-06-29 01:59	1.10	1.016	SCIPHOT/PRISM
RT Vir	2008-06-29 01:45	0.28	H0-G0	28.7	68	1.15	1.464	SCIPHOT/PRISM
HD133216	2008-06-29 01:59	1.10	1.016	SCIPHOT/PRISM
RT Vir ^F	2008-07-03 00:08	0.29	E0-G0	15.9	72	0.70	1.206	SCIPHOT/PRISM
HD120323	2008-07-03 01:49	1.01	1.141	SCIPHOT/PRISM
HD120323	2008-07-03 02:19	1.41	1.220	SCIPHOT/PRISM
RT Vir ^F	2008-07-03 00:45	0.29	E0-G0	15.4	71	0.85	1.291	SCIPHOT/PRISM
HD120323	2008-07-03 01:49	1.01	1.141	SCIPHOT/PRISM
HD120323	2008-07-03 02:19	1.41	1.220	SCIPHOT/PRISM
RT Vir ^F	2008-07-03 01:19	0.29	E0-G0	14.7	69	1.06	1.416	SCIPHOT/PRISM
HD120323	2008-07-03 01:49	1.01	1.141	SCIPHOT/PRISM
HD120323	2008-07-03 02:19	1.41	1.220	SCIPHOT/PRISM

Notes. * These observations have been published in Sacuto et al. (2013).

Table B.7. Journal of the MIDI Auxiliary Telescopes observations of π^1 Gru.

Target	UT date & time	ϕ_V	Config.	B_p [m]	PA [°]	Seeing ["]	Airmass	Mode
LP data								
π^1 Gru	2011-05-09 09:03	...	B2-C1	11.1	4	0.80	1.30	SCI-PHOT
π^1 Gru	2011-05-09 09:34	...	B2-C1	11.1	8	0.80	1.22	SCI-PHOT
π^1 Gru	2011-06-12 07:52	...	A1-B2	10.0	96	1.45	1.16	SCI-PHOT
HD206778	2011-06-12 07:36	1.08	1.32	SCI-PHOT
HD206778	2011-06-12 08:50	0.62	1.22	SCI-PHOT
π^1 Gru	2011-06-12 08:35	...	A1-B2	10.6	103	0.62	1.10	SCI-PHOT
HD206778	2011-06-12 07:36	1.08	1.32	SCI-PHOT
HD206778	2011-06-12 08:50	0.62	1.22	SCI-PHOT
π^1 Gru	2011-06-12 09:30	...	A1-C1	15.9	70	0.74	1.10	SCI-PHOT
HD206778	2011-06-12 09:14	0.62	1.22	SCI-PHOT
HD206778	2011-06-12 09:44	0.70	1.24	SCI-PHOT
π^1 Gru	2011-08-11 07:01	...	A1-C1	15.1	85	1.20	1.11	SCI-PHOT
HD206778	2011-08-11 06:41	1.20	1.33	SCI-PHOT
HD224935	2011-08-11 07:38	1.35	1.45	SCI-PHOT
Archive								
π^1 Gru*	2006-05-21 09:09	...	E0-G0	15.7	50	1.26	1.18	SCI-PHOT
HD214952	2006-05-21 09:28	1.57	1.85	SCI-PHOT
π^1 Gru*	2006-05-23 09:32	...	A0-G0	63.5	56	0.76	1.28	SCI-PHOT
HD214952	2006-05-23 10:06	0.71	1.12	SCI-PHOT
π^1 Gru*	2006-05-24 09:27	...	D0-G0	31.8	56	0.72	1.30	SCI-PHOT
HD214952	2006-05-24 09:44	0.65	1.40	SCI-PHOT
π^1 Gru*	2006-05-25 08:09	...	A0-G0	61.2	41	-1	1.29	SCI-PHOT
HD214952	2006-05-25 07:51	0.66	1.42	SCI-PHOT
π^1 Gru*	2006-05-27 09:20	...	E0-G0	15.9	57	1.51	1.23	SCI-PHOT
HD214952	2006-05-27 09:37	1.30	1.13	SCI-PHOT
π^1 Gru*	2006-06-19 10:16	...	D0-G0	30.6	83	0.62	1.10	SCI-PHOT
HD214952	2006-06-19 09:50	0.72	1.082	SCI-PHOT
π^1 Gru*	2006-08-08 08:40	...	A0-G0	52.6	102	0.88	1.28	SCI-PHOT
HD214952	2006-08-08 08:13	1.27	1.18	SCI-PHOT

Notes. * These observations have been published in Sacuto et al. (2008).

Table B.8. Journal of observations of \omicron Ori.

Target	UT date & time	ϕ_V	Config.	B_p [m]	PA [°]	Seeing ["]	Airmass	Mode
LP data								
\omicron Ori	2011-11-01 04:08	...	G1-I1	26.8	27	1.42	1.794	HIGHSENS/PRISM
\omicron Ori	2011-11-01 05:04	...	K0-I1	34.9	0	0.77	1.474	HIGHSENS/PRISM
HD18884	2011-11-01 04:50	0.83	1.143	HIGHSENS/PRISM
HD18884	2011-11-01 06:50	1.45	1.277	HIGHSENS/PRISM
\omicron Ori	2011-11-01 06:04	...	G1-I1	36.9	45	1.04	1.321	HIGHSENS/PRISM
HD18884	2011-11-01 03:55	1.12	1.198	HIGHSENS/PRISM
HD18884	2011-11-01 07:51	1.18	1.547	HIGHSENS/PRISM
HD18884	2011-11-01 08:35	0.93	1.924	HIGHSENS/PRISM
\omicron Ori	2011-11-01 07:03	...	K0-I1	37	16	1.38	1.285	HIGHSENS/PRISM
HD18884	2011-11-01 04:50	0.83	1.143	HIGHSENS/PRISM
HD18884	2011-11-01 06:50	1.45	1.277	HIGHSENS/PRISM
\omicron Ori	2011-11-01 08:04	...	G1-I1	44.7	48	0.88	1.355	HIGHSENS/PRISM
HD18884	2011-11-01 03:55	1.12	1.198	HIGHSENS/PRISM
HD18884	2011-11-01 07:51	1.18	1.547	HIGHSENS/PRISM
HD18884	2011-11-01 08:35	0.93	1.924	HIGHSENS/PRISM
\omicron Ori	2011-11-01 08:47	...	G1-I1	46	47	1.05	1.482	HIGHSENS/PRISM
HD18884	2011-11-01 03:55	1.12	1.198	HIGHSENS/PRISM
HD18884	2011-11-01 07:51	1.18	1.547	HIGHSENS/PRISM
HD18884	2011-11-01 08:35	0.93	1.924	HIGHSENS/PRISM
\omicron Ori	2011-11-04 04:40	...	H0-I1	39.6	141	0.87	1.526	HIGHSENS/PRISM
\omicron Ori	2011-11-04 07:24	...	H0-I1	31.9	146	1.80	1.309	HIGHSENS/PRISM
HD18884	2011-11-04 04:23	0.80	1.150	HIGHSENS/PRISM
HD18884	2011-11-04 07:08	1.62	1.382	HIGHSENS/PRISM
\omicron Ori	2011-11-05 04:58	...	H0-I1	38.9	140	0.83	1.439	HIGHSENS/PRISM
HD18884	2011-11-05 04:40	1.42	1.142	HIGHSENS/PRISM
Archive data								
\omicron Ori	2005-11-12 06:51	...	U1-U4	128	65	0.56	1.314	SCIPHOT/PRISM
HD50778	2005-11-12 08:04	0.58	1.025	SCIPHOT/PRISM
HD50778	2005-11-12 09:18	0.66	1.068	SCIPHOT/PRISM
\omicron Ori	2005-12-26 05:51	...	U1-U4	125	57	1.78	1.718	SCIPHOT/PRISM
HD39425	2005-12-26 00:25	0.73	1.553	SCIPHOT/PRISM
HD50778	2005-12-26 07:13	1.23	1.159	SCIPHOT/PRISM
\omicron Ori	2005-12-30 05:10	...	U1-U4	128	59	0.80	1.570	SCIPHOT/GRISM
HD50778	2005-12-30 05:48	0.85	1.040	SCIPHOT/GRISM
HD50778	2005-12-30 05:37	0.81	1.040	SCIPHOT/GRISM
\omicron Ori	2005-12-30 05:00	...	U1-U4	128	60	0.86	1.510	SCIPHOT/GRISM
HD50778	2005-12-30 05:48	0.85	1.040	SCIPHOT/GRISM
HD50778	2005-12-30 05:37	0.81	1.040	SCIPHOT/GRISM
\omicron Ori	2005-12-30 04:50	...	U1-U4	129	61	0.77	1.480	SCIPHOT/GRISM
HD50778	2005-12-30 05:48	0.85	1.040	SCIPHOT/GRISM
HD50778	2005-12-30 05:37	0.81	1.040	SCIPHOT/GRISM
\omicron Ori ^F	2005-12-31 02:53	0.61	U1-U4	123	66	0.70	1.280	SCIPHOT/GRISM
HD50778	2005-12-31 03:29	0.59	1.100	SCIPHOT/GRISM
\omicron Ori	2005-12-31 02:42	...	U1-U4	121	67	0.64	1.290	SCIPHOT/GRISM
HD50778	2005-12-31 03:29	0.59	1.100	SCIPHOT/GRISM

Table B.9. Journal of the MIDI Auxiliary Telescopes observations of U Ant.

Target	UT date & time	ϕ_V	Config.	B_p [m]	PA [°]	Seeing ["]	Airmass	Mode
LP data								
U Ant	2012-01-25 04:03	...	D0-A1	35.7	28	1.26	1.3	HIGHSENS/PRISM
U Ant	2012-01-25 05:10	...	D0-A1	35.7	28.8	1.08	1.12	HIGHSENS/PRISM
HD29139	2012-01-25 02:12	1.11	1.40	HIGHSENS/PRISM
U Ant	2012-01-29 04:46	...	B2-D0	33.8	11	1.00	1.144	HIGHSENS/PRISM
U Ant	2011-11-04 08:38	...	H0-I1	30.2	129	1.54	1.54	HIGHSENS/PRISM
U Ant	2011-11-06 05:10	...	H0-I1	28.6	128	1.39	1.6	HIGHSENS/PRISM
Archive data								
U Ant*	2008-01-10 08:25	...	G0-H0	31.5	75.5	1.07	1.04	HIGHSENS/PRISM
HD48915	2008-01-10 06:50	1.46	1.04	HIGHSENS/PRISM
HD120323	2008-01-10 09:00	0.92	1.16	HIGHSENS/PRISM
U Ant*	2008-01-11 05:47	...	G0-H0	31.5	49	0.74	1.16	HIGHSENS/PRISM
U Ant*	2008-01-11 07:22	...	G0-H0	32.0	66	1.24	1.04	HIGHSENS/PRISM
U Ant*	2008-01-11 09:17	...	E0-H0	15.2	84	0.66	1.08	HIGHSENS/PRISM
U Ant*	2008-02-20 04:22	...	A0-H0	95.6	62.6	0.66	1.06	HIGHSENS/PRISM
HD48915	2008-02-20 05:14	0.58	1.24	HIGHSENS/PRISM
U Ant*	2008-03-14 01:42	...	E0-G0	15.3	50	0.67	1.15	HIGHSENS/PRISM
U Ant*	2008-03-14 02:24	...	E0-H0	15.8	58	0.75	1.09	HIGHSENS/PRISM
U Ant*	2007-11-26 08:33	...	E0-G0	15.1	46	1.68	1.2	HIGHSENS/PRISM

Notes. * These observations have been published in Ladjal (2011), but we performed a new data reduction.

Table B.10. Journal of the MIDI Auxiliary Telescopes observations of R Lep.

Target	UT date & time	ϕ_V	Config.	B_p [m]	PA [°]	Seeing ["]	Airmass	Mode
LP data								
R Lep ^F	2011-10-24 06:36	1.40	D0-A1	34	219	0.82	1.042	SCIPHOT/PRISM
HD20720	2011-10-24 06:16	0.69	1.00	SCIPHOT/PRISM
HD48915	2011-10-24 06:54	0.56	1.208	SCIPHOT/PRISM
HD20720	2011-10-24 07:25	0.41	1.077	SCIPHOT/PRISM
HD48915	2011-10-24 08:02	0.62	1.059	SCIPHOT/PRISM
R Lep ^F	2011-10-24 07:44	1.40	D0-A1	35	226	0.60	1.016	SCIPHOT/PRISM
HD20720	2011-10-24 06:16	0.67	1.00	SCIPHOT/PRISM
HD48915	2011-10-24 06:54	0.62	1.208	SCIPHOT/PRISM
HD20720	2011-10-24 07:25	0.41	1.077	SCIPHOT/PRISM
HD48915	2011-10-24 08:02	0.69	1.059	SCIPHOT/PRISM
R Lep ^F	2011-10-26 07:44	1.41	D0-B2	34	208	1.03	1.019	SCIPHOT/PRISM
HD48915	2011-10-26 07:28	1.53	1.01	SCIPHOT/PRISM
HD20720	2011-10-26 08:03	1.65	1.179	SCIPHOT/PRISM
HD20720	2011-10-26 08:20	1.39	1.239	SCIPHOT/PRISM
HD48915	2011-10-26 09:04	1.01	SCIPHOT/PRISM
R Lep ^F	2011-10-26 08:40	1.41	D0-B2	34	212	1.22	1.068	SCIPHOT/PRISM
HD48915	2011-10-26 07:28	1.53	1.01	SCIPHOT/PRISM
HD20720	2011-10-26 08:03	1.65	1.179	SCIPHOT/PRISM
HD20720	2011-10-26 08:20	1.39	1.239	SCIPHOT/PRISM
HD48915	2011-10-26 09:04	1.01	SCIPHOT/PRISM
R Lep	2011-11-04 02:55	1.43	H0-I1	36	140	1.14	1.77	SCIPHOT/PRISM
HD20720	2011-11-04 02:37	1.30	1.22	SCIPHOT/PRISM
HD20720	2011-11-04 03:12	1.31	1.12	SCIPHOT/PRISM
R Lep ^F	2011-11-04 06:26	1.43	H0-I1	40	147	1.01	1.22	SCIPHOT/PRISM
HD20720	2011-11-04 06:08	0.84	1.03	SCIPHOT/PRISM
HD48915	2011-11-04 06:49	1.38	1.11	SCIPHOT/PRISM
Archive								
R Lep	2010-12-08 02:47	0.66	H0-I1	40	142	0.75	1.12	SCIPHOT/PRISM
HD20720	2010-12-08 02:29	0.77	1.00	SCIPHOT/PRISM
HD48915	2010-12-08 03:11	0.65	1.47	SCIPHOT/PRISM
R Lep	2011-03-11 00:35	0.88	H0-I1	38	113	1.16	1.17	SCIPHOT/PRISM
HD48915	2011-03-11 00:14	1.16	1.01	SCIPHOT/PRISM
HD20720	2011-03-11 00:47	1.09	1.73	SCIPHOT/PRISM
R Lep ^F	2012-10-05 07:57	2.22	A1-G1	79	249	0.5	1.034	SCIPHOT/PRISM
HD20720	2012-10-05 07:41	0.44	1.01	SCIPHOT/PRISM
HD32887	2012-10-05 08:11	0.52	1.01	SCIPHOT/PRISM
R Lep ^F	2012-10-12 04:18	2.23	A1-G1	48	97	1.21	1.79	SCIPHOT/PRISM
HD20720	2012-10-12 04:01	1.15	1.26	SCIPHOT/PRISM
HD32887	2012-10-12 04:34	0.95	1.61	SCIPHOT/PRISM

Table B.11. Journal of the MIDI Auxiliary Telescopes observations of Y Pav

Target	UT date & time	ϕ_V	Config.	B_p [m]	PA [°]	Seeing ["]	Airmass	Mode
LP data								
Y Pav ^F	2011-05-30 07:12:53	0.57	D0-H0	63.9	43	0.63	1.55	HIGH-SENS
HD 150798	2011-05-30 06:55:42	0.84	1.48	...
Y Pav	2011-05-30 09:07:32	0.57	H0-G1	51.2	6	0.78	1.42	HIGH-SENS
HD 150798	2011-05-30 08:50:24	0.75	1.77	...
HIP 82363	2011-05-30 09:22:51	0.82	1.83	...
Y Pav	2011-05-30 09:59:51	0.57	D0-G1	63	129	0.82	1.42	HIGH-SENS
HIP 82363	2011-05-30 09:42:36	0.78	2.03	...
HIP 82363	2011-05-30 10:15:22	0.87	2.12	...
Y Pav	2011-05-30 08:04:00	0.57	D0-H0	63.6	55	0.95	1.47	HIGH-SENS
Y Pav	2011-05-31 07:54:30	0.57	H0-G1	51.3	-4	0.77	1.47	HIGH-SENS
Y Pav	2011-05-31 08:50:28	0.57	D0-G1	60.1	116	0.63	1.42	HIGH-SENS
Y Pav	2011-07-02 04:26:06	0.71	H0-I1	51.0	85	0.53	1.83	HIGH-SENS

Table B.12. Journal of MIDI observations of TX Psc

Target	UT date & time	ϕ	Config.	B_p [m]	PA [°]	Seeing ["]	Airmass	Mode
LP data								
TX Psc	2011-10-30 01:42	...	K0-G1	80.9	28	1.26	1.136	HIGH-SENS
HIP 1170	2011-10-30 01:55	1.31	1.012	HIGH-SENS
TX Psc	2011-10-30 02:29	...	K0-A1	128	67	1.44	1.147	HIGH-SENS
HIP 154	2011-10-30 02:16	1.29	1.056	HIGH-SENS
HIP 1170	2011-10-30 02:41	1.30	1.008	HIGH-SENS
TX Psc	2011-10-30 03:29	...	G1-A1	68.8	107	1.17	1.239	HIGH-SENS
HIP 1170	2011-10-30 03:41	1.10	1.058	HIGH-SENS
TX Psc	2011-10-31 00:55	...	K0-G1	77.4	23	1.00	1.170	HIGH-SENS
TX Psc	2011-10-31 01:45	...	G1-A1	79.5	106	0.87	1.135	HIGH-SENS
TX Psc	2011-11-01 00:38	...	K0-G1	76.4	21	0.66	1.190	HIGH-SENS
TX Psc	2011-11-01 01:57	...	K0-A1	127	67	0.75	1.135	HIGH-SENS
HIP 154	2011-11-01 02:08	0.77	1.059	HIGH-SENS
Archive								
TX Psc	2006-08-28 02:50	...	E0-G0	9.4	81	1.41	1.718	HIGH-SENS
TX Psc *	2006-10-19 00:19	...	E0-G0	11.9	70	...	1.387	HIGH-SENS
HD48915	2006-10-19 08:26	0.57	1.325	HIGH-SENS
TX Psc *	2006-10-18 05:46	...	E0-G0	13.2	66	0.89	1.659	HIGH-SENS
HD48915	2006-10-18 06:57	0.87	1.278	HIGH-SENS
TX Psc	2005-06-29 08:55	...	E0-G0	13.7	82	0.54	1.238	HIGH-SENS
TX Psc	2010-09-07 04:13	...	E0-G0	14.4	73	0.93	1.194	HIGH-SENS
TX Psc	2006-08-28 05:48	...	E0-G0	15.6	73	1.30	1.136	HIGH-SENS
TX Psc	2009-11-15 02:18	...	E0-G0	15.7	72	1.26	1.225	HIGH-SENS
TX Psc*	2006-10-18 03:18	...	E0-G0	16.0	73	1.00	1.149	HIGH-SENS
HD48915	2006-10-18 06:57	0.87	1.278	HIGH-SENS
TX Psc	2006-09-20 02:28	...	D0-G0	25.1	71	1.21	1.327	HIGH-SENS
TX Psc	2006-09-20 03:23	...	D0-G0	29.0	73	1.90	1.189	HIGH-SENS
TX Psc	2006-10-16 02:12	...	H0-G0	30.5	73	0.67	1.150	HIGH-SENS
TX Psc	2009-11-16 02:13	...	H0-G0	31.0	72	0.95	1.219	HIGH-SENS
TX Psc*	2006-09-20 05:47	...	D0-G0	31.6	72	1.64	1.201	HIGH-SENS
HD20720	2006-09-20 09:48	0.89	1.095	HIGH-SENS
TX Psc	2009-11-16 01:20	...	H0-G0	32.0	73	1.36	1.146	HIGH-SENS
TX Psc	2006-09-21 01:48	...	K0-G0	44.0	68	1.01	1.489	HIGH-SENS
TX Psc*	2006-09-21 03:32	...	K0-G0	59.2	73	1.02	1.169	HIGH-SENS
HD48915	2006-09-21 08:36	1.51	1.309	HIGH-SENS
TX Psc	2006-09-17 04:20	...	A0-G0	62.0	73	1.36	1.140	HIGH-SENS
TX Psc*	2006-09-21 05:55	...	K0-G0	62.5	72	1.39	1.225	HIGH-SENS
HD48915	2006-09-21 08:36	1.51	1.309	HIGH-SENS
TX Psc	2008-09-27 04:45	...	G1-D0	63.6	133	1.00	1.155	HIGH-SENS
TX Psc*	2006-08-17 07:00	...	A0-G0	63.7	73	0.39	1.137	HIGH-SENS
HD224935	2006-08-17 07:23	0.43	1.060	HIGH-SENS
TX Psc*	2004-10-30 03:28	...	UT2-UT4	84.3	80	0.78	1.244	HIGH-SENS
HD49161	2004-10-30 09:19	0.72	1.196	HIGH-SENS
TX Psc*	2006-08-16 07:06	...	A0-G1	87	113	0.85	1.137	HIGH-SENS
HD18884	2006-08-16 07:57	0.81	1.353	HIGH-SENS
TX Psc	2006-08-15 06:20	...	A0-G1	90.3	113	0.88	1.145	HIGH-SENS
TX Psc	2011-09-21 05:39	...	I1-A1	104.0	84	1.03	1.186	HIGH-SENS
TX Psc	2011-10-05 04:21	...	K0-A1	129.0	67	0.57	1.158	HIGH-SENS
TX Psc*	2011-10-02 05:44	...	A1-J3	140.0	46	1.02	1.305	HIGH-SENS
HD45348	2011-10-02 06:42	0.88	1.512	HIGH-SENS

Notes. * These observations have been published in Klotz et al. (2013).

Table B.13. Journal of the MIDI Auxiliary Telescopes observations of S Sct

Target	UT date & time	ϕ_V	Config.	B_p [m]	PA [°]	Seeing ["]	Airmass	Mode
LP data								
S Sct	2011-05-02 08:18:31	0.84	H0-I1	40	146	0.37	1.05	HIGH-SENS
S Sct	2011-05-28 05:34:10	0.02	K0-I1	44	1	1.23	1.13	HIGH-SENS
S Sct	2011-05-28 06:34:05	0.02	K0-I1	44.3	8	1.24	1.05	HIGH-SENS
S Sct	2011-05-28 08:28:37	0.02	G1-I1	46.6	45	0.55	1.11	HIGH-SENS
S Sct	2011-05-28 09:18:32	0.02	G1-I1	45.9	46	0.90	1.23	HIGH-SENS
S Sct ^F	2011-05-28 07:27:11	0.02	K0-I1	44.9	14	0.96	1.05	HIGH-SENS
HIP89931	2011-05-28 06:15:23	...	K0-I1	46.5	9	1.01	1.01	HIGH-SENS
HIP89931	2011-05-28 07:08:03	...	K0-I1	46.3	14	1.41	1.01	HIGH-SENS
S Sct ^F	2011-05-30 06:06:29	0.03	H0-I1	40.5	144	1.01	1.07	HIGH-SENS
HIP89931	2011-05-30 05:44:39	...	H0-I1	40.1	144	0.94	1.02	HIGH-SENS
HIP90496	2011-05-30 06:23:06	...	H0-I1	40.7	148	0.86	1.00	HIGH-SENS

Table B.14. Journal of the MIDI Auxiliary Telescopes observations of AQ Sgr

Target	UT date & time	ϕ_V	Config.	B_p [m]	PA [°]	Seeing ["]	Airmass	Mode
LP data								
AQ Sgr ^F	2011-05-02 07:14:32	0.86	G1-I1	42.5	21	0.46	1.20	HIGH-SENS
HIP89931	2011-05-02 07:00:03	...	G1-I1	46.3	29	0.47	1.06	HIGH-SENS
HIP89931	2011-05-02 09:01:28	...	H0-I1	40.7	154	0.49	1.02	HIGH-SENS
HIP90496	2011-05-02 07:31:27	...	G1-I1	46.2	33	0.42	1.02	HIGH-SENS
HIP90496	2011-05-02 08:01:01	...	H0-I1	40.6	146	0.37	1.01	HIGH-SENS
AQ Sgr	2011-06-25 09:29:49	0.14	K0-I1	46.0	27	1.14	1.55	HIGH-SENS
AQ Sgr	2011-06-25 10:14:24	0.14	K0-I1	45.1	28	1.54	1.98	HIGH-SENS
AQ Sgr	2011-06-26 08:39:47	0.14	G1-I1	42.5	48	1.40	1.29	HIGH-SENS
AQ Sgr	2011-06-29 08:53:11	0.16	H0-I1	37.9	174	1.51	1.41	HIGH-SENS
HIP89931	2011-06-29 08:35:10	...	H0-I1	37.9	174	1.47	1.70	HIGH-SENS
AQ Sgr	2011-07-26 05:50:55	0.29	K0-I1	46.6	21	0.55	1.13	HIGH-SENS
AQ Sgr	2011-07-26 06:36:13	0.29	G1-I1	43.8	48	0.43	1.27	HIGH-SENS
AQ Sgr	2011-07-29 03:20:37	0.31	H0-I1	40.7	146	0.76	1.02	HIGH-SENS
Archive								
AQ Sgr	2008-06-29 02:18:18	0.65	H0-G1	22.5	42	1.01	1.50	SCIPHOT
AQ Sgr	2008-06-29 03:28:33	0.65	H0-G1	27.0	56	0.99	1.18	SCIPHOT
AQ Sgr	2008-06-29 07:53:17	0.65	H0-G1	28.4	78	2.08	1.18	SCIPHOT
AQ Sgr	2008-07-01 02:50:34	0.66	E0-G0	12.5	51	0.51	1.29	SCIPHOT
AQ Sgr	2008-07-01 04:01:38	0.66	E0-G0	14.6	62	0.45	1.09	SCIPHOT
AQ Sgr	2008-07-01 05:44:36	0.66	E0-G0	16.0	72	0.64	1.01	SCIPHOT
AQ Sgr	2008-07-02 05:41:29	0.67	E0-G0	16.0	71	0.84	1.01	SCIPHOT
AQ Sgr	2008-07-02 06:50:18	0.67	E0-G0	15.4	76	0.74	1.07	SCIPHOT
AQ Sgr	2008-07-02 08:46:43	0.67	E0-G0	11.7	81	0.91	1.46	SCIPHOT
AQ Sgr	2008-07-03 07:21:32	0.67	H0-G0	29.3	77	1.43	1.14	SCIPHOT
AQ Sgr	2008-07-03 07:56:31	0.67	H0-G0	27.2	79	0.86	1.24	SCIPHOT

Table B.15. Journal of the MIDI Auxiliary Telescopes observations of X TrA

Target	UT date & time	ϕ_V	Config.	B_p [m]	PA [°]	Seeing ["]	Airmass	Mode
LP data								
X TrA ^F	2011-04-23 03:47:06	...	K0-I1	34.0	178	0.82	1.52	HIGH-SENS
X TrA ^F	2011-04-23 05:11:55	33.7	160	0.67	1.43	HIGH-SENS
HD 150798	2011-04-23 03:24:38	0.85	1.81	HIGH-SENS
HD 150798	2011-04-23 04:02:21	0.71	1.68	HIGH-SENS
HD 150798	2011-04-23 04:56:30	0.74	1.54	HIGH-SENS
X TrA	2011-06-12 06:26:20	...	D0-A1	23.2	106	1.08	1.81	HIGH-SENS
HD 150798	2011-06-12 06:12:58	1.09	1.50	HIGH-SENS
HD 150798	2011-06-12 06:38:46	0.95	1.55	HIGH-SENS
X TrA ^F	2011-07-01 23:32:31	...	H0-I1	28.9	120	0.50	1.59	HIGH-SENS
HD 150798	2011-07-01 23:17:56	0.54	1.71	HIGH-SENS
HD 150798	2011-07-01 23:47:03	0.50	1.61	HIGH-SENS
X TrA	2011-07-02 07:40:35	...	H0-I1	33.2	-149	0.51	2.80	HIGH-SENS
X TrA	2011-07-29 02:33:26	...	H0-I1	34.5	173	0.96	1.65	HIGH-SENS
X TrA	2011-08-10 03:36:41	...	D0-A1	20.9	124	1.65	2.10	HIGH-SENS
HD 150798	2011-08-10 03:17:22	1.55	1.62	HIGH-SENS
HD 150798	2011-08-10 03:59:46	1.32	1.76	HIGH-SENS